Cardio-respiratory Health Monitoring Using a Wearable Radar System

by

Serene Abu-Sardanah

A thesis
presented to the University of Waterloo
in fulfillment of the
thesis requirement for the degree of
Master of Applied Science
in
Electrical and Computer Engineering

Waterloo, Ontario, Canada, 2023

©Serene Abu-Sardanah 2023

Author's Declaration

I hereby declare that I am the sole author of this thesis. This is a true copy of the thesis, including any required final revisions, as accepted by my examiners.

I understand that my thesis may be made electronically available to the public.

Abstract

Assessing cardio-pulmonary health is a crucial aspect of evaluating overall well-being. With the rise of cardiovascular and respiratory diseases worldwide, monitoring these physiological functions is vital for proper healthcare assessment. Cardiovascular and respiratory diseases pose significant global health concerns. According to the World Health Organization (WHO), cardiovascular disease (CVD) stands as the leading cause of global deaths, accounting for approximately 17.9 million deaths annually. Similarly, respiratory diseases such as chronic obstructive pulmonary disease (COPD) and asthma affect millions of people, resulting in high healthcare costs and a diminished quality of life. Monitoring cardiopulmonary health is of utmost importance, particularly in the wake of the COVID-19 pandemic. Studies reveal decreased cardiovascular and pulmonary performance post-infection, particularly among older adults and those with comorbidities.

A traditional gold standard method for cardiac or respiratory monitoring, such as an electrocardiogram (ECG) or spirometry, has limitations. These limitations include complexity, skin irritations, lack of continuous monitoring, and the requirement for patient cooperation. Contactless radar-based monitoring techniques that use continuous wave (CW) and frequency-modulated CW (FMCW) radars offer a solution. These techniques provide detailed information on cardio-respiratory mechanics and rates by capturing the minor chest vibrations caused by respiration and cardiac activity, which are imperceptible to the naked eye. This sensitivity to minute vibrations is particularly pronounced in the case of millimeter-wave (mm-Wave) radar systems. FMCW radars come with advantages such as a simple architecture, customizable resolution, distance and velocity data, and continuous signal acquisition. However, these contactless far-field operation methods encounter challenges. These challenges prevent the widespread adoption of the technology and include random body movements, multiple targets, noise distortion, a limited field of view, and difficulties in accurately extracting cardiac information when simultaneous respiration is present.

An FMCW radar operating in the near-field is proposed for use as a chest wearable, employing a mm-Wave radar module (Infineon, BGT60TR13C). This chest-wearable radar module functions at 60 GHz, enabling the uninterrupted extraction of various vital signs (VS) linked to cardio-respiratory activity. This system provides valuable information about the displacement waveforms associated with the movement of the chest during respiration and the cardiac cycle. Additionally, it accurately measures the respiratory rate (RR), heart rate (HR), and heart rate variability (HRV).

To ensure the effectiveness of the radar antenna when in close proximity to the skin, comprehensive full-wave electromagnetic simulations were conducted. These simulations

aim to evaluate the performance of the radar system and its ability to perform satisfactorily after attenuation due to the presence of the human torso on the near field. The results showed that the radar antenna demonstrates acceptable levels of resultant loading with skin in the near field, allowing for precise measurements of cardio-respiratory displacement waveforms.

Furthermore, experiments to extract cardiac and respiratory waveforms and rates are conducted with the chest-worn prototype, with feature-rich cardio-respiratory displacement waveforms being successfully extracted. Extracted cardiac waveforms are detailed, and cardiac events are successfully mapped to a time-synchronized ECG signal acquired by a health monitoring belt (Fourth Frontier, Frontier X). Similarly, the HR and HRV were extracted with accuracies exceeding 97% when compared to the Frontier X under breath-holding conditions. The effect of respiration on the quality of extracted cardiac signals is demonstrated, as it reduced accuracy of extracted cardiac biometrics to around 89%. Moreover, the low sensitivity of the extracted cardiac signals and biometrics to the position of the radar on the chest is highlighted as the radar measures mechanical vibrations that propagate anywhere on the chest. Likewise, detailed respiratory waveforms are extracted that enable accurate estimation of RR, with an accuracy of 98% achieved for the stationary RR estimation when compared to a ground truth metronome. We also demonstrate system effectiveness at differentiating between different types of breathing (laboured, shallow), and apnea with a high true positive rate by employing a statistical thresholding method. Finally, we explore the efficacy of the system as a respiratory monitoring tool during exercise and demonstrate its superior performance when compared to an off-the-shelf health monitoring device (i.e., Frontier, X) with time-synchronized RR data when compared to a ground truth metronome that regulates participants' breathing.

To conclude, recommendations are made to increase system data security, throughput, and scalability by employing a custom power over Ethernet (PoE) system. The system diagram and the firmware implementation are summarized to highlight the interactions between different system components. Additionally, a recommendation is made to investigate a dual-band system that makes use of an additional frequency, particularly the 2.4-2.5 GHz frequency band as it offers better penetration through the human body, which could offer additional functional cario-respiratory information.

Acknowledgements

I would like to express my heartfelt gratitude to my supervisors Professor Omar Ramahi and Professor George Shaker for their invaluable guidance, support, and expertise throughout my Master's journey. Their insightful feedback and encouragement played a significant role in shaping this work.

I am also immensely grateful to my family for their unwavering love, encouragement, and belief in my abilities. Their constant support and understanding provided the foundation on which I could pursue this endeavour.

I extend my deepest appreciation to my friends for their understanding, patience, and motivation. Their presence and companionship made this journey not only academically fulfilling but also memorable and enjoyable.

Lastly, I would like to acknowledge all the individuals who have contributed to my research in any way, directly or indirectly, particularly my friends and colleagues at the Wireless Sensors and Devices Lab and the Advanced Concepts Research Laboratory. Your assistance, collaboration, and encouragement have been instrumental in the completion of this thesis.

Thank you all for being a part of this significant milestone in my life.

Dedication

I dedicate this work to my loving parents, whose unwavering support and belief in me have been my constant motivation. Your guidance and encouragement have shaped me into the person I am today.

To my brothers, Faisal and Rayan, thank you for always being there, offering both laughter and a listening ear. Your love and camaraderie have brought joy to my journey.

This accomplishment is as much yours as it is mine, and I am forever grateful for your presence in my life.

Table of Contents

Author's Declaration ii

Abstract iii

Acknowledgements v

Dedication vi

List of Figures x

List of Tables xiii

List of Abbreviations xiv

List of Symbols xviii

1 Introduction 1

1.1 Motivation 1

1.2 Objective 2

1.3 Thesis outline 3

2 Background 4

2.1 Physiological basis 4

2.1.1 Cardiac cycle . . . 4
2.1.2 Respiratory cycle . . . 6
2.2 Literature survey . . . 7
2.2.1 Conventional cardio-respiratory health monitoring . . . 8
2.2.2 Radar-based vital signs monitoring . . . 13

3 Hardware Equipment & Experimental Setup 21
3.1 Ground truth . . . 21
3.1.1 Frontier X activity monitor . . . 21
3.1.2 Metronome usage . . . 23
3.2 60-GHz radar system hardware . . . 23
3.2.1 Radar architecture . . . 24
3.2.2 Full-wave electromagnetic radar simulations . . . 25
3.3 Data collection setup . . . 29

4 FMCW Radar for Cardio-respiratory Waveform and Rate Extraction 31
4.1 Digital signal processing chain . . . 31
4.1.1 Determining the target range . . . 34
4.1.2 Extracting cardio-respiratory signals . . . 36
4.2 Cardiac investigation . . . 43
4.2.1 Extraction of cardiac displacement and rate during regulated respiration . . . 43
4.2.2 Cardiac displacement and rate during a breath-hold . . . 51
4.3 Respiratory investigation . . . 58
4.3.1 Stationary respiratory displacement and rate extraction . . . 58
4.3.2 Differentiating between different breathing patterns . . . 59
4.3.3 Ambulatory respiratory displacement and rate extraction . . . 66

5 Conclusion **71**
5.1 Summary . . . 71
5.2 On-going and future work . . . 72
5.2.1 PoE radar system . . . 72
5.2.2 2.5 GHz radar system . . . 73
5.2.3 Experimental improvements . . . 74
5.3 Publications . . . 74

References **76**

APPENDICES **90**

A Digital Signal Processing Supporting Material **91**
A.1 FMCW radar fundamentals . . . 91
A.1.1 Radar system overview . . . 91
A.1.2 FMCW radar signal . . . 93
A.1.3 Radar equation and received signal . . . 96
A.2 Proof of arctangent modulation sensitivity . . . 98
A.3 Commented signal processing algorithm . . . 99

B PoE 60-GHz FMCW System **105**
B.1 System layout . . . 105
B.2 System firmware flowchart . . . 107

C 2.5 GHz FMCW Radar **109**
C.1 System layout . . . 109

List of Figures

2.1 Cardiac system overview 6

3.1 Frontier X health monitor by Fourth Frontier 22
3.2 Visual representation of RMSSD calculation 22
3.3 Summary of mm-Wave radar system used 24
3.4 Simulated radar and base PCB with and without skin volume 25
3.5 S-parameter magnitude for skin distance sweep a distance of 0.25λ (1.25 mm) to 4λ (20 mm) away from the skin 26
3.6 S-parameter phase for skin distance sweep a distance of 0.25λ (1.25 mm) to 4λ (20 mm) away from the skin 27
3.7 Radar antenna S-parameters in free space and with a skin volume 5 mm away 28
3.8 Experimental setup of 60 GHz radar and Frontier X on the torso for time synchronized data collection 29

4.1 Digital signal processing chain for cardio-respiratory waveform and rate extraction 32
4.2 Radar data cube highlighting matrix dimensions 33
4.3 Sample target detection visual summary 37
4.4 Example of phase discontinuities that must be addressed through phase unwrapping where the green path is the correct transition and the red path is the transition before phase unwrapping 39
4.5 Example of phase unwrapping with and without up-sampling. Note the sharp transition that can be captured when up-sampling the data 41

4.6 Sample spectrum highlighting different frequency components during VS extraction with RR of 10 breaths/minute, and HR of 72 beats/minute . . . 42

4.7 Radar set up on top of clothing using adhesive. Frontier X (not visible) is in contact with the skin under the shirt 44

4.8 Sample cardio-respiratory displacement waveforms during regulated breathing (subject ID = 4, regulated RR = 10 breaths/minute) 45

4.9 Sample ventricular contraction in radar and ECG signal, as well as the physiology of the relevant cardiac phase (subject ID = 4, regulated RR rate = 10 breaths/minute 46

4.10 Sample ventricular relaxation in radar and ECG signal, as well as the physiology of the relevant cardiac phase (subject ID = 4, regulated RR = 10 breaths/minute) 48

4.11 FFT of the filtered cardiac signal for one 20-second window during a regulated RR of 13 breaths/minute (Subject ID = 1, regulated RR = 10 breaths/minute) 49

4.12 Continuous HR monitoring for 120-second window (Subject ID = 1, regulated RR = 10 breaths/minute) 49

4.13 Box and whisker plot showcasing the time-averaged accuracy of the radar HR extraction for the three different regulated breathing rates 51

4.14 Sample cardiac displacement waveforms during the breath-hold investigation 52

4.15 Sample cardiac activities in radar and synchronized ECG signal (subject ID = 1) 55

4.16 Example showcasing used HRV intervals, where the R_N indicates radar intervals and E_N indicates ECG intervals (Subject ID = 1) 57

4.17 Sample respiratory waveform highlighting inhalation and exhalation periods (subject ID = 1, regulated RR = 10 breaths/minute) 59

4.18 FFT of the filtered respiratory signal for one 20-second window during a regulated RR of 10 breaths/minute (Subject ID = 1) 60

4.19 Continuous RR monitoring (Subject ID = 1) 60

4.20 Box and whisker plot showcasing the time-averaged accuracy of the radar RR extraction for the three different regulated breathing rates 62

4.21 Sample respiratory displacement waveforms highlighting various types of breathing . . . 65
4.22 Row-normalized confusion matrix of different breathing types to display the true positive rates . . . 66
4.23 Zoomed-in sample extracted continuous respiratory chest displacement for treadmill exercises (Subject ID = 1) . . . 68
4.24 Zoomed-in sample extracted continuous RR for treadmill exercises (Subject ID = 1) . . . 68
4.25 Percent of extracted RR from the radar (left) and Frontier X (right) a certain number of breaths per minute away from the ground truth metronome at treadmill speeds of 1.5 MPH and 3.0 MPH . . . 70

A.1 Radar system and waveform overview. . . . 92

B.1 System layout for high-speed radar system highlighting signals between different chips as well as power up voltages. . . . 106
B.2 PoE radar custom PCB top and bottom view. . . . 106
B.3 Firmware flowchart for PoE radar. . . . 108

C.1 radio frequency (RF) front end system diagram. . . . 110
C.2 Low-frequency radar custom PCB top and bottom view. . . . 110
C.3 Magnitude (left) and phase (right) of 25-dB coupler . . . 112
C.4 Patch antenna design. . . . 113
C.5 Simulation of a single antenna with varying tissue layer thickness . . . 114
C.6 Simulation of two antennas on top of skin with varying separation distance 115
C.7 Simulation of two antennas on top of muscle with varying separation distance 116

List of Tables

3.1 Radar parameters used for system 30

4.1 Participants in regulated breathing and breath-holding investigations . . . 43

4.2 Metrics extracted from radar cardiac waveform versus expected values from ECG during regulated breathing 50

4.3 Metrics extracted from radar cardiac waveforms versus expected values from ECG during breath-hold 56

4.4 Sensitivity of HR and HRV to position of radar on the chest 57

4.5 Metrics extracted from radar respiratory waveform versus expected values from metronome during regulated breathing 61

4.6 Breakdown of participants in ambulatory and breath-type investigations . . 63

4.7 Thresholding statistical parameters 64

C.1 Summary of antenna parameter values. 112

C.2 Summary of RF front end design. 118

List of Abbreviations

AD arctangent demodulation 38

ADC analog-to-digital converter 23, 32, 44, 77, 93, 95, 103

AV atrioventricular 5, 45, 47, 52–54

BCG ballistocardiograms 8, 9

BPF bandpass filter 18, 42, 43, 51, 58

CAT-5 Category-5 91

COPD chronic obstructive pulmonary disease 1, 7

CVD cardiovascular diseases 1

CW continuous wave 2, 13, 14, 18–20, 73, 74

CWT continuous wavelet transform 16

DFT discrete-time Fourier Transform 18

DSP digital signal processing 16, 19, 24

ECG electrocardiogram 1, 2, 11, 13, 14, 19, 21, 43–47, 51–54, 56, 71, 72, 74

EDR ECG derived respiration 11

EMD empirical mode decomposition 16

EWT empirical wavelet transform 16

FFT fast Fourier transform 14, 15, 17, 35–38, 42, 47, 54, 59, 67

FIFO first-in-first-out 23

FIR finite-element response 40, 42, 43, 51, 58

FMCW frequency modulated continuous wave 2, 3, 14–18, 23, 25, 31, 52, 71, 77, 81–83

FOV field of view 2, 17, 34

FTPR frequency-time phase regression 14

HBI heartbeat intervals 22

HR heart rate 1, 2, 7, 8, 12–14, 16–19, 21, 29, 38, 42–44, 47, 49, 50, 54, 56, 72

HRV heart rate variability 1, 2, 21, 22, 29, 43, 44, 54, 56, 72

HVD Hilbert vibration decomposition 16

IF intermediate frequency 29, 80, 95, 103, 104

ILO injection-locked oscillator 20

IMD inter-modulation 38

IQ in-phase and quadrature 19, 24

ISAR inverse synthetic aperture radar 16

LED light-emitting diode 12

LNA low-noise amplifier 23, 77, 99, 104

LO local oscillator 38, 97, 103

LPF lowpass filter 25, 40, 103

MCU microcontroller unit 23, 73, 91, 93

MIMO multiple input multiple output 17

mm-Wave millimeter-Wave 2, 18, 28, 37, 80

MUSIC multiple signal classification 17

PA power amplifier 23, 77, 97, 104

PCG phonocardiogram 2, 12–14, 74

PLL phase-locked loop 23–25

PoE power over ethernet 72, 73, 91, 93

PPG photoplethysmogram 12

PPG phonopneumogram 12

RBM random body movement 2, 15–19, 71

RCS radar cross-section 82–84

RF radio frequency 23, 29, 35, 79, 95–97, 103, 104

RIP respiratory inductive plethysmography 10, 12

RMSE root mean squared error 17, 19

RMSSD root mean square of the successive differences 21, 22, 56

RR respiratory rate 2, 7–10, 13, 14, 16–19, 21, 23, 29, 38, 42, 44, 49, 58, 59, 67, 69, 71, 72

RX receiver 23, 25, 26, 32, 44, 77, 83

SA sinoatrial 5

SCG seismocardiograms 8, 9

SILO self-injection-locked oscillator 20

SNR signal to noise ratio 19, 24

SPI serial peripheral interface 91, 93, 95, 103

TCP transmission control protocol 91, 93

TX transmitter 23, 26, 77, 83

UTP unshielded twisted pair 91

VCO voltage-controlled oscillator 23, 25, 77, 95, 97, 104

VGA variable-gain amplifier 23

VS vital signs 2, 7, 13–17, 19, 34, 36, 82

WHO World Health Organization 1

List of Symbols

B Bandwidth: The frequency range for the radar chirp 77, 79

f_{beat} Beat-frequency: Radial frequency of the down-converted beat signal in Hz 35, 36, 81

x_{beat} Beat signal: Received echo signal after down-conversion and filtering 32, 34, 35, 37, 80

K Chirp slope: The rate of change of the bandwidth over a single chirp duration (the bandwidth divided by the chirp time) 32, 36, 77, 79, 80

T_C Chirp time: The duration of a single chirp 35, 77, 79

τ Delay time: round trip time for chirp signal 36, 77, 79, 80

t_f Fast time: The sampling time within a chirp in a given frame 32, 34, 35, 77, 79

f_R Frame rate: Rate of frame acquisitions in Hz 38, 42

T_R Frame time: Time duration to acquire a single frame (including all samples, for all chirps) 37, 38, 77, 79

T_i Idle time: Time duration between chirps 77

c Speed of light: A constant describing the speed of light 299,792,458 m/s 36, 80

f_{max} Maximum frequency: Upper bound on chirp bandwidth or linear frequency sweep 79

λ_{max} Maximum wavelength: Wavelength associated with minimum chirp frequency 35, 79

f_{min} Minimum frequency: Lower bound on chirp bandwidth or linear frequency sweep 35, 79

λ_{min} Minimum wavelength: Wavelength associated with maximum chirp frequency 79

ϕ Phase noise: Random fluctuation in the phase of the signal, expressed in radians, which can degrade the performance of the radar system 35, 79–81

ω_{beat} Radial beat-frequency: Radial frequency of the down-converted beat signal in radians per second 32, 80

A_{RX} Received signal amplitude: The amplitude of the received chirp signal 34, 79

f_S Sampling frequency: Radar sampling frequency in fast time 32, 35, 36

t_s Slow time: The sampling time across different chirps in a given frame (i.e., the chirp index) 32, 34, 35, 77, 79, 80

R_0 Target distance: Position of the target, in this case, the chest from the radar 34–36, 79, 80

Δd Target vibration: Vibration of the target due to cardio-respiratory activity 34, 36, 38, 42, 79

A_{TX} Transmitted signal amplitude: The amplitude of the transmitted chirp signal 34, 79

θ_1 Cardio-respiratory phase: Phase component in beat signal associated with cardio-respiratory activity detected on the chest 38, 80, 81

Chapter 1

Introduction

1.1 Motivation

With the increasing prevalence of cardiovascular and respiratory diseases worldwide, monitoring these vital systems is integral to assessing individual health. Cardiovascular and respiratory diseases are major global health concerns, contributing significantly to morbidity and mortality rates. According to the World Health Organization (WHO), cardiovascular diseases are the leading cause of death worldwide, accounting for approximately 17.9 million deaths annually [1]. In fact, WHO estimated that 32% of all deaths worldwide are caused by cardiovascular diseases (CVD) [2]. Similarly, respiratory diseases, including chronic obstructive pulmonary disease (COPD) and asthma, affect millions of people globally as their prevalence has increased by 39.8% since 1990, thus, substantially increasing healthcare costs and reducing individual quality of life [3, 4, 5]. Monitoring cardiopulmonary health, in general, is of particular importance following the recent COVID-19 pandemic, as recent studies point to decreased cardiovascular and pulmonary performance following COVID-19 infection, particularly in the older adult populations and demographics with diagnosed comorbidities [6].

Conventional gold-standard methods, including electrical-based techniques like electrocardiogram (ECG)s, provide cardiac conduction information throughout the cardiac cycle enabling extraction of metrics like heart rate (HR) and heart rate variability (HRV). However, clinical ECG acquisition methods are complex, as they typically require 12–15 electrodes placed precisely on the body, cause skin burns and irritations due to the use of coupling hydrogels, and are incompatible with long-term continuous monitoring as patients are required to remain still and supine for the duration of the data collection period [7, 8].

Similarly, spirometry is a commonly employed technique for performing functional respiratory tests to diagnose respiratory conditions and gauge responses to different treatment methods [9]. Nonetheless, this method heavily relies on patient cooperation and effort to obtain dependable results, posing difficulties for specific populations, including young children or individuals with cognitive impairments. Furthermore, spirometry does not offer continuous measurements of respiratory rate (RR) and other respiratory, particularly during physical exercise [10].

Contactless radar-based monitoring of vital signs (VS) using continuous wave (CW) radars can capture millimetre-scale respiratory and heartbeat vibrations on the chest, as well as detailed micrometre-scale displacements resulting from the repetitive closure of cardiac valves throughout the heartbeat, clinically referred to as "heart sounds" [11, 12]. Such functional information is not electrical-based and cannot be extracted using an ECG, instead, this information is detected by an acoustic-based method like phonocardiogram (PCG). Contactless frequency modulated continuous wave (FMCW) radars have also been widely used for cardio-respiratory displacement waveform and rate detection [13, 14, 15]. FMCW radars are desirable due to their simple architecture, customizable resolution, ability to provide both distance and velocity data, and continuous signal acquisition [16]. In particular, millimeter-Wave (mm-Wave) systems possess high sensitivity to heartbeat and breathing vibrations due to their shorter wavelength. However, these methods are subject to several challenges such as random body movement (RBM) of the target, the presence of multiple targets in the field of view (FOV) to the detriment of accuracy, multi-path and noise sources that distort the VS waveform, limited VS acquisition to the FOV of the radar, as well as challenges extracting the cardiac information due to the overlap with higher-order respiratory harmonics [16, 13].

1.2 Objective

The primary goal of this thesis is to explore a system capable of extracting both cardiac and respiratory displacement waveforms. These radar displacement waveforms must provide comprehensive detail and be correlated with the ground truth signal acquired from conventional cardio-respiratory monitoring systems to establish a physiological basis for the radar displacement-based signal. Specifically, for radar cardiac displacement waveforms, different segments of the cardiac cycle should be identified, while for radar respiratory displacement waveforms, inhalation and exhalation periods should be distinguished. The extracted waveforms will then be utilized to derive valuable metrics, including HR, RR, and HRV. Additionally, the system should differentiate between breathing patterns (e.g.,

normal, laboured, apnea) and extract respiratory metrics during exercise.

1.3 Thesis outline

The structure of this thesis is as follows:

- Chapter 2: Background information regarding the cardiac and respiratory cycles, a literature survey for conventional and radar-based cardio-respiratory monitoring techniques, and the basics of FMCW radar signal.
- Chapter 3: Radar system and ground truth devices used, the experimental setup, and full-wave electromagnetic simulations to verify near-field radar operation.
- Chapter 4: A proposal of the cardio-respiratory waveform and rate extraction algorithm, as well as the results of the extracted signals and rates.
- Chapter 5: Closing remarks and system limitations, and recommendations for system performance improvements.

Chapter 2

Background

2.1 Physiological basis

The primary objective of this chapter is to assess the diverse sensing methodologies employed for observing the activities of the heart, lungs, or both. Each modality relies on a specific physiological effect that is measurable in a *non-invasive* manner. To facilitate a comprehensive understanding of the available sensing modalities, we must first delineate a set of frequently utilized physiological signals that manifest as a result of cardiac or pulmonary activity.

2.1.1 Cardiac cycle

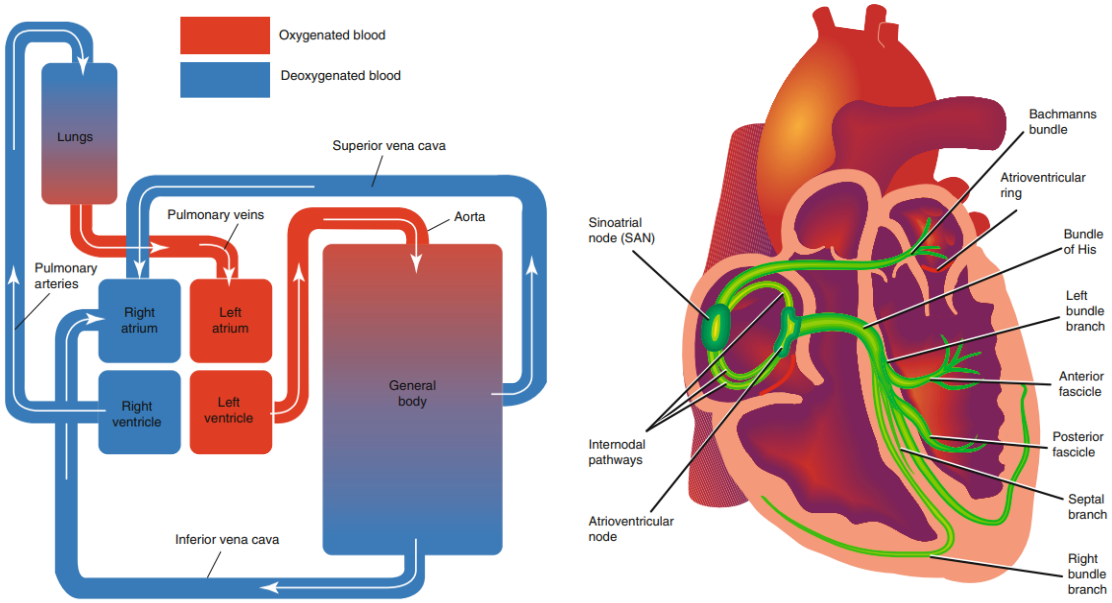
The heart is a complex organ responsible for the circulation of blood throughout the body. The mechanics of the heartbeat involve a series of events that result in the coordinated contraction of the myocardial (i.e., cardiac muscle) cells, and the synchronized opening and closure of the different cardiac valves. The cardiac cycle can be divided into two phases: The diastole and systole [17]. The diastole is the relaxation phase of the cardiac cycle. During diastole, the heart's chambers (atria and ventricles) are in a state of relaxation, and blood flows passively into the heart. The atria fill with blood from the veins, and the ventricles relax and expand, allowing for optimal blood filling. The diastole is often associated with the resting phase of the heart. On the other hand, systole is the contraction phase of the cardiac cycle. During systole, the heart's chambers actively contract to pump blood out of the heart. The atria contract first, pushing the remaining blood into the

ventricles. Then, the ventricles contract forcefully, pumping blood out of the heart and into the arteries. Systole is responsible for the ejection of blood from the heart and is often associated with the working phase of the heart. The flow of oxygenated and deoxygenated blood can be observed in Figure 2.1a.

The process of the heartbeat is initiated by an electrical signal that originates in the sinoatrial (SA) node, which is located in the right atrium of the heart as seen in Figure 2.1b. The SA node is known as the natural pacemaker of the heart, and it generates an electrical impulse that spreads through the atria, causing them to contract [18]. As the electrical signal spreads through the atria, it reaches the atrioventricular (AV) node, which is located in the inter-atrial septum between the atria. The AV node serves as a gatekeeper, slowing down the electrical signal to allow the atria to contract fully and empty their contents into the ventricles. The delay between atrial and ventricular contraction allows for efficient filling of the ventricles and optimization of cardiac output [18, 19]. After passing through the AV node, the electrical signal travels down the bundle of His, which is a specialized conduction pathway that divides into the left and right bundle branches. The branches travel down the interventricular septum and towards the apex of the heart, where they terminate in the Purkinje fibres. The Purkinje fibres are specialized cells that rapidly transmit the electrical signal throughout the ventricles, causing them to contract in a coordinated manner and eject blood out of the heart. In addition, the movement of blood through the heart is controlled by four valves: the tricuspid valve, the pulmonary valve, the mitral valve, and the aortic valve. These valves ensure that blood flows in the correct direction through the heart, preventing back-flow or regurgitation. The tricuspid valve and mitral valve control the flow of blood between the atria and ventricles, while the pulmonary valve and aortic valve control the flow of blood out of the heart and into the pulmonary and systemic circulations, respectively [17, 19].

Understanding the mechanics of the heartbeat is essential for the diagnosis and management of various cardiac conditions, including arrhythmia, valve disorders, and heart failure [20]. The electrical activity generated by the collective cardiac muscle cells is projected onto the body surface, resulting in a measurable signal that can give insight into cardiac health. Such signals can evaluate the regularity and timing of the cardiac conduction [21]. Moreover, the intricate dynamics of the heart due to chamber and value movement along the beat progression contribute to displacements and vibrations that are detectable on the surface of the body. As the heart contracts and relaxes with each beat, it undergoes motion and deformation, resulting in subtle movements of adjacent structures. These movements propagate to the body surface, producing both discernible displacements and acoustic signals that can be detected and quantified. In addition to the cardiac motion, the propagation of the pulse wave throughout the body also influences surface displace-

ments. The pulse wave, generated by the rhythmic ejection of blood from the heart, travels along the arteries, causing a pulsatile effect in the limbs and neck. This pulsation, in turn, induces vibrations and oscillations in the body surface away from the chest, which can be observed and analyzed to infer cardiovascular activity.



(a) Blood flow through human body [22] (b) Cardiac conduction system for regulating heartbeat [22]

Figure 2.1: Cardiac system overview

2.1.2 Respiratory cycle

Respiration involves a complex set of mechanics to facilitate the expansion and relaxation of the lungs. The lungs are highly specialized, spongy organs located within the thoracic cavity enclosed by a thin, flexible membrane known as the pleura [23]. The process of inhalation is initiated by the contraction of the diaphragm and external intercostal muscles, which are located on the outer surface of the rib cage and are responsible for elevating the ribs during inhalation, therefore, expanding the chest cavity and increasing the lung volume. The resultant decrease in intrapulmonary pressure, also known as alveolar pressure (i.e., the pressure within the sac-like structures known as alveoli in the lungs), creates a

negative pressure gradient which drives airflow into the lungs. This process is essential to the efficient exchange of gases in the alveoli, where oxygen diffuses into the bloodstream and carbon dioxide is removed [24].

Exhalation, on the other hand, is primarily a passive process in healthy individuals and is initiated by the relaxation of the diaphragm and internal intercostal muscles, which causes the chest cavity to decrease in size by depressing the ribs, thus decreasing the volume of the chest cavity and causing the lungs to expel carbon dioxide-rich air [23]. However, during forced exhalation, the internal intercostal muscles and abdominal muscles can also contract to further decrease chest cavity size and increase the pressure within the lungs, thus allowing for more forceful expulsion of air [24]. These mechanical processes are necessary for the efficient functionality of the respiratory system, and any disruption can result in respiratory difficulties. For example, conditions such as asthma or COPD can impair the mechanics of respiration by causing inflammation or constriction of the airways, leading to decreased lung function [23, 24].

The mechanics of breathing and lung function are important factors in monitoring VS, especially in critically ill patients. The RR, or the number of breaths taken per minute, is a key indicator of a patient's overall health status and can be affected by a range of conditions. The respiratory cycle entails substantial changes in lung size, causing noticeable movements of the torso surface that can be readily observed without the aid of any instruments [21]. As the lungs expand and contract during inhalation and exhalation, the displacement of the torso becomes apparent, manifesting as a visible rise and fall of the chest and abdomen. By capturing and analyzing these displacements and vibrations of the body surface, it becomes possible to gain insights into the respiratory system's health as well as deviations from any expected variations.

2.2 Literature survey

There are five VS that are integral to fully assessing and monitoring health status. They include body temperature, HR, RR, blood pressure, and oxygen saturation [25]. It is essential to understand the utility of VS in characterizing illnesses. For example, the HR and RR are fundamental metrics in diagnosing individuals with a high risk of sudden cardiac arrest, in which a patient's heart stops pumping blood and their breathing becomes abnormal [20]. The HR and RR are also of particular importance for athletic performance, with both being integral indicators of exercise-induced fatigue and dyspnea [26]. As such, they can be used as guidelines for adjusting the intensity and duration of exercise to prevent adverse effects. Nevertheless, it is important to realize that while HR and RR

are good foundational biometrics in terms of characterizing cardiovascular and pulmonary health, they do not provide a comprehensive overview of the underlying organ functionality, and as such are limited in the amount of information they can provide. To interrogate organ complex organ functionality described in the previous section of this chapter, one must observe the electro-mechanical behaviours of the heart during a heartbeat and the mechanical activity of the lungs during respiration, and any other additional biometrics that can be extracted from them.

2.2.1 Conventional cardio-respiratory health monitoring

Manual observation

Perhaps the most obvious method of detecting cardio-respiratory rates is through manual observation [27]. Typically, the measurement of the RR occurs during a resting state and involves observing the rise of the chest and counting the number of breaths in one minute. The HR is measured by feeling for the pulsations on the patient's neck, where the carotid artery is, or on the inside of their wrist. The number of beats felt within a one-minute time frame is counted. Alternatively, if time constraints exist, the beats are counted for 30 seconds, and the count is multiplied by two to derive the heart rate per minute. An attempt at accuracy is maintained by consistently counting the breaths or beats while focusing on the physical modulation, however, this method is very inaccurate, and cannot provide a continuous reading of cardio-respiratory rates [27]. Moreover, this is a very surface-level assessment of health, with no additional biometrics, or underlying organ functionality.

Displacement-based methods

Displacement-based methods for observing cardio-respiratory health are numerous and vary in their ability to continuously measure both cardiac and respiratory signals, but work mostly by monitoring chest displacements due to breathing and heartbeat. For example, ballistocardiograms (BCG) and seismocardiograms (SCG) are non-invasive techniques used to measure and analyze cardiac activity [28]. BCG utilizes sensors, such as ballistocardiographs or accelerometers, to detect the mechanical forces and body movements resulting from the heart's contraction and provide information regarding the HR, stroke volume, and cardiac output. Nevertheless, this method requires integration into a bed, chair, or scale that the patient will be in constant contact with to facilitate continuous monitoring [29, 30, 31, 32, 33]. SCG, on the other hand, uses motion sensors placed on the chest wall to capture the vibrations caused by cardiac contractions [34]. SCG allows analysis

of cardiac timing intervals and monitoring of cardiac performance, which can be a helpful diagnostic tool, but does not provide detailed waveforms of chest displacement due to the heartbeat [34, 35, 36, 37]. Although BCG and SCG are non-invasive and provide insight into cardiac dynamics, both techniques require careful placement of sensors that are highly susceptible to noise artifacts from undesired movements, which places limitations in terms of widespread clinical adoption and availability for continuous ambulatory monitoring. It is worth noting that although not meant for respiratory monitoring, both methods can capture breathing motion artifacts which can be translated into the RR [36]. SCG and BCG are fraught with calibration complexities, placement restrictions, and a large susceptibility to noise. Additionally, their inability to provide a complete screening of heart and lung functionality limits their use in non-research environments and clinical settings.

Strain gauges are another displacement-based method for measuring the displacement and vibrations of the chest. Strain gauges work by measuring strain in the chest through the use of a thin wire or foil that changes its electrical resistance when subjected to mechanical stress [38]. When attached to the chest for respiratory measurements, the strain gauge detects the expansion or contraction of the chest during breathing, converting it into changes in electrical resistance or capacitance [39, 40]. These changes are then converted into RR and volume measurements using appropriate signal processing techniques. Strain gauges can be good indicators of cardiac health parameters such as blood pressure, but aren't able to provide detailed timing or functional information [41]. Using strain gauges for cardio-respiratory measurement has certain limitations including their small and precise measurement area, need for multiple sensors for displacement measurements, potential skin irritation due to slippage from the torso, sensitivity to noise due to movement, calibration challenges, restricted measurement range, and incompatibility with ambulatory measurements [42, 43, 44, 45, 46]. Moreover, many strain gauges can lack the sensitivity to capture the cardiac vibrations, as they are often dominated by the large amplitude of the respiratory vibrations.

A similar option that is prominent in literature for displacement-based detection is piezoelectric sensing. Piezoelectric sensors and strain gauges are similar in that they both provide measurements based on mechanical deformation. While strain gauges rely on the change in resistance due to strain, piezoelectric sensors generate an electrical charge in response to deformation [47]. Both sensors can be used to measure forces, strains, or vibrations in various healthcare applications. However, unlike strain gauges, piezoelectric sensors do not require direct physical contact with the object or body being measured, offering a contactless sensing option as cardio-respiratory behaviour can be captured through a highly sensitive transducer [48]. This makes these sensors more sensitive to cardiac vibrations resulting from the heartbeat. Nevertheless, piezoelectric sensors require calibration

and are sensitive to noise as a result of movement. These downsides can affect the accuracy and reliability of measurements obtained through these sensors. As a result, these methods are also not widespread in clinical use.

Another displacement-based method, respiratory inductive plethysmography (RIP), is a non-invasive technique that measures changes in thoracic and abdominal volumes during respiration using elastic bands embedded with inductive coils placed around the chest and abdomen [38, 49]. RIP offers several advantages which include providing a global assessment of respiratory movements by capturing both thoracic and abdominal volumes as well as real-time monitoring of respiratory parameters, such as tidal volume and breathing pattern. Nevertheless, RIP bands often suffer from slippage and are not advisable to use during exercise, on those with sensitive skin, and young children as skin irritation is common, as is the case with most skin-contact-based sensors [46, 44]. The method also requires proper calibration, which can be time-consuming as correct sensor placement is essential for accurate measurements, with external factors like motion artifacts and electromagnetic interference introducing ample noise [50]. Additionally, RIP systems can be relatively expensive and bulky, limiting accessibility in certain settings [51].

The final displacement-based method, spirometry, serves as the gold standard for respiratory diagnosis and monitoring in clinical settings. Spirometry facilitates standard pulmonary functional tests that measure the volume and flow of inhaled and exhaled air as an individual performs various respiratory maneuvers using a spirometer, a device that records the changes in airflow and lung volumes [52]. The primary advantage of spirometry is its ability to assess parameters such as respiratory flow rates, as well as lung volumes and capacities for various points of inhalation and exhalation [52, 53]. Spirometry is widely used in diagnosing and monitoring respiratory conditions, evaluating the severity of lung diseases, and assessing treatment responses [9]. However, this method requires patient cooperation and effort to achieve reliable results, making it challenging for certain individuals, such as young children, individuals with cognitive impairments, and those with respiratory conditions such as asthma. Moreover, this method does not provide continuous measures of RR and other respiratory volumes and rates. In addition, variations in testing techniques or effort due to muscle weakness can affect the accuracy and reproducibility of the measurements [10]. It is important to note that both RIP and spirometry cannot capture cardiac functionality, and are the gold standard for respiratory monitoring only.

Electrical-based methods

Other conventional cardio-respiratory sensing methods rely on utilizing the electrical signal produced by the heart. These modalities are driven in part by the understanding that

human skin has the unique characteristic of being partially conductive [21]. One such method, which is the gold standard for cardiac monitoring, is the ECG. The conventional clinically prevalent 12-lead ECG is a visual depiction of the electrical impulses generated by myocardial excitation [54]. Its operation involves the identification of these electrical signals using a collection of passive terminals known as leads, strategically positioned on the patient's skin. Each lead consists of two electrodes, a positive and a negative, that measure the voltage difference produced by the depolarization and re-polarization of the cardiac muscle [55]. By combining the data from all 12 leads, which are placed in specific positions on the body, a comprehensive and detailed representation of the heart's electrical activity is obtained, enabling the diagnosis and assessment of various cardiac conditions [56]. Although not optimized for this purpose, it is possible to extract functional respiratory signals from ECG, often referred to as ECG derived respiration (EDR) signals.

Nevertheless, ECGs come with many functional limitations despite being the gold standard for cardiac health monitoring. In particular, patient movement is restricted throughout the measurement duration due to the effect of motion artifacts on signal quality, which necessitates supine positioning and limits measurement sessions to around 10 minutes [57, 7]. Moreover, ECGs are expensive and can lack sensitivity and accuracy in detecting subtle abnormalities, especially in patients with obesity or chest deformities [58]. Moreover, while ECG is ideal for detecting conduction cardiac disorders, such as arrhythmia and ischemia to name a couple, it cannot detect mechanical, muscular, or valvular cardiac disorders [59, 11]. Another major limitation of this modality is the prevalent skin sensitivity to the hydro-gel used for improving electrode coupling to the skin, which can cause discomfort or skin reactions, compromising electrode placement and accuracy [8].

An alternative to conventional ECG is capacitive ECG which does not require any direct skin contact, eliminating skin irritation as electrodes can now be embedded in textiles [21, 60]. Nevertheless, aside from being highly sensitive to movement artifacts and requiring precise placement, it involves added complexities when washing the device after use [61]. Finally, wrist wearable systems (i.e., Apple Watch, Fitbit) offer an accessible alternative to conventional ECGs and do not require additional care instructions such as washing [62]. Nevertheless, the ECG feature on such wearables is a single-lead ECG, which limits its ability to detect certain cardiac conditions or provide a comprehensive assessment compared to a traditional 12-lead ECG [63]. Such wearables have a high risk of false positives, with a study finding that only 34% of participants who received an irregular pulse notification from an Apple watch were ultimately diagnosed with atrial fibrillation [64]. Moreover, the quality of ECG is still heavily influenced by factors such as improper placement of the electrode, movement artifacts, or signal interference that plague conventional ECG methods.

Optical-based methods

Another category for conventional cardio-respiratory monitoring is optical sensing-based methods. These methods do not interrogate displacement or electrical activity directly caused by respiration or heartbeat, instead using the visible segment of the electromagnetic spectrum, they can interrogate finer secondary changes associated with electro-mechanical cardio-pulmonary activity. One such example is a variation of the aforementioned RIP, commonly known as the photoplethysmogram (PPG), which uses a light-emitting diode (LED) and a photodetector embedded in a pulse oximeter at the surface of the skin to measure the volumetric variations of blood circulation [65]. PPG has the advantage of being a cost-effective way of continuously monitoring the HR, and has a very small footprint (it is often a clip-house sensor placed on the index finger) [66]. This method is also capable of extracting cardiac waveforms and can be used to detect conditions such as premature ventricular contractions, ventricular tachycardia, and ventricular fibrillation [67, 68]. Moreover, investigations have been conducted for breathing rate estimation and extracting spirometry-like breathing waveforms from PPG when placed on various areas of the body, such as in the ear [69, 70]. Nevertheless, it is important to consider some limitations of this modality starting with highly subjective signal quality depending on conditions such as bad circulation, hypothermia, and physical factors such as skin pigmentation, tattoo ink, or excessive hair [67, 71]. PPG primarily measures changes in blood volume in superficial tissues, such as the fingertip or earlobe, making it unsuitable to capture physiological changes in deeper tissues and limiting its applicability for certain measurements [72]. Finally, PPG readings can be affected by motion artifacts caused by movement or muscle contractions, ambient light, temperature, and other environmental factors which introduce noise and affect the accuracy and reliability of the measurements [73, 71].

Auscultation methods

The final category for conventional cardio-respiratory monitoring is auditory methods such as the PCG and the phonopneumogram (PPG) (not to be confused with the photoplethysmogram in the previous paragraph). These methods are a graphical or digitized representation of the sounds produced by the cardiac valves during the cardiac cycle and respiratory sounds during inhalation and expiration, respectively [74, 75]. PCGs are the clinical gold standard for detecting abnormal heart sounds which can be indicative of valve disorders, heart murmurs, or structural abnormalities [76]. Likewise, PPGs are often the first tool used to assess functional respiratory health as they can determine breath intensity, exhalation and inhalation duration, and different breathing abnormalities [77]. PCG and PPG

are inexpensive and non-invasive techniques that do not require complex equipment, allowing for early identification and intervention [78]. Devices are often compact, and easier to operate than other methods such as ECG or spirometers, making them convenient for use in different clinical settings by healthcare professionals with minimal training [79]. The strong suit of these two methods is providing complementary information to gold-standard methods such as ECG and spirometry, enhancing the overall assessment of cardiac health, rather than acting as a stand-alone assessment tool [80]. Nevertheless, these methods are also laden with some limitations, the main one being that interpretation of the recordings is highly subjective and requires trained expertise due to background noise, artifacts, and variations in cardiac and pulmonary sounds between subjects [81]. Additionally, PCG in particular primarily focuses on assessing valvular heart disease at a snapshot in time during the assessment period and may not provide a comprehensive continuous evaluation of other cardiac parameters such as electrical, mechanical, and structural abnormalities [82].

2.2.2 Radar-based vital signs monitoring

Contactless (far field) radar-based monitoring

Radar-based VS monitoring systems have been steadily growing in popularity due to their ability to measure biological data in a continuous, unobtrusive, and safe manner [13]. Radars can use various frequency bands and work by transmitting harmless low-power electromagnetic waves and accurately analyzing their reflections [83]. Different radar signals can probe different characteristics of the reflected echo signal, including the frequency shift, phase shift, and delay time, for capturing VS. Far-field contactless radar systems have been widely used for various health-focused applications including sleep apnea diagnosis, HR detection, RR detection, and even recreating ECG-like signals of cardiac mechanics during the cardiac cycle [84, 85, 14, 86, 87]. Moreover, these systems offer the advantage of eliminating contact with the skin and the need for coupling hydrogels, thus minimizing skin burns and irritation and other limitations on data acquisition periods prevalent with other methods like ECG [8, 88]. Additionally, their unobtrusive nature means that they do not require the intense active patient participation that is required for methods such as spirometry, making them more appropriate for older adults, young children, and those with cognitive impairments [10].

The most basic radar system is the CW radar, which operates by continuously transmitting an unmodulated electromagnetic signal and measuring the phase and frequency shift of the reflected echo [89]. These radars are simple, cost-effective, and able to provide accurate velocity measurements making them well-suited for short-range applications and

VS detection. When compared to other radar systems such as pulsed-radars, which transmit short-duration pulses and utilize the time delay of the echo from a target to determine the range, CW systems bypass the issue of target range ambiguity [90, 89]. This issue arises when the radar encounters targets that are located at distances greater than the maximum range that can be unambiguously resolved, as echoes from distant targets can arrive back at the radar after the next pulse has already been transmitted, causing ambiguities in determining the true range. CW radar is not affected by target range ambiguity, as it continuously transmits and receives signals. Nevertheless, these CW radars cannot provide range information unless advanced signal processing techniques are employed. They are also susceptible to interference from nearby objects or surfaces, which can affect the accuracy of range measurements.

Nevertheless, it is possible to use CW radars for VS detection. In the work by Nosrati *et al.* a phased array 2.4 GHz CW radar system was utilized to monitor the VS of two targets [91]. The antenna array was specifically designed to generate two beams at different angles. The proof-of-concept radar system employed a 4-element linear array for both transmission and reception. The beams were directed at angles of 25° and -35° relative to the antenna's central axis. This configuration allowed for the differentiation of the phase signatures of two subjects positioned within the field of view of the separate beams. The system was tested on two subjects, primarily focusing on detecting RR, while the detection of HR and any functional waveforms were neglected. The same group utilizes a CW operating at 2.4 GHz to enhance the acquisition of the heart signal by applying a technique involving the second derivative of the received phase [92]. To achieve this, they apply a filter characterized by the frequency response of ω^2 on the input signal, thereby amplifying the higher frequencies associated with the HR. Notably, an improvement in accuracy of approximately 10% is observed by employing the frequency-time phase regression (FTPR) method as an alternative to the commonly used fast Fourier transform (FFT).

Michler *et al.* used a 24 GHz interferometric CW radar system with a 1 μm distance accuracy placed at a distance of 40 cm in front of the human chest to detect not only HR (93.14% accuracy) and RR (0.828% error), but their waveforms as well [12]. This investigation extracts the heart sounds (typically extracted using a PCG) using a radar and maps them against an ECG ground truth. Nevertheless, this approach employs a six-port receiver design that adds some complexity to the system design. The same system is validated for accurate detection of heart sounds S1 and S2 compared to a synchronized PCG, showing an 83% and 81% correlation, respectively, as well as accurate heartbeat detection against a synchronized ECG and PCG signal with a 92% and 94% F1 score, respectively, which indicates high system detection accuracy [11].

The investigation in this thesis is particularly interested in FMCW radar systems,

as such it is crucial to understand their advantages and limitations over other methods. FMCW radars, in particular, are very desirable due to their relatively straightforward architecture, their customizable resolution, and their ability to provide both distance and velocity data [83]. These systems modulate the frequency of the transmitted signal at a known rate over a fixed period; two common modulations are triangular and sawtooth schemes referred to as chirps [83, 16]. FMCW radars provide distance information by comparing the transmitted and received signals to determine the difference in frequency due to the distance travelled by the signal. This is accomplished by taking the FFT of the down-converted received signal to reveal the position of a target at a certain range bin with maximum amplitude. Although velocity information can be extracted due to the Doppler frequency (i.e., because of the Doppler effect of a moving object), displacement of the chest due to the heartbeat and breathing is often too small to be detected in the Doppler information [89]. Instead, these vibrations are embedded in the phase changes of the maximum range bin where the target exists.

However, the widespread adoption of contactless FMCW radars as health monitoring devices face numerous challenges. The accurate detection of human VS is essential for their successful implementation, yet it proves to be a significant hurdle due to the data being embedded within minor phase changes within a specific range bin. Consequently, these radar systems become highly sensitive to environmental factors, with RBM being a notable challenge [93]. RBM introduces additional noise and interference, overwhelming the VS. Additionally, factors such as the presence of multiple occupants in the detection area, the desire for accurate ambulatory measurement, and the influence of high-order VS harmonics, such as the effect of high-order respiratory harmonics on cardiac waveforms, add further complications [94, 16, 14]. Therefore, the removal of these environmental variables becomes imperative to enhance the accuracy of VS estimation.

Techniques have been implemented to combat the previously outlined limitations of FMCW radars. The first discussed issue of RBM as well as the presence of artifacts and noise and their effect on the accuracy of the detected VS has been addressed using a combination of improving signal processing techniques and altering radar-based sensing system design. Some far-field radar investigations focus on improving the system hardware through the addition of sensors, such as a camera, to radar-based detection systems for phase compensation to address the effect of RBM on the accuracy of VS detection [95]. The cited investigation by Gu *et al.* successfully utilizes both the radar signal and the camera-based visual signal to detect chest displacement waveforms due to respiration and heartbeat. Nevertheless, not only does the use of camera systems increase system complexity, but it also raises privacy concerns, as individuals may object to continuous monitoring during their activities.

Other radar systems focus on detecting and reducing RBM by using multiple radars in different orientations. For example, the work by Muñoz-Ferreras *et al.* proposes the use of two FMCW radar systems, each targeting opposite sides of the test subject, for RBM suppression [96]. The main operating assumption is that the RBMs are detected as moving towards one radar and away from the other at a given time, whereas the chest movement due to the heartbeat and respiration will appear as moving toward both radars and away from both radars at a given time, due to the radial displacement of the torso during respiration and heartbeat. This paper suggests that by tracking the range histories obtained by each radar sensor, the VS can be accurately obtained by tracking the migration of the detected RBM through different bins, a method commonly used for improving the quality of inverse synthetic aperture radar (ISAR) images [97]. Although the system successfully extracts the RR and HR accurately, the validation is performed on simulated RBMs and cardio-respiratory rates. Moreover, an obvious limitation to the setup is the increased system complexity with the necessity to accurately synchronize two radars, and the oversimplified assumption of the nature of RBMs on otherwise stationary subjects. The investigation assumes they are linear movements large enough to cause target-bin migration and that they don't affect the phase information where the chest displacement data is embedded.

Some FMCW radar systems have focused more on improving the digital signal processing (DSP) techniques to eliminate the effect of RBMs. Some works have addressed this challenge using continuous wavelet transform (CWT), where the frequency of the wavelet coefficients is empirically decided [98]. Despite the cited investigation's success in decreasing the worst-case scenario error in HR detection by 10%, these systems require re-calibration for the selected CWT scales for different subjects, as they might vary based on the individual or the environment. This is evident by the variability of the error rate from below 5% to upwards of 15% for different test subjects. Other investigations address this issue by using CWT with adaptive scales [99, 100]. Despite their success at improving results, they present the challenge of significantly increasing the computation time, limiting their usability as a continuous monitoring system. Work by Cheng *et al.* uses a 24 GHz FMCW radar to compare the performance of different frequency decomposition modalities such as empirical mode decomposition (EMD), empirical wavelet transform (EWT), Hilbert vibration decomposition (HVD), and their proposed methodology of enhanced HVD [101]. The evaluated methods can remove both small and large scale RBMs with varying levels of success, achieving an HR error percentage of 46.22%, 2.75%, 2.61%, and 1.67% for the previously mentioned methods, respectively. However, the more accurate the results the slower the processing time is for the raw data, as the previously mentioned methods in the investigation achieve a time of 0.083 s, 0.0066 s, 0.663 s, and 0.883 s, respectively. Moreover, all methods described in this paragraph only extract cardio-respiratory rates

and do not provide additional information regarding the mechanics of the lung and heart by providing waveforms during respiration or the heartbeat, which can further limit the extraction of additional biometrics.

The second challenge experienced by FMCW systems is the extraction of cardiovascular rates and waveforms in the presence of multiple targets. This limitation has been mostly addressed by improving signal processing complexity and efficacy. For example, work by Lee *et al.* processes the signal from a 24 GHz using the multiple signal classification (MUSIC) algorithm to identify the position of different subjects in the radar FOV, with an additional FFT used in conjunction to a parametric spectral estimation technique to monitor VS for multiple subjects [102]. The investigation can monitor the cardio-respiratory signs of two targets 40 cm apart, which is beyond the limit of the theoretical range resolution of the system. Nevertheless, the computational overhead and cost of the MUSIC algorithm are high, which makes such a system potentially difficult to implement for continuous real-time vital-sign monitoring.

Multi-target VS detection using multiple input multiple output (MIMO) FMCW radars is an advanced technique that holds significant potential in healthcare applications. These radar systems utilize multiple transmitting and receiving antennas to obtain rich spatial and temporal information that can aid in the detection of multiple targets. The investigation by Dai *et al.* utilizes a 77 GHz FMCW system to track the cardio-respiratory rates for two seated subjects 0.6 m apart [15]. This is well within the capability of the range resolution of this system, as such, it is relatively straightforward to separate the two targets into two different range bins and monitor the RR of both subjects separately. This investigation shows a maximum root mean squared error (RMSE) of 2.3 for the detected RR when compared to a health monitoring belt. Nevertheless, the system does not attempt extracting HR or any other information about the cardio-respiratory waveforms. In addition, in both of these investigations, the subject remains still, which is unrealistic for a real-world detection system.

The successful implementation of FMCW radar systems for ambulatory subject monitoring is a critical challenge that encompasses elements of the two previously discussed obstacles. This challenge pertains to the presence of RBM in the radar signal and the potential existence of multiple targets in the radar FOV. Specifically, this challenge necessitates the development of a robust solution capable of accurately extracting cardio-respiratory rates even in scenarios where the monitored subject is in motion or engaged in physical exercise. Overcoming this limitation is vital for the widespread adoption of FMCW radar systems for health monitoring as it enables continuous and reliable VS monitoring in dynamic and active settings. Work by Mercuri et al. explores the use of an 8 GHz radar for contactless monitoring of multiple non-stationary targets [13]. The investigation differenti-

ates between up to three moving targets with 97.77% accuracy, however, it does not extract the cardio-respiratory rates of the ambulatory target. Instead, the investigation explores the accuracy of cardio-respiratory rate detection with the addition of "moderate RBMs". The participants in the study were instructed to perform up to five moderate RBMs (i.e., moderate limb movements, crossing the legs, and so on) for a single measurement, which results in a RR and HR accuracy of 75.63% and 59.25%, respectively.

There have been investigations using CW implementations of ambulatory cardio-respiratory rate detection. An investigation by Morgan and Zierdt uses a radar with a bandwidth between 1–10GHz for RR and HR detection during two types of regulated motions: Periodic steps forwards and backward in a 2-meter range, and a 4-meter walk at the speed of 0.3 m/s [103]. With an ambulatory subject, the large body motion overwhelms the small respiration and heartbeat signals, making reliable estimation of rates very difficult as the paper concludes that no clear cardio-respiratory waveform or rate can be reliably extracted under those conditions. An investigation by Mikhelson *et al.* uses a 94-GHz mm-Wave interferometer to detect chest displacements due to breathing and heartbeat [93]. The investigation evaluates the proposed system using a protocol where the subject begins seated, stands up and walks slowly towards the sensor, walks back, and then runs towards the sensor. A combination of statistical methods and prior knowledge about the nature of the human heartbeat (e.g., $max\ HR = 200 - age$) are employed to create a probability distribution to classify a detected peak in the radar cardiac displacement waveform as a "heartbeat". Although the investigation shows a recall of over 88% and precision of over 85%, the values show a high variance for different test subjects due to the subjective nature of the employed statistical methods. Moreover, the suggested technique requires the calculation of the classification probability distributions for each subject, as well as prior knowledge about their age and demographic, making the system computationally expensive and hard to implement in real-time for most users, especially those with abnormal HR.

The final challenge particularly concerns the proper extraction of cardiovascular data using FMCW radar systems. The HR typically occurs between 1–3 Hz (i.e., 60-90 beats per minute) and RR occurs at 0.1–0.5 Hz (i.e., 6–30 breaths per minute), as such, the fourth or fifth harmonic of the breathing signal overlaps with the cardiac signal [16]. Keeping in mind that the chest vibrations due to the heartbeat have a much smaller amplitude than those due to breathing, the extraction of a detailed cardiac waveform can be a challenge. Alizadeh *et al.* use a 77 GHz FMCW radar for their investigation and employ the common approach of applying a discrete-time Fourier Transform (DFT) to determine the target range, and extracting the semi-periodic chest vibrations by applying a second DFT across the collected frames [14]. A bandpass filter (BPF) with appropriate upper and lower cutoff

values is applied to retrieve the HR and RR. The investigation explains the use of a mm-Wave system due to its high sensitivity to small cardiac and respiratory chest vibrations and can achieve a Pearson correlation coefficient of 0.9 when tracking the RR and 0.8 when tracking the HR when compared to a health monitoring vest, indicating very close tracking. additionally, an investigation by Arsalan *et al.* uses Kalman filtering to improve the continuous HR estimation, and can reduce the RMSE in the detected HR from 17.6 to 5.3 [104]. Other modal decomposition methods have also been used for this purpose but can add complexity which limits the real-time continuous application of the system, as is the case in the previously mentioned investigation by Cheng *et al.* [101].

Near field radar-based monitoring

With the previously mentioned obstacles facing far-field radar-based VS detection, near-field-based methods, where the radar is placed on the body, are proposed as a method of reducing environmental noise, multi-target challenges, and RBM effects on the quality of the detected signal in contactless radar systems. Moreover, wearable radar methods still maintain an advantage over conventional cardio-respiratory detection methods, as they do not need to be in direct contact with the skin, can easily account for motion artifacts though DSP, and can perform both cardiac and respiratory monitoring through one device. An investigation by Bi *et al.* uses a single radar unit operating at 2.4 GHz (that was chosen "arbitrarily") for near-field detection of cardiac displacement and HR. The cited work qualitatively highlights the system sensitivity to the placement location and antenna polarization on the chest to proper cardiovascular signal detection [105]. Although the system maps extracted results to a simultaneously recorded ECG signal, the investigation simply shows the variation in the raw in-phase and quadrature (IQ) data without further analysis of the features of the waveform or extraction of any biometrics such as HR. The investigation does not look further into extracting respiratory waveforms or their rate or investigating their effect on the retrieved cardiac waveforms. Moreover, the investigation is performed on the target in idealized stationary positions.

Work by Fletcher *et al.* uses a single 2.45 GHz CW near-field radar system operating at a distance of 1–2 cm from the torso [106]. The system is presented as a sensor that can be integrated into clothing and blankets. This radar produces ECG-like readings with a good signal to noise ratio (SNR), however, it provides no information about breathing rate or breathing waveform, which is a crucial aspect of VS characterization. The paper also only captures the results in a stationary supine setting, which is not realistic for real-world ambulatory applications. The system discusses the potential for real-time continuous monitoring by using periodic measurements to optimize power consumption.

Finally, work by Wang *et al.* describes a bistatic CW radar system made up of two main parts: a self-injection-locked oscillator (SILO) tag placed on the chest, and an injection-locked oscillator (ILO)-based frequency demodulator for signal processing within the operational frequency range of 2.36–2.484 GHz [107]. The SILO tag on the chest transmits a CW signal, that is reflected by a moving target (i.e., chest, lungs, or heart) and subsequently injected into the same oscillator. Chest movements due to either respiration or heartbeat have associated Doppler shifts which are extracted by frequency-demodulating the output signal of the oscillator using the ILO-based demodulator. This system is promising as a wearable as it was tested during various physical exercises such as running on a treadmill, and the tag consumes a low power of 4.4 mW, making it suitable for wearable architecture. Nevertheless, the bulky ILO-based frequency demodulator must be near the tag (located 30 cm from the subject in the investigation), which limits the portability of the device.

Chapter 3

Hardware Equipment & Experimental Setup

3.1 Ground truth

3.1.1 Frontier X activity monitor

The health monitoring belt utilized (Fourth Frontier, Frontier X) is a patented product that provides real-time feedback on cardiac and respiratory health meant for use during exercise [1]. This belt is designed to be worn around the torso, under the pectoralis muscle as shown in Figure 3.1, and was used in this thesis to establish a reference point for comparison with radar-collected data for RR. Values were compared with the ground truth rate set by a metronome, as will be discussed in upcoming subsections. Moreover, Frontier X was used to not only capture continuous ground truth HR and HRV data but ECG data as well for mapping against the radar cardiac displacement waveforms for correlation of cardiac events during the cardiac cycle. This ECG data is collected using a single-lead dry electrode, which although not as accurate as clinically prevalent methods, is still fairly accurate for use as a comparison method [108].

The Frontier X relays the collected biometrics to both a mobile and web application that can be used to view data analytics or download the raw data for plotting. The system calculates the heart rate by detecting the timing between ECG R-peaks in a ∼20-second window interval, while the root mean square of the successive differences (RMSSD) method

[1] This device was optimized for cardiac monitoring, although respiratory rate and strain are provided.

described in Figure 3.2 is used to calculate HRV. The method determines the time difference between successive heartbeat intervals (HBI), where N in the expression in the figure is the number of heartbeats in a given window [109]. To note, HRV refers to the variation in the time intervals between successive heartbeats and provides valuable insights into the autonomic nervous system's activity, which regulates the heartbeat [110]. The resulting RMSSD value represents the magnitude of short-term variability in HBI, with higher values indicating greater variability and stronger parasympathetic activity.



Figure 3.1: Frontier X health monitor by Fourth Frontier

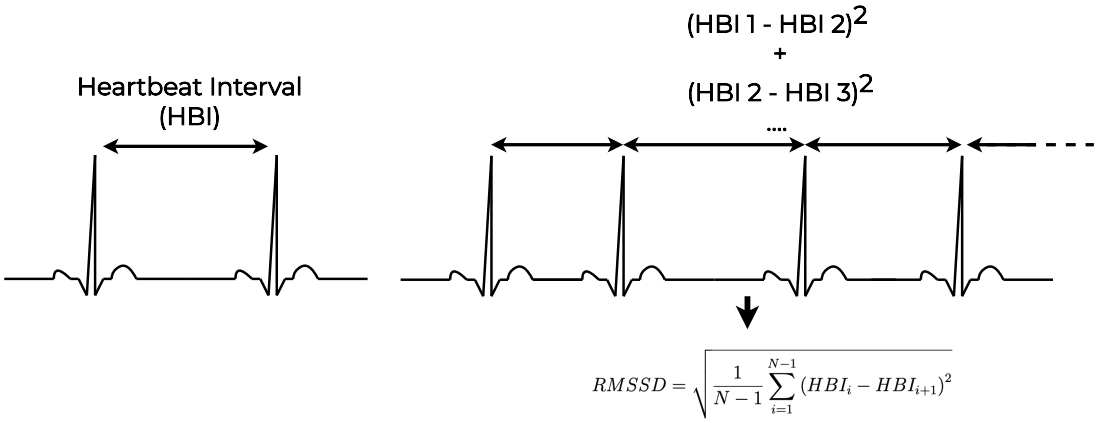


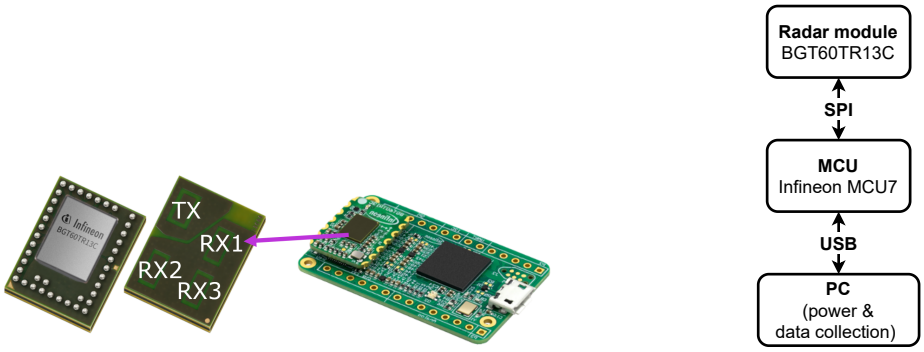
Figure 3.2: Visual representation of RMSSD calculation

3.1.2 Metronome usage

A metronome is a device that produces regular, rhythmic beats at a specific frequency, allowing individuals to synchronize their breathing with the audible rhythm. When it comes to monitoring and evaluating the RR, a metronome serves as a ground truth for the rate as it allows individuals to match their inhalations and exhalations to the beats, ensuring a controlled RR. The Frontier X does provide RR data, but as will become clear in upcoming chapters, it is of poor quality since the device is optimized for cardiac measurements. A metronome allows for accurate and reproducible measurements across different individuals and experimental conditions. Moreover, adjusting the metronome's frequency enables the control of the RR to match low values correlating with resting conditions, as well as higher values that correlate with physical activity. For this purpose, an online metronome was used and the sound was played over noise-cancelling headphones worn by the participants during data collection periods to help regulate their breathing [111].

3.2 60-GHz radar system hardware

The chosen FMCW radar system has multiple components including an RF front-end (containing a signal synthesizer, voltage-controlled oscillator (VCO), variable gain power amplifier (PA), antennas, variable gain low-noise amplifier (LNA), and mixer), an analog-to-digital converter (ADC), phase-locked loop (PLL), memory, and digital peripheral communication protocols. By using the 60 GHz Infineon radar module (Infineon, BGT60TR13C), a high level of integration combined into a single compact 6.5 mm $\times$ 5.0 mm chip solution can be achieved [112]. The system supports a wide 5.4 GHz bandwidth, which can improve detection accuracy as described in expression A.13, and has an optimized power consumption. The primary function of the radar module is to transmit a FMCW signal using its transmitter (TX) antenna, while simultaneously receiving echo signals from the target object using its three receiver (RX) 0.98 mm $\times$ 1.95 mm patch antennas shown in Figure 3.3a. Each receiver path includes base-band filtering, a variable-gain amplifier (VGA), and a 12-bit ADC. The digitized output is then stored in a first-in-first-out (FIFO) queue data structure. The data is then transferred to a microcontroller unit (MCU) on the Infineon demo-board (Infineon, DEMO BGT60TR13C) shown in Figure 3.3b for radar signal collection and pre-processing [113].



(a) 60 GHz radar module and data collection board highlighting three RX channels

(b) System diagram for the radar system

Figure 3.3: Summary of mm-Wave radar system used

3.2.1 Radar architecture

The Infineon radar utilizes a real modulation scheme as shown in Figure A.1a, with an additional PLL feedback control [112]. Below are a few distinctions between IQ and real mixing techniques:

- In IQ mixing, the signal power is distributed between I and Q, whereas real mixing does not involve any power division [114].
- In real mixing, the positive and negative frequencies are shifted to the left and right of DC, respectively. This conversion process results in the doubling of the noise level (i.e., +3.0 dB), and reducing the SNR at the baseband due to the overlapping noise from both positive and negative frequencies.
- As implied by the previous point, in IQ mixing, only the positive (or negative) portion of the spectrum is downconverted, making half the spectrum available for noise power estimations in the DSP of the baseband signal.

The frequency-modulated carrier signal has a linearly variable frequency in accordance with the baseband signal as shown in Figure A.1, making it robust against interference and noise. The architecture allows for precise recovery of the modulating signal at the receiver, as the synchronization ensures that the receiver knows the carrier's characteristics and can accurately extract the modulating information. However, any deviation in frequency or phase synchronization between the transmitter and receiver can lead to signal degradation

or loss of information; this radar module bypasses this limitation by utilizing an on-chip PLL system. The primary function of a PLL system is to track and synchronize the phase and frequency of an input reference signal (i.e., the VCO signal) with that of a local oscillator (i.e., the transmitted FMCW signal) [115]. A phase detector compares the phases of the reference and local oscillator signals and generates an error signal. This error signal is filtered and applied to the VCO, which adjusts its frequency based on the error signal. The feedback loop formed by the VCO, phase detector, and a lowpass filter (LPF) continuously adjusts the VCO frequency until the phase and frequency of the local oscillator closely match those of the reference signal. By controlling the frequency of the VCO, the PLL can achieve accurate frequency and phase synchronization, even in the presence of noise and frequency variations.

3.2.2 Full-wave electromagnetic radar simulations

The FMCW radar operates with a 60 GHz center frequency, which our group successfully utilized previously for near-field probing of human tissue, particularly, glucose level detection [116]. The module has a compact footprint of 6.5 mm $\times$ 5.0 mm placed on a 12.7 mm $\times$ 12 mm base PCB. The modules' three RXs, which were used for multi-channel data acquisition, are arranged in an L-shape for horizontal and vertical angular measurement as shown in Fig. 3.4. The full-wave electromagnetic simulator HFSS by Ansys was used for near-field operation analysis of the radar antennas [117]. The human torso was modeled as a volume with the dielectric properties of skin at 60 GHz as shown in Figure 3.4 [118]. The thickness of the volume was swept from 0.5λ to 2λ to ensure convergence to valid results using this model of the torso physiology.

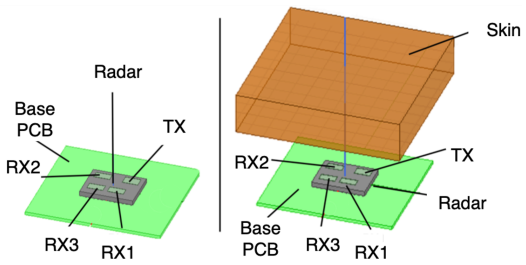
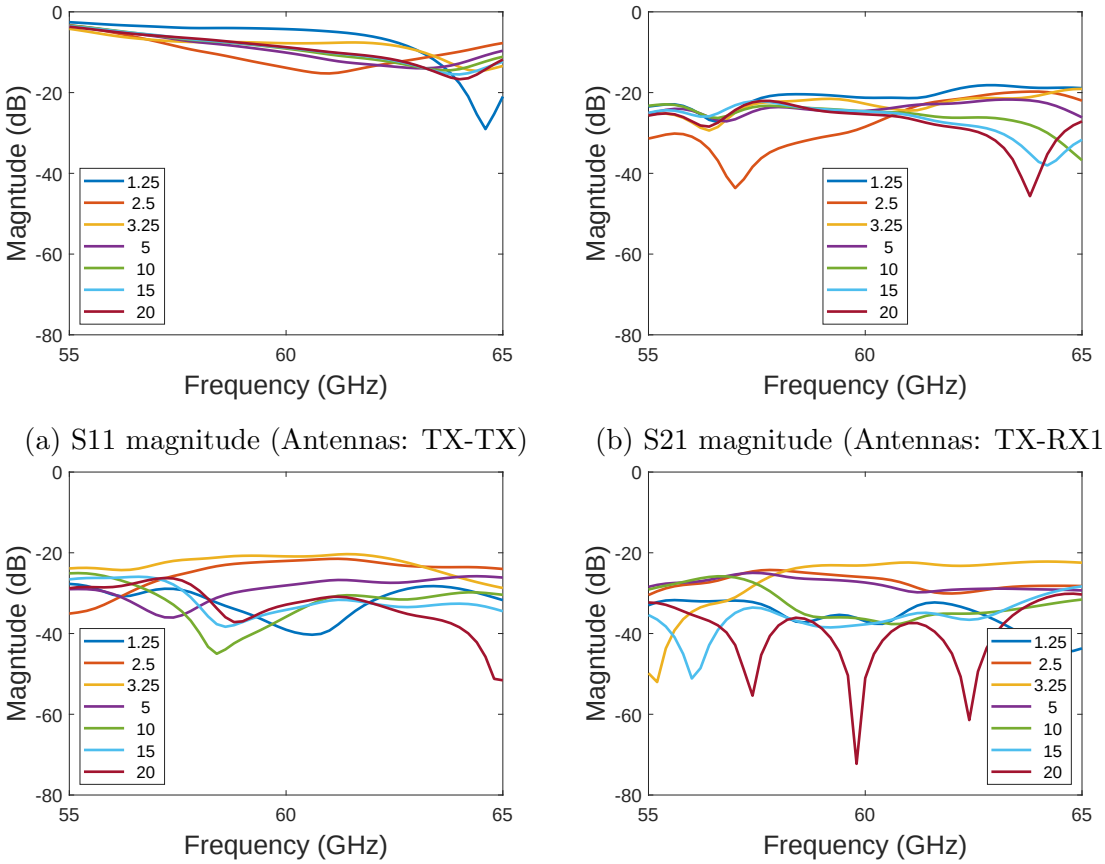


Figure 3.4: Simulated radar and base PCB with and without skin volume

The resulting S-parameter magnitudes and phases from a sweep of the distance between the radar antennas and the torso model are shown in Figure 3.5 and Figure 3.6, respectively.

The simulation type is a modal network, where each antenna is defined as a lumped port, and the entire structure is surrounded by an open boundary. The system operates on the torso *on top of clothing*, at it has negligible effects on the propagation. As can be seen from the S-parameter magnitudes in Figure 3.5, the loading effect of the torso model is clear on the antenna performance, in particular for near-field distances of < 5 mm. Nevertheless, coupling between the TX antenna and the three RX antenna is acceptable.



(a) S11 magnitude (Antennas: TX-TX)

(b) S21 magnitude (Antennas: TX-RX1)

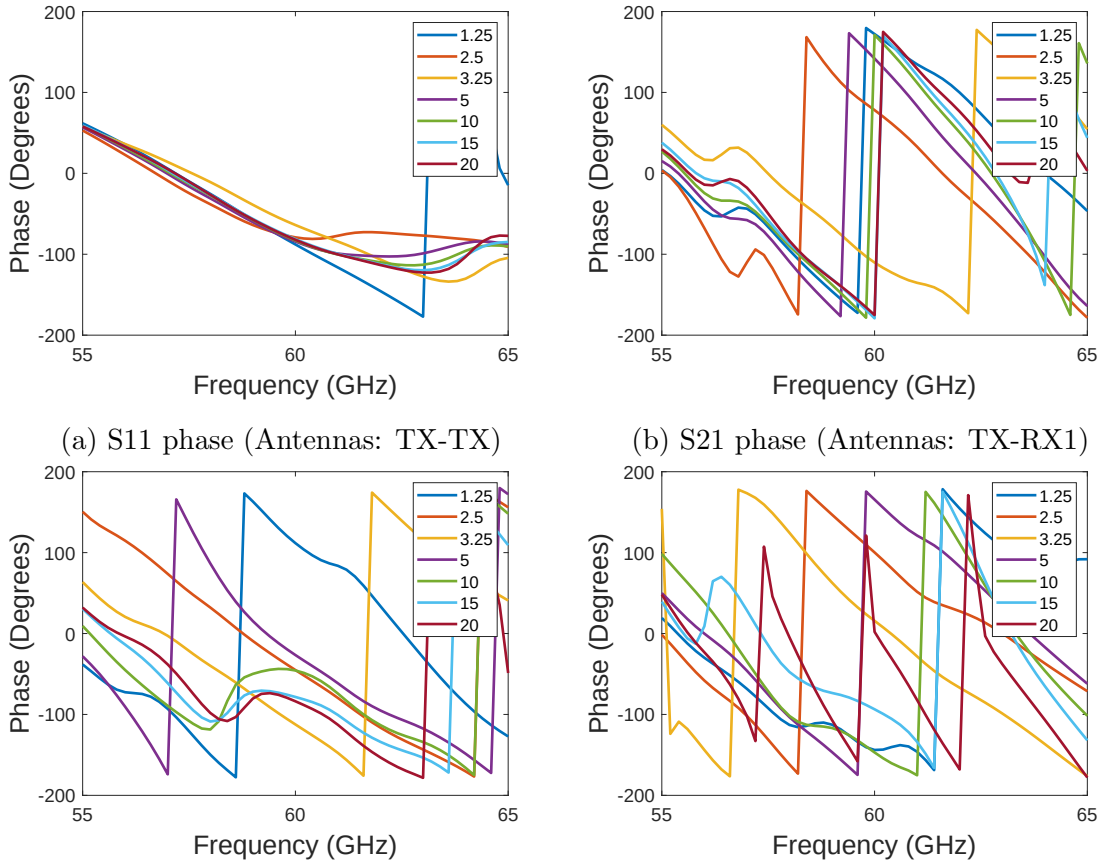
(c) S31 magnitude (Antennas: TX-RX2)

(d) S41 magnitude (Antennas: TX-RX3)

Figure 3.5: S-parameter magnitude for skin distance sweep a distance of 0.25λ (1.25 mm) to 4λ (20 mm) away from the skin

The S-parameter phases in Figure 3.6 show more variation with the sweep, with the transmission parameters being most affected in the relevant 5.4 GHz bandwidth around the center frequency of 60 GHz. Significant phase shifts appear, in particular for near-field

distances of < 5 mm resulting in significant signal lagging or leading. The practical effect of this is not significant for distances > 5 mm between the chest and the radar antennas. In addition, for some distances < 5 mm, a small group delay component is added, which occurs just outside the lower end of the bandwidth of interest. These combined phase effects can potentially affect the accuracy of the continuous phase extraction needed to detect vital signs using radars as described in Appendix A.1.



(a) S11 phase (Antennas: TX-TX)

(b) S21 phase (Antennas: TX-RX1)

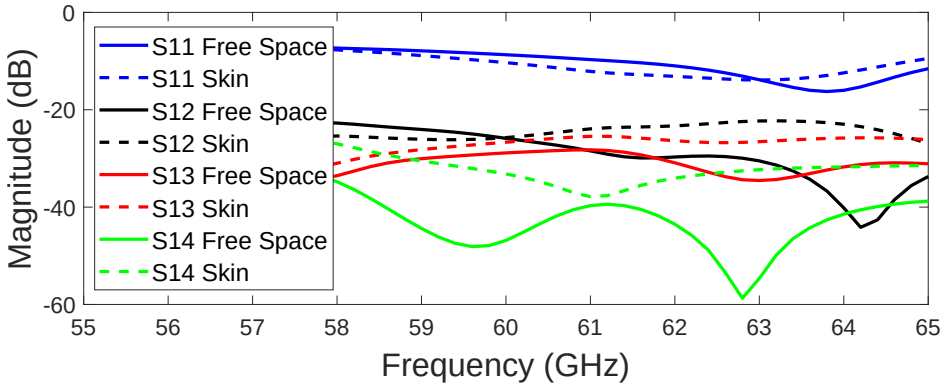
(c) S31 phase (Antennas: TX-RX2)

(d) S41 phase (Antennas: TX-RX3)

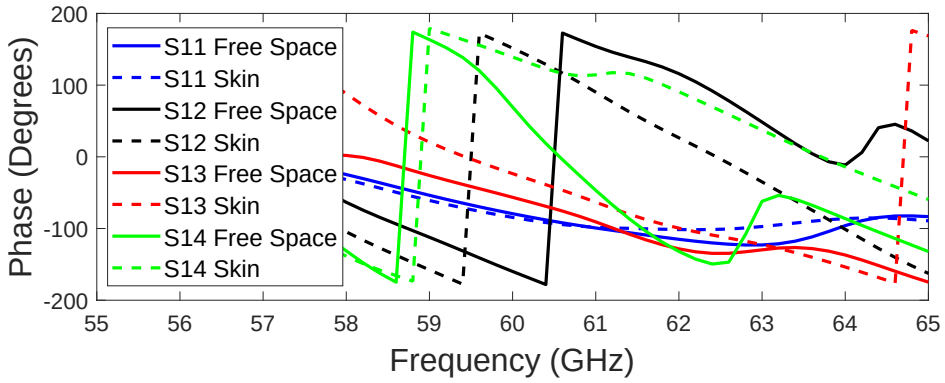
Figure 3.6: S-parameter phase for skin distance sweep a distance of 0.25λ (1.25 mm) to 4λ (20 mm) away from the skin

To summarize the results above, the same torso model shown in Figure 3.4 was simulated both without the skin and with the skin placed one wavelength away (i.e., $\lambda \approx 5$mm) from the radar. In Figure 3.7a, the magnitude s-parameter plot for the antennas of the

60 GHz mm-Wave radar shows minimal loading effects with a skin volume in the near-field. Although coupling between the single TX antenna and each of the RX antennas is impacted, it remains adequate for use in proximity to the skin. The phase plot shows minor shifts resulting in lagging or leading for different antennas, however, group delay is minimal and occurs outside the bandwidth of interest when present.



(a) Radar S-parameter magnitudes



(b) Relevant radar S-parameter phases

Figure 3.7: Radar antenna S-parameters in free space and with a skin volume 5 mm away

3.3 Data collection setup

The Infineon demo board containing the radar module, which integrates the RF frontend and provides sampled intermediate frequency (IF) signals, captures the radar samples for digital signal processing and enables configuration of the radar module. The board uses the USB interface to communicate with the PC for power and data acquisition. The radar module is positioned on top of clothing on the torso, and the Frontier X is worn under the clothing, in contact with the skin on the upper abdomen, for establishing cardiac ground truth, as shown in Figure 3.8. The metronome was played to the participant on noise-cancelling headphones. The radar parameters throughout this investigation were selected as specified in Table 3.1. The radar module used and the Frontier X both produce a time stamp that can be used to synchronize the cardio-respiratory signals provided by the devices. Throughout the thesis, accuracy values will be discussed, which were calculated according to 3.1. The ground truth values are biometrics provided by the Frontier X in the case of the HR and HRV comparison or the value of the metronome used to regulate participant breathing in the case of the RR comparison.

$$\%\ Accuracy = \left(1 - \frac{|value_{radar} - value_{ground\ truth}|}{value_{ground\ truth}}\right) \times 100 \tag{3.1}$$

For all experiments in Chapter 4 performed on human subjects, healthy participants ages 18–38 were recruited from the Wireless Sensors and Devices Lab. Approval of all ethical and experimental procedures and protocols was granted by the University of Waterloo, under Application No. 22770.

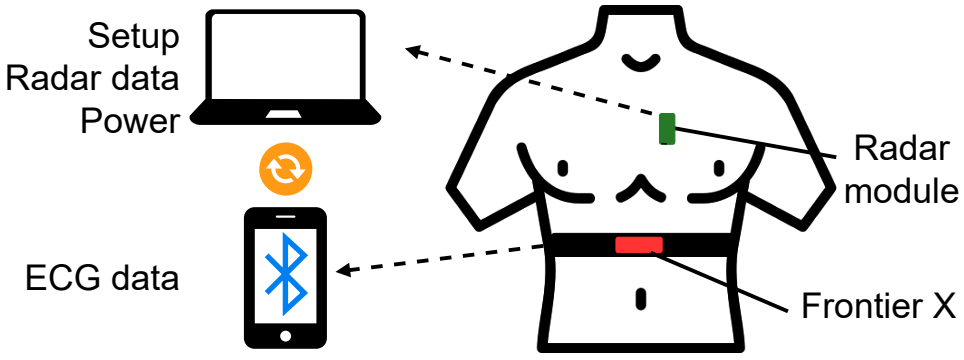


Figure 3.8: Experimental setup of 60 GHz radar and Frontier X on the torso for time synchronized data collection

Table 3.1: Radar parameters used for system

Parameter	**Value**
Bandwidth (GHz)	5.4
Center Frequency (GHz)	60
Sample Rate (MHz)	1.0
Chirp Duration (μs)	69
Pulse Repetition Time (μs)	504
Frame Rate (Hz)	20
Number of Chirps per Frame	32
Number of Samples per Chirp	64
Range Resolutions (m)	0.03
Maximum range (m)	0.96

Chapter 4

FMCW Radar for Cardio-respiratory Waveform and Rate Extraction

Work in this chapter was reported in the following publications:

- S. Abu-Sardanah, A. Gharamohammadi, O. M. Ramahi and G. Shaker, "A Wearable mm-Wave Radar Platform for Cardiorespiratory Monitoring," in IEEE Sensors Letters, vol. 7, no. 6, pp. 1-4, June 2023, Art no. 6003404, doi: 10.1109/LSENS.2023.3277365. [**Published**].
- S. Abu-Sardanah, O. M. Ramahi and G. Shaker, "A Wearable mmWave Radar System for Continuous Cardiopulmonary Monitoring," AP-S/USRI 2023 International Symposium 2023, Portland, Oregon. [**Completed, unpublished**].
- S. Abu-Sardanah, Y. Wang, A. Gharamohammadi, O. M. Ramahi and G. Shaker, "A Wearable mmWave Radar System for Respiratory Health Monitoring," Journal TBD. [**Under preparation**].

4.1 Digital signal processing chain

FMCW basics and derivations for expressions used in this chapter can be found in Appendix A.1. The signal processing chain for extracting the cardio-respiratory waveforms and their rates has two main components as highlighted in Figure 4.1:

- Determining the target (i.e., chest) range bin;
- Extracting the cardio-respiratory waveforms.

The down-converted raw radar data is sampled using a 12-bit ADC at $f_S = 1$ MHz, as described in Table 3.1. The down-converted raw radar signal, $x_{beat}(t_f,t_s)$ decribed in A.11, with a radial beat frequency ω_{beat} is acquired from each of the three RX ADC channels. In this expression, t_f is the fast time and t_s is the slow time. The sampled data is organized into a cube referred to from this point onward as the "radar data cube" as shown in Figure 4.2. The radar cube is a data structure with dimensions $M \times N \times K$, where M, N, and K [1] are the number of chirps, samples, and frames, respectively. For the remainder of this section, different operations will be applied to different dimensions of this cube, which will be referred to using the appropriate index reference.

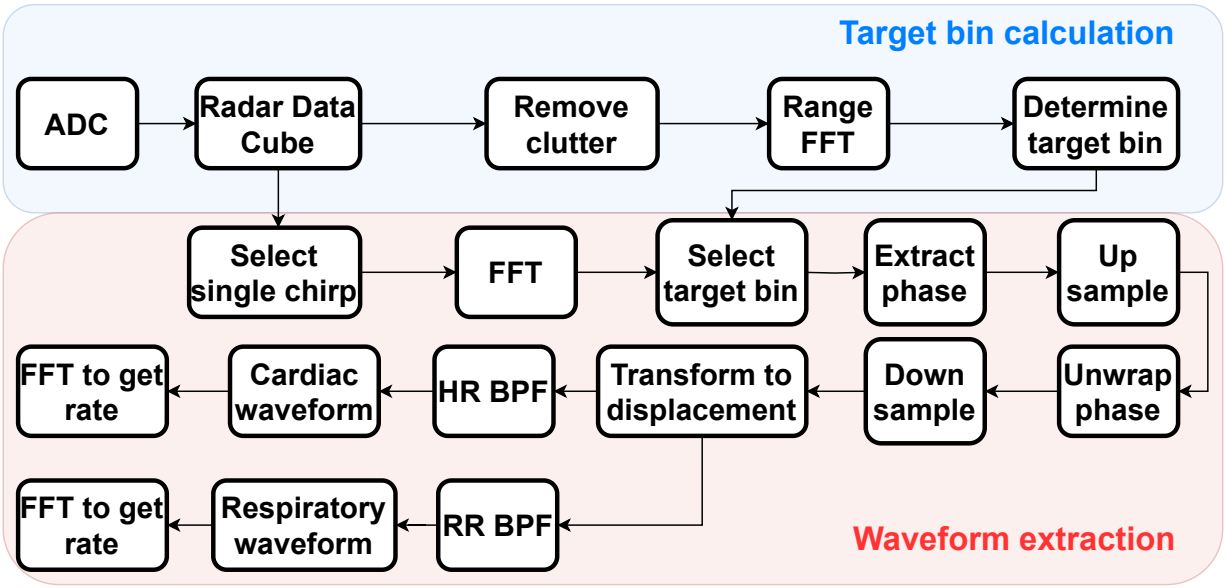


Figure 4.1: Digital signal processing chain for cardio-respiratory waveform and rate extraction

[1] Here, K denotes the number of frames is not to be confused with the K in Chapter A.1 indicating the chirp slope

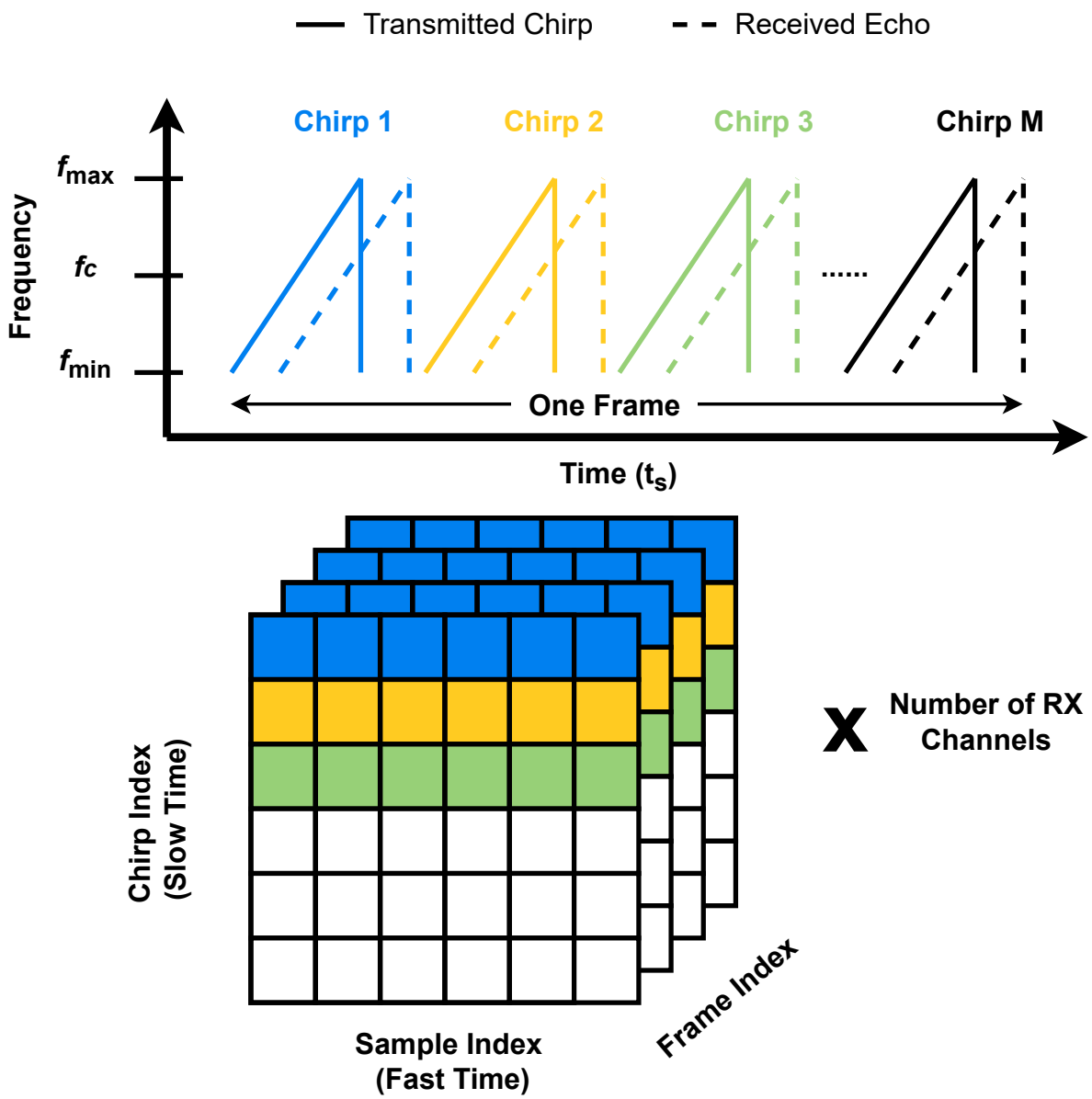


Figure 4.2: Radar data cube highlighting matrix dimensions

4.1.1 Determining the target range

Clutter removal

To determine the target range, which is the chest of the test subject, unwanted extraneous echos —referred to as clutter— must first be removed from the raw signal. Clutter can affect the acquired signal quality which interferes with the accurate detection of cardio-respiratory rates if not handled properly, as the extraction can performed on the incorrect range bin. In VS monitoring applications, radar clutter can originate from various sources, which can manifest in the form of:

1. **Static clutter**: This type of clutter is caused by stationary objects in the environment, such as walls, furniture, or other objects that reflect radar signals in the case of contactless radars. For a wearable radar system, stationary clutter can be reflections from loose clothing. These stationary objects can create echoes that interfere with the detection of the target range bin, which affects the accuracy of extracted VS.

2. **Dynamic clutter**: Dynamic clutter refers to moving objects within the radar's field of view that reflect the radar signals. Examples include people or objects moving in the background or nearby, such as medical equipment, fans, or curtains. These effects are minimal in a wearable radar system, as the FOV is limited to the test subject's chest. Nevertheless, they can appear as moving clothing or jewelry, especially during ambulatory measurements. The movement of these objects can also interfere with the detection of the target range bin, which affects the extracted VS.

3. **Multi-path reflections**: Radar signals can bounce off of multiple surfaces before reaching the receiver. When these reflected signals arrive at the receiver at different times, they can interfere with each other and create interference patterns, leading to clutter. Multi-path reflections can occur due to reflections from walls, floors, or other objects in the environment in contactless radar systems. In the case of a wearable radar system, these reflections can result from signal reflections from different parts of the torso.

At the clutter removal stage, the mean of the raw signal across K frames is determined and subtracted from all $M \times N \times K$ sample points in the cube. We can showcase this by first discretizing the downconverted radar signal $x_{beat}(t_f,t_s)$ in A.11, and expressing it as in 4.1 and 4.2 where A_{TX} is the transmitted signal amplitude, A_{RX} is the amplitude of the signal received echo, R_0 is the distance to the target's chest, $\Delta d[m]$ is the chest vibration

due to respiration and heartbeat, λ_{max} is the longest wavelength in the band (associated with f_{min}), f_{beat} is the frequency of the beat signal, and ϕ_T is the total accumulated phase noise of the RF frontend. Note that the chest vibration due to cardio-repiratory activity is embedded in the phase expression in 4.2. The signal is sampled at $f_S = 1$ MHz in the fast time across the N-length dimension, therefore, the fast time discretized intervals can be expressed as $t_f = n/f_S$. The signal is sampled at $f_C = 1/T_C$ in the slow time across the M-length dimension, therefore, the slow time discretized intervals can be expressed as $t_s = m/f_C$. In these expressions, n and m are discrete fast and slow time indices in $[0, N-1]$ and $[0, M-1]$, respectively. This procedure is repeated across successive frames. This limits the investigation to an $M \times N \times W$ cube where W is a sliding window with overlap and of some defined length with a max value equal to the number of frames, K.

$$x_{beat}[n,m] = A_{TX}A_{RX}\cos\left[4\pi\frac{R_0}{\lambda_{max}} + 4\pi\frac{\Delta d[m]}{\lambda_{max}} + 2\pi n f_{beat} + \phi_T[n,m]\right] \tag{4.1}$$

$$\theta_{beat}[n,m] = 4\pi\frac{R_0}{\lambda_{max}} + 4\pi\frac{\Delta d[m]}{\lambda_{max}} + 2\pi n f_{beat} + \phi_T[n,m] \tag{4.2}$$

After clutter removal across multiple frames the signal $x_{beat}[n,m]$ becomes $y[n,m]$:

$$y[n,m] = x_{beat}[n,m] - \frac{1}{W}\sum_{w=0}^{W-1} x_{beat}[n,m]_w \tag{4.3}$$

Target range detection

The distance to the chest of the test subject, R_0, in each of the K frames can be determined by applying the FFT $Y = \mathcal{F}\{y\}$ along the fast time axis. Applying the FFT across the N samples for each of the M chirps as shown in Figure 4.3a (i.e., across each of the rows in the radar data cube) obtains the spectrum of the beat signal. The complex-valued spectrum, as described in 4.4, where p is the frequency domain index within $\left[0, \frac{N}{2}+1\right]$ and n is the time domain index within $\left[\frac{-N}{2}, \frac{N}{2}+1\right]$, will have a maximum magnitude occurring at a frequency specifying the position of the detected target as seen in Figure 4.3b. This FFT reveals target range information, as such, it is often referred to as a range FFT. Each frequency bin in the resulting spectrum can be expressed as a distance at increments of the range resolution as specified in A.13. This procedure is repeated across successive frames using a sliding overlapping window W with a max value equal to the number of frames, K.

$$Y_p[\omega_n] = \sum_{n=0}^{N-1} y[n] \cdot {W_n}^{np}, \quad \text{where } W_n = \exp\left(\frac{-2\pi j}{N}\right) \text{ is one of } n \text{ roots of unity}$$

$$Y_p[\omega_n] = \sum_{n=0}^{N-1} y[n] \cdot \exp\left(\frac{-2\pi j}{N} np\right) \tag{4.4}$$

Since the radar signal is real-valued, the resulting spectrum is conjugate symmetric (i.e., $|Y[-\omega]| = |Y[\omega]|$ and $\angle Y[-\omega] = -Y[\omega]$), therefore the signal is sufficiently described by considering the spectrum in the range $\left[0, \frac{N}{2} + 1\right]$. The result of the FFT is a complex sequence of values as described in 4.4 with magnitude and phase as described in 4.5 and 4.6, respectively. The radial frequency indices of the spectrum, $\omega = 2\pi f$, are described in 4.7, since the sampling frequency is the limiting factor for the detectable beat frequency (see A.14). The magnitude spectrum of the signal can be determined by applying 4.5 to all points in $\left[0, \frac{N}{2} + 1\right]$, where the target bin with the maximum amplitude, $argmax(|Y_p[\omega_n]|)$, indicates the chest range bin as shown in Figure 4.3.

$$|Y_p[\omega_n]| = \sqrt{\mathfrak{Re}(Y_p[\omega_n])^2 + \mathfrak{Im}(Y_p[\omega_n])^2} \tag{4.5}$$

$$\theta_{Y_p} = \tan^{-1}\left(\frac{\mathfrak{Im}(Y_p[\omega_n])}{\mathfrak{Re}(Y_p[\omega_n])}\right) \tag{4.6}$$

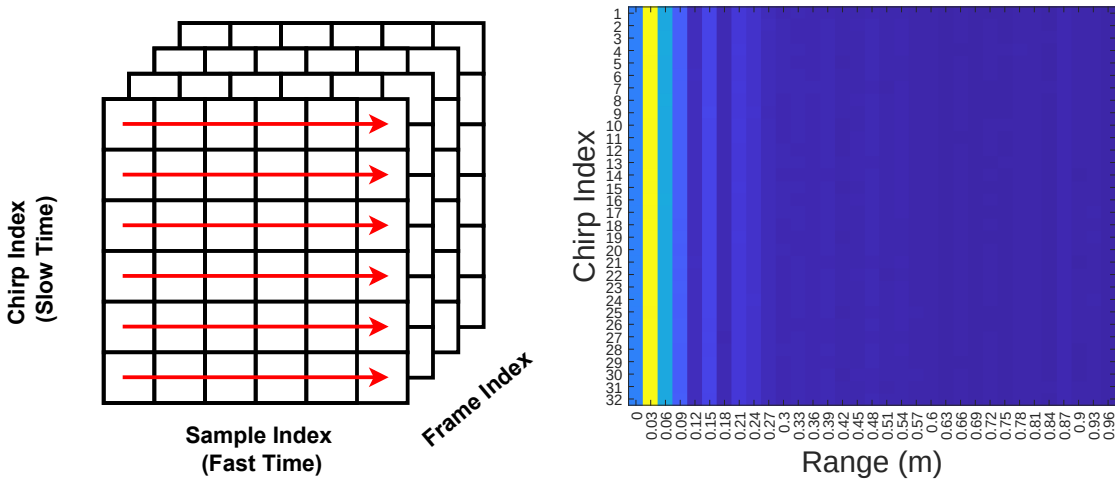
$$\omega_n = n \times \frac{f_S}{N} \tag{4.7}$$

Considering these expressions, and keeping the Nyquist sampling theorem in mind, it can be observed that to detect a target at a range resulting in a given f_{beat}, said frequency must meet the condition: $f_{beat} \leq f_{beat_{max}} = f_S/2$. Considering the round-trip time for signal propagation $\tau = 2R_{0_{max}}/c$, and the chirp slope K, resulting in $f_{beat} = \tau \cdot K$ (see Figure A.1b) we determine the maximum detectable target range as $R_{0_{max}} = f_S \cdot c/(2K)$, as described in A.14. Likewise, the minimum resolvable beat frequency can be described as f_S/N according to 4.7, which can be defined in terms of the minimum detectable range as in the following expression: $R_{0_{min}} = f_S/N \cdot c/(2K) = c/(2B)$, as shown in A.13 as well.

4.1.2 Extracting cardio-respiratory signals

Target range selection

Now that the position of the target's chest, R_0, is determined, it is possible to extract the vibrations due to the VS described as $\Delta d[m]$ around R_0 in 4.2 and A.9. It it worthy of note



(a) Range FFT operation on relevant radar cube dimension

(b) Target position at 0.03 m shown in one of K frames

Figure 4.3: Sample target detection visual summary

that the small wavelength for the utilized mm-Wave radar lends itself to high sensitivity to the small vibrations of the chest. Since the methodology utilized in this investigation is based solely on displacement (not velocity or Doppler information), a single chirp is considered for all collected frames, which eliminates the need to consider the M-length slow time dimension in upcoming steps. Moreover, the difference in the signal from chirp to chirp was observed to be minor in comparison to the frame-to-frame variation. This simplification reduces the size of the radar cube to an $N \times K$ matrix if all frames are processed at once. The sampling period of interest for observing phase modulation due to the vibration of the chest as result of cardio-respiratory activity is, therefore, along the K-length dimension of the radar cube in increments of T_R. To create a continuous real-time estimate of the cardio-respiratory displacements and rates in time, one can take a sliding window of some defined length, W, along the K-length dimension across the frames (period of T_R) with some overlap, simplifying each iteration to an $N \times W$ matrix.

An FFT is applied across the N-length dimension of the *cluttered* x_{beat} signal (i.e., along the fast time as shown in Figure 4.3a), producing a rich complex-valued spectrum, where only the values in the range $\left[0, \frac{N}{2} + 1\right]$ are considered due to the conjugate symmetry of real-values raw data. The previously determined chest range bin (in Figure 4.3b), is tracked across successive frames. This limits the investigation to a $1 \times W$ array, where W is the aforementioned sliding window of some defined length.

Phase extraction

The expression for the phase associated with the cardio-respiratory signal within one frame is given in 4.2, noticeably, the vibration $\Delta d[m]$ varies along the slow time in this expression. Our method depends on tracking the vibration across successive frames using only one chirp (i.e., one point in the slow time) which extracts a signal with a frequency corresponding to the RR and HR. The envelope of this signal (which is described by θ_1 in A.9 corresponds to the cardio-respiratory displacement of the chest.

An expression can be used to simplify the signal, assuming that the chest appears to be stationary to the wearable radar, as the cardio-respiratory displacements are too small to be detected as range-bin variations. Therefore, the signal in a k-index frame, sampled at a rate of $f_R = 1/T_R$ can be represented as a combination of the breathing signal with amplitude A_B and frequency f_B, the heart signal with amplitude A_H and frequency f_H, and the total phase noise as described in 4.8. Extracting the envelope enables the tracking of the chest displacement due to the heartbeat and respiration, and extracting the frequency components enables the extraction of the cardio-respiratory rates. Of course, this expression is an oversimplification of the spectrum, which will be rich with many peaks at RR and HR harmonics, as well as their inter-modulation (IMD) products.

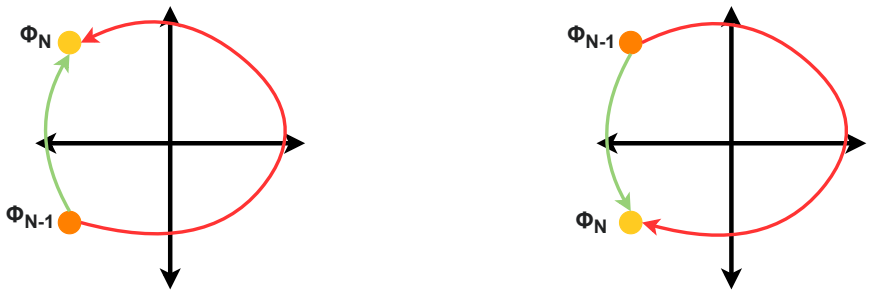
$$\Delta d[k] = \frac{4\pi}{\lambda_{max}} A_B \cos\left(2\pi \frac{f_B}{f_R} k\right) + \frac{4\pi}{\lambda_{max}} A_H \cos\left(2\pi \frac{f_H}{f_R} k\right) + \phi_T[k] \tag{4.8}$$

The arctangent demodulation (AD) technique was chosen as the phase analysis method of choice due to its relative insensitivity to local oscillator (LO) and mixer phase noise and its high sensitivity to small changes in displacement as shown in Appendix A.2 [16]. This method extracts the phase at the target range bin from the complex-valued FFT result according to the expression in 4.6. Nevertheless, the $\tan^{-1}$ function produces outputs in the range $[\frac{-\pi}{2}, \frac{\pi}{2}]$, thus, two consecutive angle measurements could vary within $[-\pi, \pi]$. If this range is exceeded, the phase measurement will wrap around and introduce a sudden discontinuity. Phase unwrapping aims to remove these discontinuities and provide a continuous and accurate representation of the phase. It involves identifying the phase jumps or "wraps" and adding appropriate multiples of 2π to the phase values to ensure a smooth and unwrapped phase curve. Detection of discontinuities requires knowledge of two successive phase values at a time, denoted by: ϕ_N and ϕ_{N-1} [2]. A discontinuity occurs when $|\phi_N - \phi_{N-1}| > \pi$, which must be corrected to reveal the true phase value and remove any discontinuities as described below and demonstrated in algorithm 1:

[2]Note that this use of the subscript N is *unrelated* to the previous uses denoting the number of samples in a chirp

- $\phi_N - \phi_{N-1} > \pi$: Should indicate a clockwise jump across one quadrant, instead it is interpreted as a counter-clockwise jump across three quadrants without phase unwrapping due to the constraints of the range $[-\pi, \pi]$ as shown in Figure 4.4a. In this case, multiples of 2π must be subtracted from ϕ_N.

- ϕ_N - $\phi_{N-1} < -\pi$: Should indicate a counter-clockwise jump across one quadrant, instead it is interpreted as a clockwise jump across three quadrants without phase unwrapping due to the constraints of the range $[-\pi, \pi]$ as shown in Figure 4.4b. In this case, multiples of 2π must be added to ϕ_N.



(a) Phase discontinuity greater than π (b) Phase discontinuity smaller than $-\pi$

Figure 4.4: Example of phase discontinuities that must be addressed through phase unwrapping where the green path is the correct transition and the red path is the transition before phase unwrapping

Up-sampling is typically employed before phase unwrapping in scenarios where the phase discontinuities are closely spaced, and the phase variations are small between adjacent samples. By increasing the sampling rate, up-sampling helps to capture finer details in the phase signal as shown in the example in Figure 4.5 and improves the accuracy of the unwrapping process in algorithm 1. Two main scenarios may benefit from up-sampling the data before unwrapping:

- High wrap density: When the phase wraps occur at a high density within a short interval, up-sampling can help resolve the phase ambiguities and provide a more accurate representation of the phase. By increasing the number of samples per wrap, up-sampling allows for better detection and unwrapping of phase jumps.

- Small phase variations: In cases where the phase variations between adjacent samples are small, up-sampling can enhance the resolution of the phase signal. This

is particularly important when dealing with subtle phase changes or precise phase tracking. Up-sampling increases the number of samples and improves the ability to detect and unwrap fine phase variations.

Algorithm 1 Phase unwrapping with up-sampling and down-sampling

Require: Phase sequence with phase wraps, $\phi[n]$
Ensure: Unwrapped phase sequence, $\Phi[n]$
1: Up-sample $\phi[n]$ with interpolation to obtain $\tilde{\phi}[n]$
2: Initialize $\Phi[0] = \tilde{\phi}[0]$
3: **for** $n = 1$ to $N - 1$ **do**
4: $\quad \Delta\tilde{\phi} = \tilde{\phi}[n] - \tilde{\phi}[n-1]$
5: $\quad$ **if** $\Delta\tilde{\phi} > \pi$ **then**
6: $\quad\quad \Phi[n] = \Phi[n-1] - 2\pi$
7: $\quad$ **else if** $\Delta\tilde{\phi} < -\pi$ **then**
8: $\quad\quad \Phi[n] = \Phi[n-1] + 2\pi$
9: $\quad$ **else**
10: $\quad\quad \Phi[n] = \tilde{\phi}[n]$
11: $\quad$ **end if**
12: **end for**
13: Down-sample $\Phi[n]$ with anti-aliasing LPF to obtain the final unwrapped phase sequence

It is crucial to maintain the phase information quality and to avoid artifacts introduced by the sampling rate conversion process. Up-sampling must be performed with interpolation techniques to estimate and insert additional samples by using mathematical functions to generate the intermediate data points. The purpose of interpolation is to preserve the signal's characteristics and capture the finer details introduced by the increased sampling rate. The MATLAB function `interp()` was used to double the sampling rate, which uses the lowpass interpolation algorithm 8.1 in [119]. Likewise, down-sampling without proper filtering can introduce aliasing, which is the distortion of the signal due to overlapping frequency components. To prevent aliasing, it is necessary to apply an anti-aliasing LPF before down-sampling to attenuate the high-frequency components in the signal. The filter ensures that the frequency content of the signal is limited to below the Nyquist frequency to avoid overlap and distortion. The MATLAB function `resample()`, which implements an finite-element response (FIR) anti-aliasing LPF, was used.

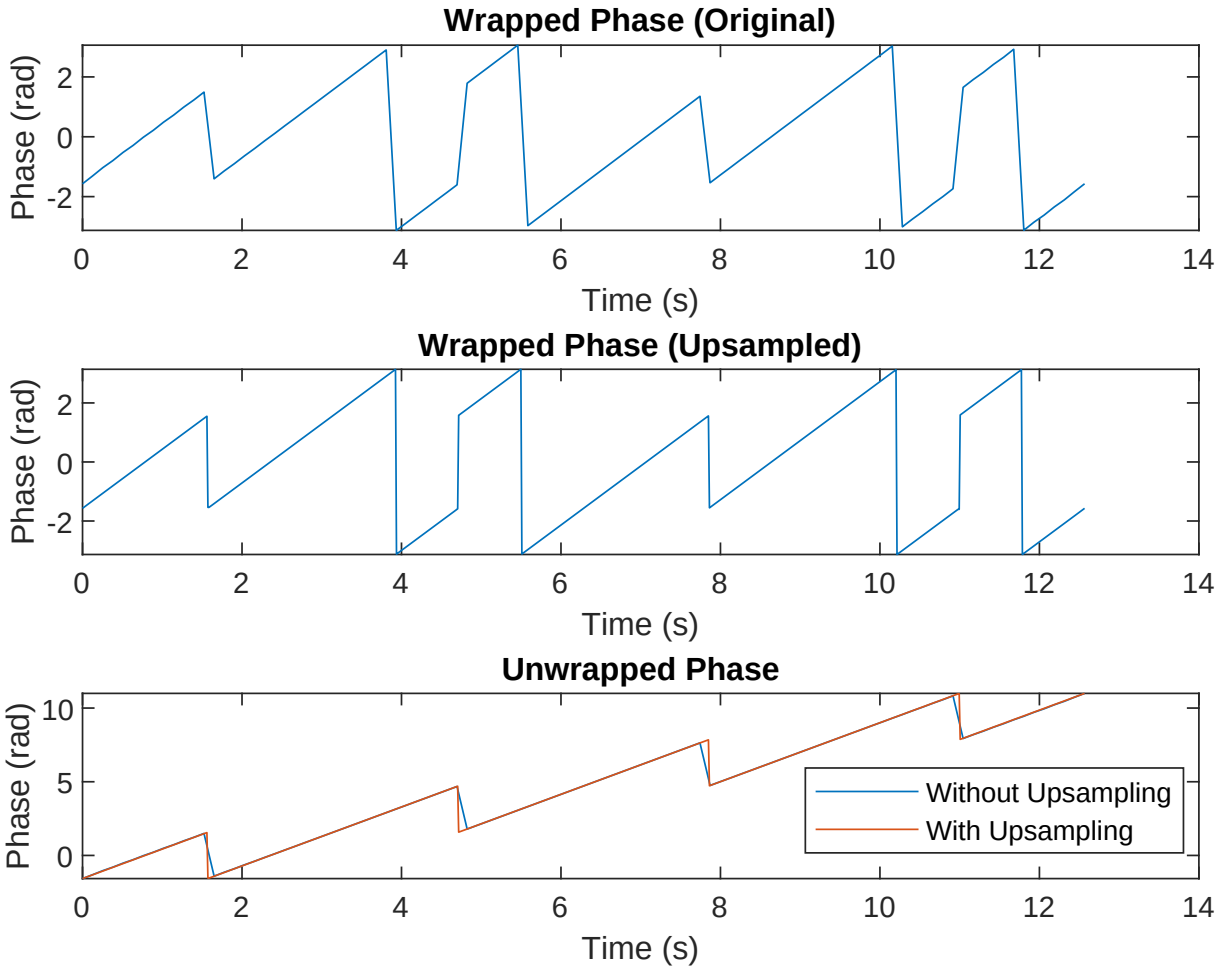


Figure 4.5: Example of phase unwrapping with and without up-sampling. Note the sharp transition that can be captured when up-sampling the data

Rate extraction

This waveform for $\Delta d[k]$ contains displacements due to both respiration and heartbeat as described in 4.8. Recall that the HR typically occurs between 1–3 Hz (i.e., 60–90 beats per minute) and RR occurs at 0.1–0.5 Hz (i.e., 6–30 breaths per minute) [16]. Therefore, appropriate Butterworth FIR BPFs are used to separate the respiratory and cardiac waveforms from the rich unfiltered spectrum shown in Figure 4.6. Keeping in mind that the amplitude of the cardiac displacement is much smaller than the amplitude due to the breathing displacement, the extraction of a detailed cardiac waveform can be a challenge due to the potential overlap of high-order respiratory harmonics with the cardiac displacement waveform.

To extract the cardio-respiratory rates from the filtered chest displacement waveforms following the application of the proper filter, an FFT must be applied along the successive W-length displacement array windows. The frequency bin with the maximum amplitude indicates the appropriate rate in Hz, creating a continuous curve with time that tracks the biometrics of interest. Note that by the Nyquist sampling theorem, the largest detectable frequency for this FFT would be $f_R/2$, which corresponds to 10 Hz considering the frame rate in Table 3.1. This is more than sufficient for capturing the RR and HR.

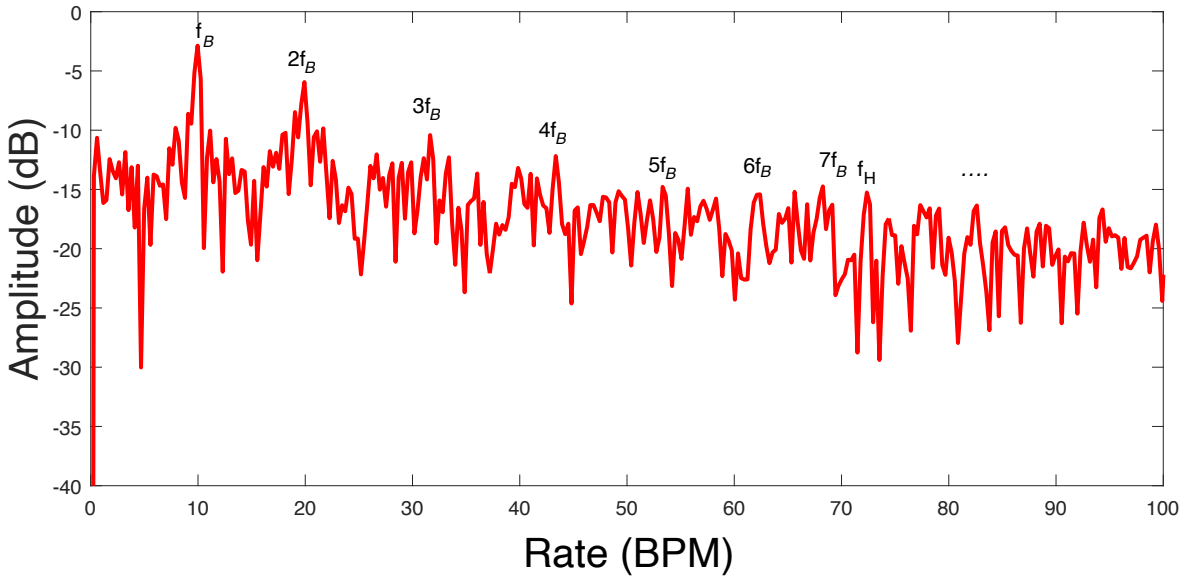


Figure 4.6: Sample spectrum highlighting different frequency components during VS extraction with RR of 10 breaths/minute, and HR of 72 beats/minute

4.2 Cardiac investigation

4.2.1 Extraction of cardiac displacement and rate during regulated respiration

Experimental setup

Five healthy young adults from our research group were recruited to participate in this investigation as shown in Table 4.1. Participants were instructed to remain seated and stationary while the radar and Frontier X were positioned on the torso as shown in Figure 3.8 and Figure 4.7, and radar parameters were set as described in Table 3.1. A metronome was played through noise-cancelling headphones and participants were asked to breathe at a regulated rate for 2-minute intervals at a time, for each of the following rates: 10, 13, and 15 breaths per minute. The algorithm outlined in Figure 4.1 was applied to acquire the cardiac rate and displacement waveforms. An FIR BPF with a passband from 0.9–3.0 Hz is applied to minimize the effect of the respiratory waveform when extracting the cardiac waveform and to capture the fine details of the cardiac displacement waveforms. After collecting both the radar and Frontier X data from all participants and applying the radar signal processing chain, time stamps that were produced by both devices are collected and used to synchronize both signals in time to establish a physiological basis for the extracted cardiac displacement waveforms. The features of the simultaneously recorded ECG signal will were correlated to those extracted from a radar cardiac displacement waveform. Likewise, the HR and HRV will be compared to those extracted from the Frontier X as well.

Table 4.1: Participants in regulated breathing and breath-holding investigations

Subject ID	Gender	Age	Cardio-respiratory Condition	BMI
1	F	22	Healthy	20.0
2	M	25	Healthy	25.7
3	M	29	Healthy	30.8
4	M	35	Healthy	30.9
5	F	24	Healthy	24.1

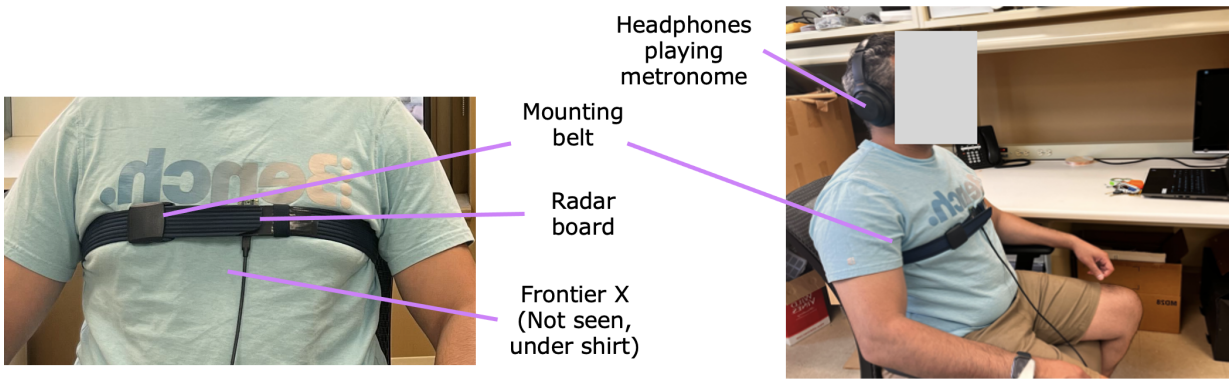


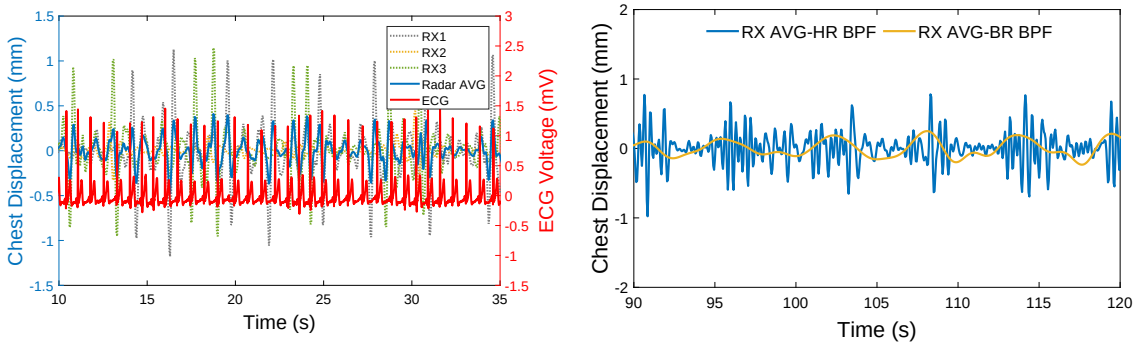
Figure 4.7: Radar set up on top of clothing using adhesive. Frontier X (not visible) is in contact with the skin under the shirt

Extracted cardiac waveforms

Radar systems are presented as a tool that can be used to continuously extract cardiac biometrics and functional cardiac waveforms with the presence of a respiration signal. This section aims to establish a physiological basis for the collected cardiac radar signal and to draw parallels between it and the gold-standard method of ECG.

For a typical adult, the chest moves about 1–12 mm and 0.01–0.5 mm due to breathing and heartbeat, respectively [14]. The latter correlates with the results observed for the sample cardiac displacement shown in Figure 4.8a detectable on the chest of the target. This figure highlights the extracted cardiac displacement from all three RX ADC channels, as well as the average waveform used as the basis for continuous HR and HRV extraction. The averaging process improves the quality of the displacement and extracted biometrics likely due to the destructive interference of the incoherent noise in the signal. From Figure 4.8b, the impact of respiratory harmonics on the extracted cardiac displacement waveform can be observed. Even when applying filters to eliminate the RR frequency, the substantial effect of these respiratory harmonics persists and can substantially alter the cardiac displacement waveform. Consequently, this influence may limit our ability to draw accurate conclusions about the underlying functional cardiac health solely based on the extracted waveform, as the amplitude is distorted. The large variation in cardiac peaks makes the peak detection required for HRV intervals challenging, which results in highly inaccurate estimates of this biometric.

Nevertheless, it is possible to extract a cardiac displacement waveform and map it to



(a) Cardiac displacement waveforms from the three RX channels

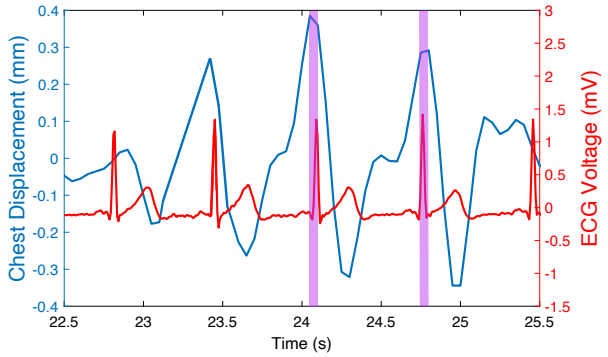
(b) Highlighting the effect of breathing harmonics on the cardiac waveform

Figure 4.8: Sample cardio-respiratory displacement waveforms during regulated breathing (subject ID = 4, regulated RR = 10 breaths/minute)

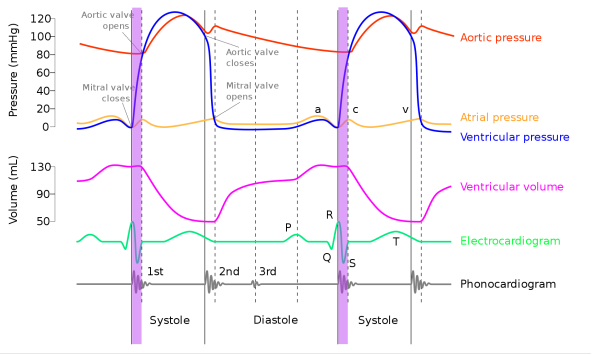
the time-synchronized ECG data to establish a physiological basis for the signal. Figures 4.9a and 4.9b highlight the isovolumetric ventricular contraction phase of the cardiac cycle, where the ventricles begin contracting, increasing pressure and preparing for blood ejection. As observed in the Wiggers diagram in Figure 4.9b, isovolumetric ventricular contraction occurs after the ventricles have filled with blood. As the ventricular muscles contract, blood volume within the ventricles remains constant since both the AV (mitral and tricuspid) valves and the semilunar (aortic and pulmonary) valves are closed, preventing any blood flow into or out of the ventricles. This prevents any blood from being ejected or refilled into the ventricles during this phase. This is observed in the radar signal in Figure 4.9a as a flat positive peak indicating no chest displacement towards or away from the radar. It is important to note that this is not observed in a majority of the peaks, but is occasionally captured, likely due to the effect of the breathing signal. The isovolumetric ventricular contraction phase aligns with the QRS-complex in the ECG signal which represents the depolarization of the ventricles, as highlighted in Figure 4.9b.

Figures 4.9c and 4.9d highlight the ventricular ejection phase of the cardiac cycle, where the ventricles undergo a series of mechanical events to efficiently pump blood. As described in the Wiggers diagram in Figure 4.9d, when the muscular walls of the ventricles contract, the pressure within the chambers rises significantly, surpassing the pressure in the arteries, opening the semilunar valves and propelling blood from the ventricles into the aorta and pulmonary arteries. The ejection process is, therefore, characterized by changes in ventricular volume as described in Figure 4.9d. Initially, the ventricular volume decreases rapidly as blood is expelled into the arteries. This rapid decrease is referred to as the rapid

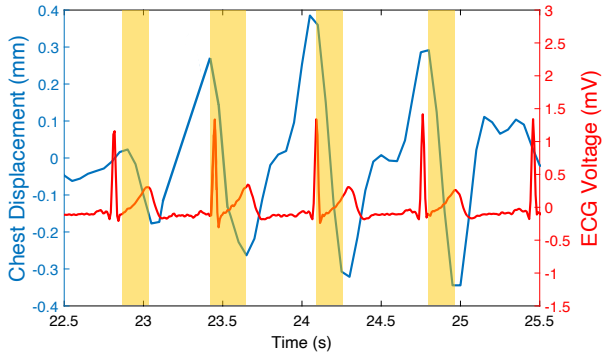
ejection phase. Subsequently, the rate of volume reduction slows down, leading to a slower ejection phase. Finally, when the ventricular pressure falls below the arterial pressure, the semilunar valves close, marking the end of ventricular ejection. This decrease in volume is reflected as a displacement away from the radar (i.e., negative displacement slope) in Figure 4.9c. Drawing a parallel to the ECG signal, ventricular ejection is associated with the period between the QRS-complex and the initial part of the T-wave, as seen in the highlighted section in Figure 4.9c.



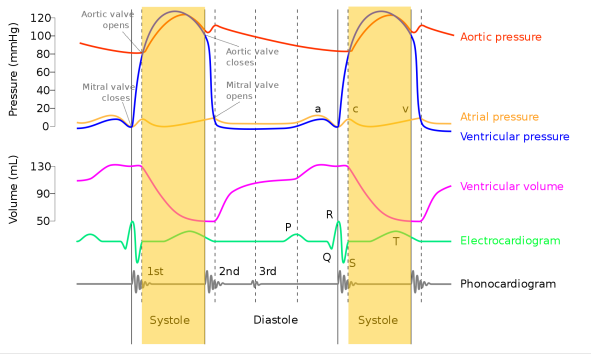
(a) Plot highlighting ventricular isovolumetric contraction in radar and ECG signals



(b) Wiggers diagram highlighting physiology of ventricular isovolumetric contraction



(c) Plot highlighting ventricular ejection in radar and ECG signals



(d) Wiggers diagram highlighting physiology of ventricular ejection

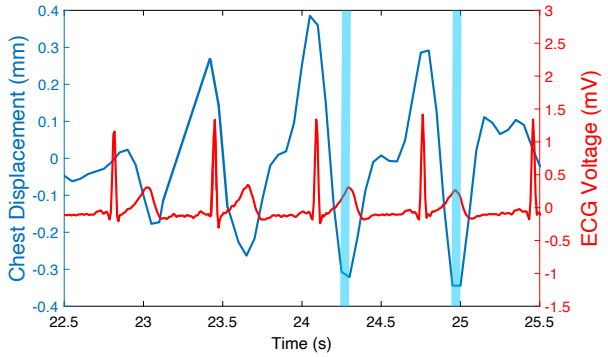
Figure 4.9: Sample ventricular contraction in radar and ECG signal, as well as the physiology of the relevant cardiac phase (subject ID = 4, regulated RR rate = 10 breaths/minute

Figures 4.10a and 4.10b describe isovolumetric ventricular relaxation, which occurs immediately after ventricular ejection and before the subsequent filling of the ventricles. The ventricles of the heart undergo a period of repolarization, where the pressure decreases in the ventricles due to muscle relaxation while the volume of blood within the ventricles remains constant as seen in Figure 4.10b. Both the AV (mitral and tricuspid) valves and the semilunar (aortic and pulmonary) valves are closed, preventing any blood flow into or out of the ventricles. this is observed in the radar signal in Figure 4.10a as a flat minimum in the displacement signal with no displacement toward or away from the radar. It is important to note that this is not observed in a majority of the peaks, but is occasionally captured, also likely due to the effect of the breathing signal. Drawing parallels to the ECG signal, this phase is associated with the T-wave, which represents the repolarization of the ventricles. The drop in pressure in this phase causes the blood in the aorta and pulmonary arteries to become greater than the ventricular pressure, leading to the closure of the semilunar valves as seen in the Wiggers Diagram in Figure 4.10b.

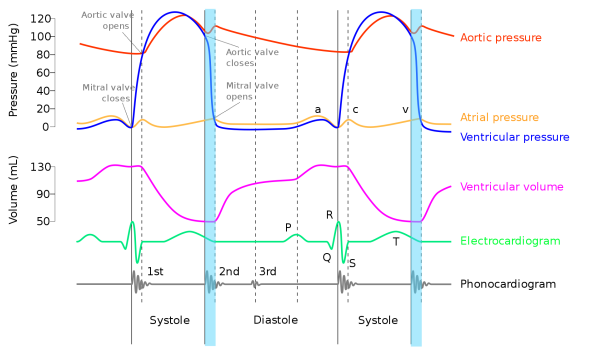
Finally, Figures 4.10c and 4.10d describe ventricular relaxation, also known as the diastole, which is the phase of the cardiac cycle when the ventricles of the heart are at rest and are preparing for the next contraction, allowing the ventricles to refill with blood and maintain efficient cardiac function. As described in the Wiggers diagram in Figure 4.10d, the relaxation of the ventricular muscles is initiated by the repolarization represented by the T-wave on the ECG. This is the rapid inflow phase and appears as a positive-sloped displacement (toward the radar) as the ventricles expand as seen in Figure 4.10c. As the ventricular muscle fibres relax, the pressure within the ventricles decreases which closes the atrioventricular AV, allowing blood to flow passively from the atria into the ventricles in what is referred to as ventricular filling. This decrease in the atrial volume can occasionally be seen as in two of the highlighted peaks in Figure 4.10c, as there is a *minor* negative-sloped displacement due to atrial contraction before ventricular filling continues. This minor displacement away from the radar aligns to the P-wave in the ECG. Nevertheless, this is not visible in most peaks, due to the effect of the breathing harmonics and their significant amplitude on the respiratory waveform. Therefore, it is difficult to conclusively map it to a cardiac event, as it could also be a sampling artifact.

Extracted cardiac rates

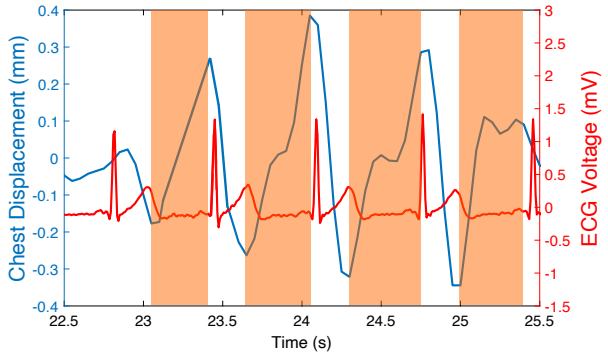
By applying an FFT to the filtered cardiac displacement waveforms, the HR can be extracted as described in the first subsection of this chapter. The result of the filtered FFT for one window of size $W = 20$ seconds is shown in Figure 4.11. Here, the x-axis is transformed from the frequency in Hz to the HR in beats per minute. Only the relevant range



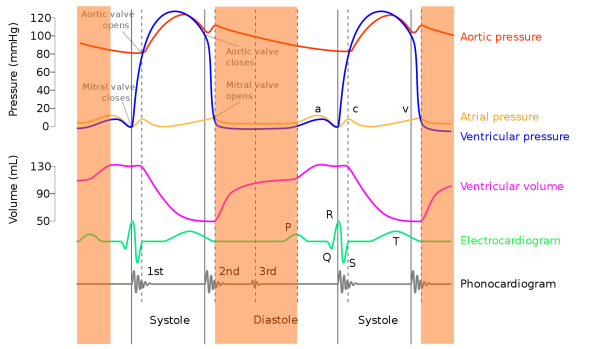
(a) Plot highlighting ventricular isovolumetric relaxation in radar and ECG signals



(b) Wiggers diagram highlighting physiology of ventricular isovolumetric relaxation



(c) Plot highlighting ventricular relaxation and filling in radar and ECG signals



(d) Wiggers diagram highlighting physiology of ventricular relaxation and filling

Figure 4.10: Sample ventricular relaxation in radar and ECG signal, as well as the physiology of the relevant cardiac phase (subject ID = 4, regulated RR = 10 breaths/minute)

of the x-axis is shown, as the resting heart rate is typically between 60–100 beats/minute. Figure 4.12 shows a continuous measure of the respiratory rate can be extracted by determining the maximum of the FFT for a 20-second sliding window with a 1-second overlap.

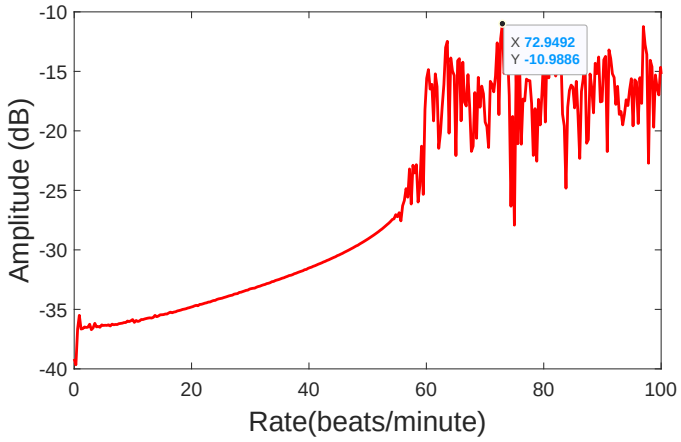


Figure 4.11: FFT of the filtered cardiac signal for one 20-second window during a regulated RR of 13 breaths/minute (Subject ID = 1, regulated RR = 10 breaths/minute)

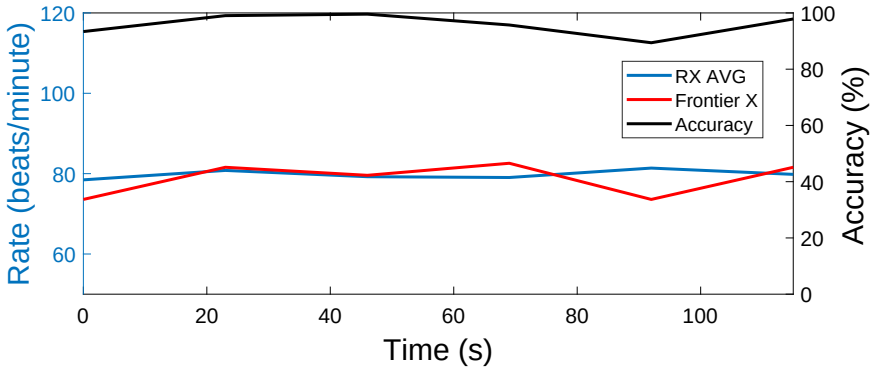


Figure 4.12: Continuous HR monitoring for 120-second window (Subject ID = 1, regulated RR = 10 breaths/minute)

The results for all five participants are shown in Table 4.2, outlining the time-averaged measured HR from the radar, the time-averaged expected HR from the Frontier X, and the time-averaged percent accuracy as extracted from all produced curves analogous to Figure 4.12 for all three metronome-regulated RRs for the five subjects. The heart rate

extraction demonstrates an average overall accuracy of 89.04% as determined by the expression in 3.1. Note that when the breathing rate is increased to 15 breaths per minute, the average accuracy noticeably decreases for all participants. This relationship is visually depicted in Figure 4.13 using a box and whisker plot. The reduced accuracy can be attributed to the overlap of the expected HR range of 60–75 BPM with the fourth or fifth harmonics of the breathing signal. These harmonics can possess a significant amplitude compared to the cardiac waveform, as illustrated in Figure 4.8b. Unfortunately, filtering out these harmonics is not feasible. Hence, more advanced signal processing techniques are necessary to effectively separate the cardiac components from the overlapping respiratory harmonics, which could yield higher quality waveforms with better accuracy results. Therefore, this investigation demonstrates the radar's ability to detect detailed cardiac displacement waveforms and rates.

Table 4.2: Metrics extracted from radar cardiac waveform versus expected values from ECG during regulated breathing

Subject ID	**Gender**	**Regulated RR (breaths/minute)**	**Measured HR (beats/minute)**	**Expected HR (beats/minute)**	**HR Accuracy (%)**
1	F	10	71.78	68.75	95.59
		13	79.79	78.75	98.68
		15	63.67	75.25	84.61
2	M	10	68.55	75.50	90.79
		13	70.95	75.78	93.63
		15	59.86	76.32	78.43
3	M	10	63.09	65.33	96.57
		13	65.04	69.73	93.27
		15	58.89	66.80	88.16
4	M	10	72.85	79.59	91.53
		13	74.22	85.00	87.32
		15	71.48	84.60	84.49
5	F	10	79.00	92.60	85.31
		13	82.91	89.40	92.74
		15	92.20	73.44	74.46
				Average	89.04

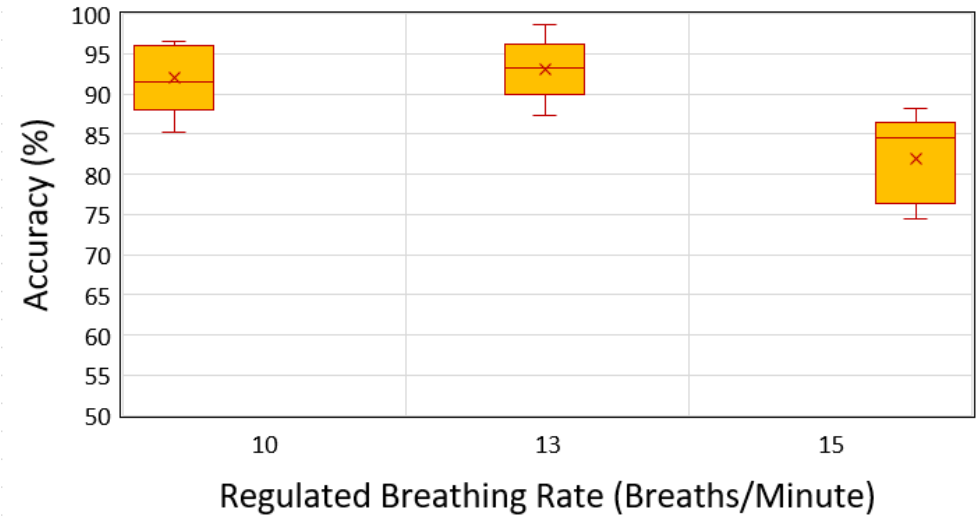


Figure 4.13: Box and whisker plot showcasing the time-averaged accuracy of the radar HR extraction for the three different regulated breathing rates

4.2.2 Cardiac displacement and rate during a breath-hold

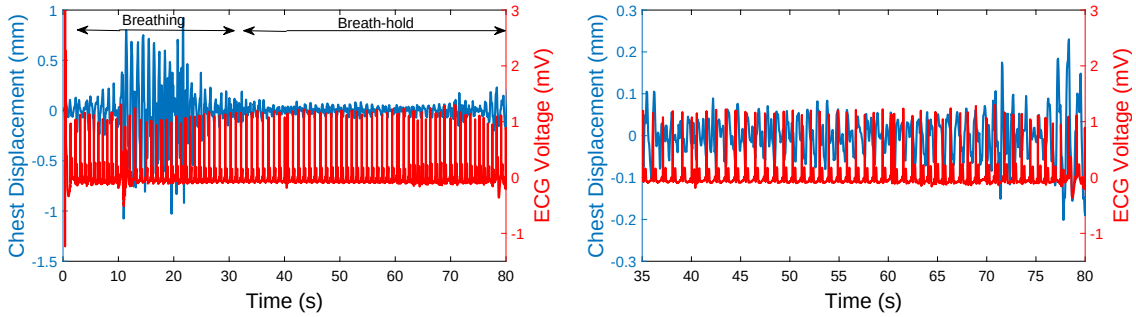
Experimental setup

The radar and Frontier X were again placed as depicted in Figure 3.8 and Figure 4.7 using an adhesive to mount the radar instead of a belt. Participants were instructed to remain seated and stationary while the radar parameters were configured according to the details provided in Table 3.1. Each of the five participants listed in Table 4.1 were instructed to breathe at their typical resting breathing rate for 20 seconds, followed by a breath-hold of at least 30 seconds. This sequence was repeated twice for each participant. The purpose of this experiment was twofold: to mitigate the impact of breathing displacement waveforms on the cardiac signal and to explore the possibility of capturing more comprehensive features of heart vibrations during the cardiac cycle. Simultaneously, the Frontier X continuously collected ECG data throughout the radar data collection period, which underwent processing based on the procedure outlined in Figure 4.1. To minimize the influence of the respiratory waveform and capture fine details of the cardiac displacement waveforms, an FIR BPF with a passband of 0.9 Hz to 9.0 Hz was implemented. As previously mentioned, the Frontier X and the radar generate timestamps which are used to synchronize the two signals. This synchronization facilitates an understanding into the relationship between the impedance-based ECG signal and the displacement-based radar signal, providing insights

into the underlying heart mechanics.

Extracted cardiac waveforms

Radar cardiac displacement signals have the potential to reveal functional information about the cardiac mechanics that can be used to either complement the electrical signal provided by ECG, which cannot provide information about mechanical heart defects or to replace it and eliminate its limitations. These limitations include the complexity, skin irritations due to the use of coupling hydrogels, and incompatibility with long-term continuous monitoring as patients are required to remain still and supine for the duration of the data collection period. Here, we demonstrate the potential use of FMCW radars for clinical health diagnostics, by showcasing that detailed waveforms that can be correlated to different phases of cardiac cycle can be established.



(a) Highlighting breathing and breath-hold periods. Note the difference in amplitude even after applying HR BPF

(b) Highlighting a full breath-hold period. Note increased detail in waveforms

Figure 4.14: Sample cardiac displacement waveforms during the breath-hold investigation

A detailed breakdown of the cardiac signal can be observed in Figure 4.15. Figure 4.15a showcases the isovolumetric contraction period where ventricular contraction is initiated. This aligns with the QRS-complex in the ECG signal which indicates the depolarization of the ventricles. In the initial phases of ventricular contraction, the AV and semilunar valves are closed, as such, the ventricles experience an increase in pressure as the volume of blood remains constant. This is observed as a nearly flat (i.e. zero-sloped) positive-valued displacement in the radar signal as there is no volumetric change in the size of the ventricles. Unlike the investigation during respiration, this feature of the cardiac wave is consistently observed in most peaks in the signal, as the effect of the breathing signal is eliminated during a breath-hold.

Figure 4.15b describes the ventricular contraction phase characterized by the rapid ejection of blood from the left and right ventricles to the systemic and pulmonary loops of the cardiac systems, respectively. This period is characterized by a rapid negative-sloped displacement away from the radar as the ventricles begin to decrease in volume. Greater detail can be observed for this period during a breath-hold than during the regulated breathing investigation in Figure 4.9c. It can be observed that for some of the peaks, the slope of the displacement is initially steeper, aligning with the rapid ejection phase of the cardiac contraction, before getting more gradual near the end of the ejection period where the rate of blood flow and therefore the displacement of ventricular walls slows down. This signal correlates to the end of the QRS-complex signal and the beginning of the T-wave of the ECG signal, as highlighted in Figure 4.15b.

Figure 4.15c highlights the ventricular isovolumetric relaxation period. In this phase of the cardiac cycle, the ventricles of the heart undergo a period of repolarization, where the pressure decreases in the ventricles due to muscle relaxation and the volume within the ventricles remains constant as no blood can flow in or out due to the closure of both AV and semilunar valves, as described previously. This is observed as a flat negative-valued displacement in the radar signal, as the position of the ventricular walls remains constant. Drawing parallels to the ECG signal, this phase is associated with the T-wave, which represents the repolarization of the ventricles. Unlike the regulated breathing investigation, this feature is observed clearly for most peaks.

Figure 4.15d describes the ventricular relaxation period characterized by the expansion of the ventricles as they prepare for the next cardiac cycle. During this period of the cardiac phase, the inflow of blood into the ventricles begins as they increase in volume during their relaxation period, thus, decreasing the pressure and opening the AV valves. This is observed as a rapid positive-sloped displacement toward the radar as the ventricles begin to fill with blood. Correlating this behaviour to the ECG, this is the period near the end of the T-wave towards the beginning of the P-wave.

Figure 4.15e highlights atrial depolarization, which was previously not consistently visible in the cardiac investigation under regulated breathing conditions. Atrial contraction refers to the phase of the cardiac cycle during which the atria contract to pump blood into the ventricles and complete the blood transfer initiated in the ventricular relaxation stage, which is essential for efficient blood flow and the overall functioning of the cardiovascular system. Specifically, the P-wave in the ECG represents the electrical depolarization and contraction of the atria. The P-wave is the first deflection observed in the ECG waveform and it is regarded as the initial point for the electrical impulse regulating the cardiac cycle. This is observed as a small negative-sloped displacement away from the radar, smaller than that associated with ventricular contraction. The atrial contraction occurs just before the

ventricular contraction, allowing for efficient filling of the ventricles with blood.

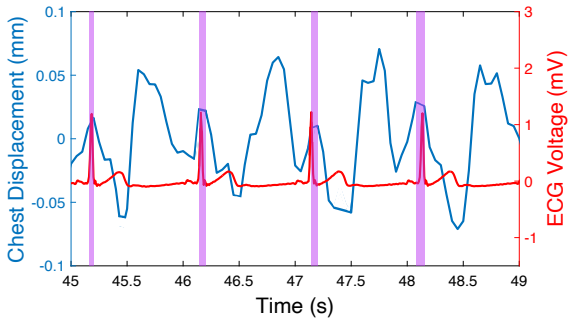
Finally, Figure 4.15f also captures atrial relaxation, which is also not visible in the cardiac investigation under-regulated breathing conditions. This is also typically not captured in ECG signals as it is often overwhelmed by the QRS-complex. Atrial relaxation refers to the phase of the cardiac cycle during which the atria relax as the ventricles prepare to contract which allows the AV valves to close, preventing the regurgitation of blood back into the atria. This is observed as a small positive-sloped displacement towards the radar, smaller than that associated with ventricular relaxation.

Extracted cardiac biometrics

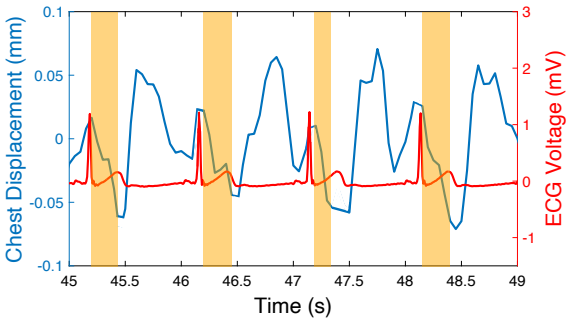
A single FFT was applied on each of the 30-second breath-hold periods after filtering and the local maxima were selected to extract the HR for all five participants. The corresponding HR recorded by the Frontier X was selected for the accuracy comparison in Table 4.3 according the expression in 3.1. An increased HR accuracy of 97.58% as determined by 3.1 is observed which is an improvement of 8.54% when compared to the results in Table 4.2 with the presence of respiration. This highlights the effectiveness of this method as a tool for continuous HR extraction.

Moreover, the detailed cardiac waveforms can now be utilized for the extraction of additional cardiac biometrics, such as the HRV. HRV plays a crucial role in diagnosing cardiac health due to its ability to provide valuable insights into the functionality of the autonomic nervous system and overall cardiovascular health. This metric characterizes the variation in time intervals between consecutive heartbeats, which is influenced by the interplay between sympathetic and parasympathetic nervous systems [3]. A healthy heart exhibits a balance between sympathetic and parasympathetic activities, resulting in a higher HRV typically in range of 50–100 ms. Reduced HRV is associated with physical inactivity, and various cardiac conditions including arrhythmia, heart failure, and increased risk of cardiovascular events. By analyzing HRV patterns, healthcare professionals can assess the autonomic regulation of the heart, identify abnormalities in cardiac function, and predict the risk of adverse cardiovascular events. Moreover, HRV analysis can also provide valuable information regarding the effectiveness of therapeutic interventions as well as athletic performance,

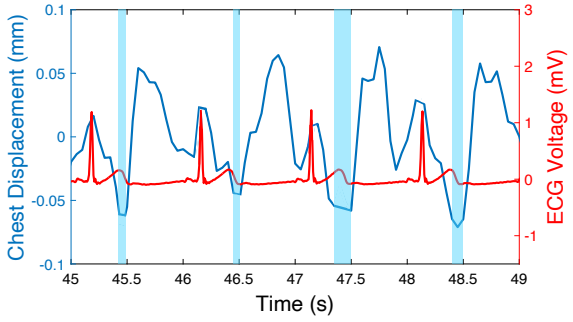
[3]The sympathetic and parasympathetic nervous systems are two branches of the autonomic nervous system, responsible for regulating involuntary bodily functions. The sympathetic system prepares the body for action, by increasing heart rate, dilating blood vessels, and releasing stress hormones. In contrast, the parasympathetic system promotes a state of relaxation and restoration by slowing heart rate, constricting blood vessels, and facilitating digestion



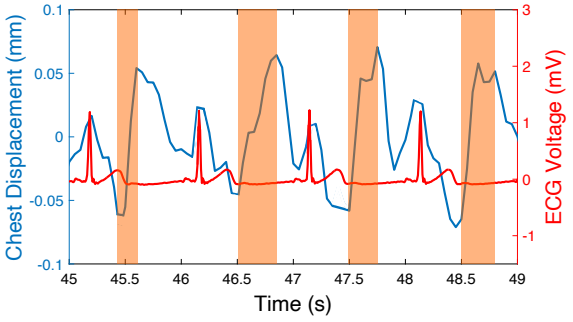
(a) Ventricular isovolumetric contraction



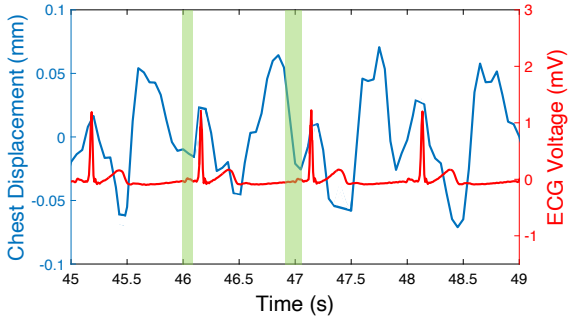
(b) Ventricular contraction (i.e., ejection)



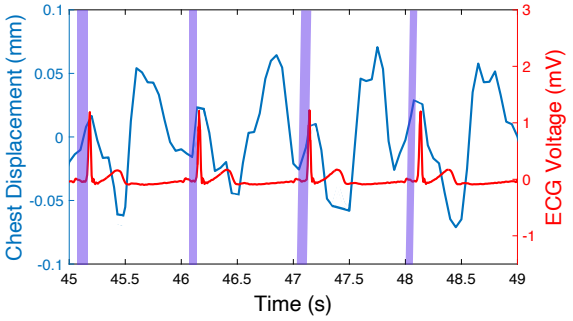
(c) Ventricular isovolumetric relaxation



(d) Ventricular relaxation (i.e., filling)



(e) Atrial contraction



(f) Atrial relaxation

Figure 4.15: Sample cardiac activities in radar and synchronized ECG signal (subject ID = 1)

making it an essential tool in diagnosing and managing cardiac health. This metric is extracted from the ECG signal using the RMSSD method as described in Figure 3.2. A similar method was used to detect the local maxima in the radar cardiac displacement peaks associated with the cardiac ventricular contraction as shown in Figure 4.16. These peaks were chosen as they are demonstrated to be analogous to the R-peaks in ECGs in Figure 4.15, which are used in the RMSSD method to determine HRV. The HRV extraction indicates high accuracy results, as can be seen in Table 4.3, with an average accuracy of 97.01% during all breath-hold periods.

Overall, this subsection highlights the improved accuracy and additional biometrics that can be reliably extracted when a high-accuracy cardiac waveform is acquired. Such waveforms reveal crucial mechanical characteristics of the heart throughout the cardiac cycle and ensure accurate HR and HRV extraction which is integral to assessing cardiac health and physical exertion due to exercise.

Table 4.3: Metrics extracted from radar cardiac waveforms versus expected values from ECG during breath-hold

ID	Gender	Measured HR (beats/minute)	Expected HR (beats/minute)	HR Accuracy (%)	HRV (ms)	Expected HRV (ms)	HRV Accuracy (%)
1	F	64.5	66.3	97.17	46.6	45.3	96.99
2	M	86.7	85.9	99.03	81.9	81.5	99.52
3	M	72.7	71.5	98.38	62.4	63.5	98.33
4	M	64.2	62.0	96.52	95.7	91.3	95.21
5	F	66.2	68.4	96.79	54.8	57.7	94.97
			Average	97.58 (STD = 1.08)		**Average**	97.01 (STD = 1.96)

Sensitivity to Placement

Data was gathered by positioning the radar at different locations on the chest to examine how the placement location influenced the quality of the extracted waveforms and biometrics. The breath-holding protocol described in the "Experimental setup" section was repeated for all five participants, for an additional two positions: The upper right chest, and the center chest (i.e., on top of the sternum). The biometrics extracted from these positions are compared to those previously extracted from the upper left chest as shown in Table 4.4. It can be observed that all positions display a high accuracy —as determined by the expression in 3.1— of over 94% for both the HR and HRV. This can be ascribed to the radar system's capability to detect heart vibrations that propagate through the torso, making them observable irrespective of the radar's placement location on the chest.

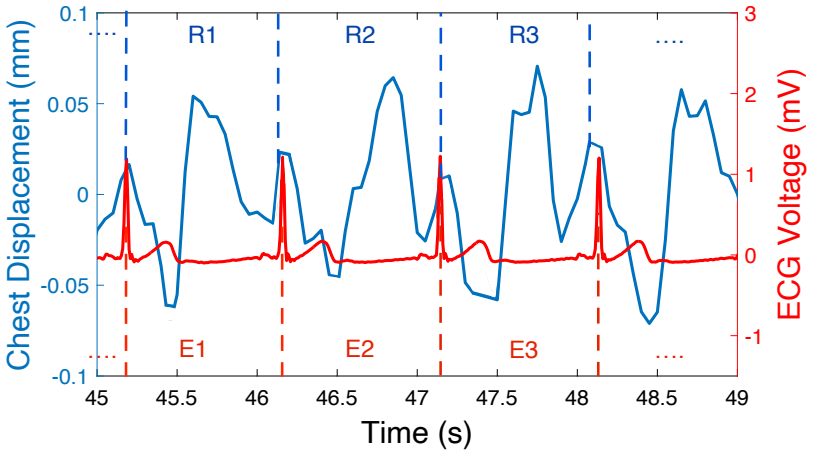


Figure 4.16: Example showcasing used HRV intervals, where the R_N indicates radar intervals and E_N indicates ECG intervals (Subject ID = 1)

Table 4.4: Sensitivity of HR and HRV to position of radar on the chest

Subject ID	**Gender**	**HR Accuracy Left Chest (%)**	**HR Accuracy Right Chest (%)**	**HR Accuracy Center Chest (%)**	**HRV Accuracy Left Chest (%)**	**HRV Accuracy Right Chest (%)**	**HRV Accuracy Center Chest (%)**
1	F	97.17	93.93	97.87	96.97	93.79	98.47
2	M	99.02	93.03	93.95	99.52	96.44	89.23
3	M	98.38	95.98	99.24	98.33	96.64	99.84
4	M	96.52	94.92	96.29	95.20	92.05	95.57
5	F	96.78	95.48	98.37	94.99	92.42	91.61
	Average	97.57 (STD = 1.08)	94.67 (STD = 1.19)	97.14 (STD = 2.08)	97.00 (STD = 1.96)	94.27 (STD = 2.18)	94.94 (STD = 4.49)

4.3 Respiratory investigation

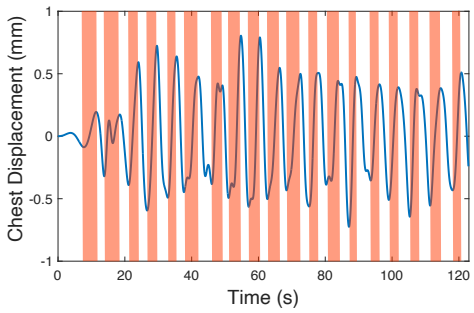
4.3.1 Stationary respiratory displacement and rate extraction

Experimental setup

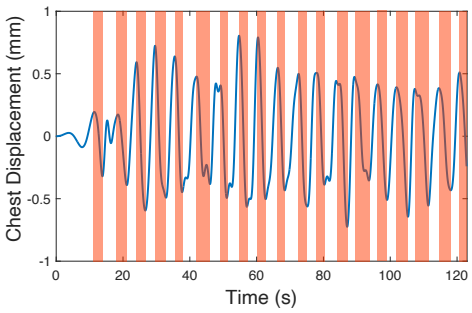
Five young adults from our research group, who self-reported healthy cardiac and pulmonary health, were selected as participants as outlined in Table 4.1. Participants were instructed to remain seated and stationary while the radar system and Frontier X were positioned on the torso, as depicted in Figure 4.7 and Figure 3.8, respectively. The radar parameters were configured as outlined in Table 3.1. To regulate participants' breathing, a metronome was played through noise-cancelling headphones. Each participant was instructed to breathe at a controlled pace for 2-minute intervals, and this procedure was repeated for respiratory rates of 10, 13, and 15 breaths per minute. The RR and respiratory displacement waveforms were obtained using the algorithm described in Figure 4.1. To minimize the effect of higher-frequency harmonics and noise due to the cardiac waveform, a FIR BPF ranging from 0.2–0.6 Hz (i.e., 12–36 breaths/minute) was applied. The results were compared to the ground-truth metronome.

Extracted respiratory waveforms

Figure 4.17 shows a sample of the extracted radar data from one of the participants. The respiratory waveform is captured successfully while highlighting the positive-sloped displacement of the chest towards the radar during inhalation in Figure 4.17a. This displacement indicates inhalation as the diaphragm, located at the base of the lungs, contracts and moves downward, expanding the chest cavity and causing the lungs to expand as well. As the lungs expand, oxygen-rich air is drawn through the respiratory tract, filling the alveoli where oxygen is transferred into the bloodstream to be carried to the body's cells for energy production. The negative-sloped displacement of the chest away from the radar during exhalation in Figure 4.17b is observed as the diaphragm and the intercostal muscles between the ribs relax, which is a passive process. As the diaphragm moves back upward and the chest cavity decreases in size, the lungs compress and the air is expelled. The carbon dioxide is carried back to the lungs by the bloodstream, passing from the blood into the alveoli and is then expelled from the body through the nose or mouth.



(a) Highlighted inhalation periods



(b) Highlighted exhalation periods

Figure 4.17: Sample respiratory waveform highlighting inhalation and exhalation periods (subject ID = 1, regulated RR = 10 breaths/minute)

Extracted respiratory rates

By applying an FFT to the filtered respiratory displacement waveforms, the RR can be extracted. The result of the filtered FFT for one window of size $W = 20$ seconds can be seen in Figure 4.18. Here, the x-axis is transformed from the frequency in Hz to the RR in breaths per minute. Figure 4.19 shows a continuous measure of the respiratory rate can be extracted by determining the maximum of the FFT for a 20-second sliding window with a 1-second overlap.

The results for all five participants are shown in Table 4.5, outlining the time-averaged measured RR, the expected RR based on the metronome, and the time-averaged percent accuracy as outlined from all the curves produced analogous to Figure 4.19, for all test subjects. The breathing rate extraction demonstrates an average overall accuracy of 98.34%. The relationship between the regulated metronome breathing rate and the calculated respiratory rate is shown in Figure 4.13 using a box and whisker plot. All three rates are accurately detected with over 95% accuracy. Therefore, this investigation demonstrates the radar's ability to detect accurate respiratory displacement waveforms and rates.

4.3.2 Differentiating between different breathing patterns

Experimental Setup

In this section aimed at investigating various breathing types, a group of ten healthy young adults was selected from our research group as shown in Table 4.6. To establish different

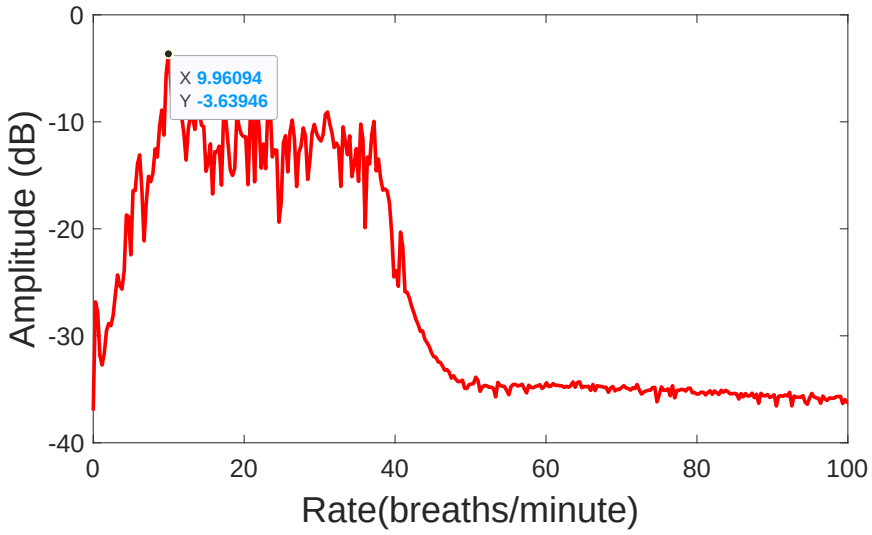


Figure 4.18: FFT of the filtered respiratory signal for one 20-second window during a regulated RR of 10 breaths/minute (Subject ID = 1)

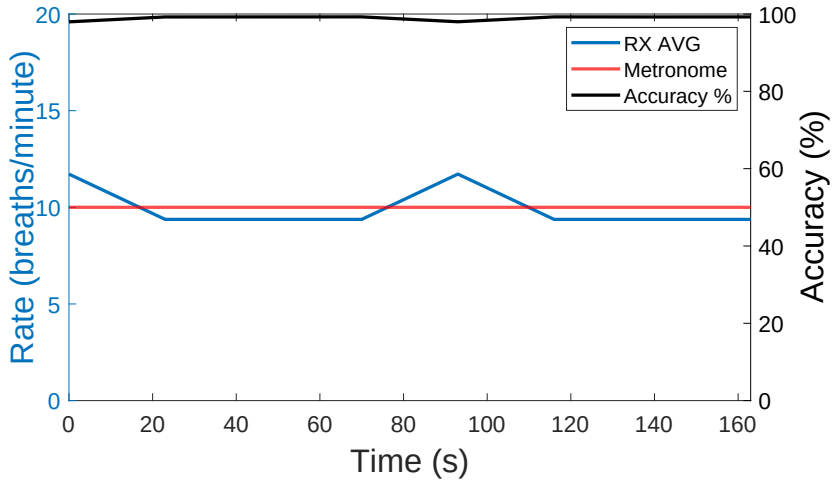


Figure 4.19: Continuous RR monitoring (Subject ID = 1)

Table 4.5: Metrics extracted from radar respiratory waveform versus expected values from metronome during regulated breathing

Subject ID	**Gender**	**Measured RR (breaths/minute)**	**Expected RR (breaths/minute)**	**RR Accuracy (%)**
1	F	10.25	10	97.50
		13.27	13.00	97.92
		14.65	15.00	97.67
2	M	9.96	10.00	99.60
		12.60	13.00	96.92
		14.75	15.00	98.33
3	M	10.03	10.00	99.70
		13.18	13.00	98.62
		15.53	15.00	96.47
4	M	9.96	10.00	99.60
		12.89	13.00	99.15
		14.94	15.00	99.60
5	F	9.86	10.00	98.60
		12.89	13.00	99.15
		14.45	15.00	96.33
			Average	98.34

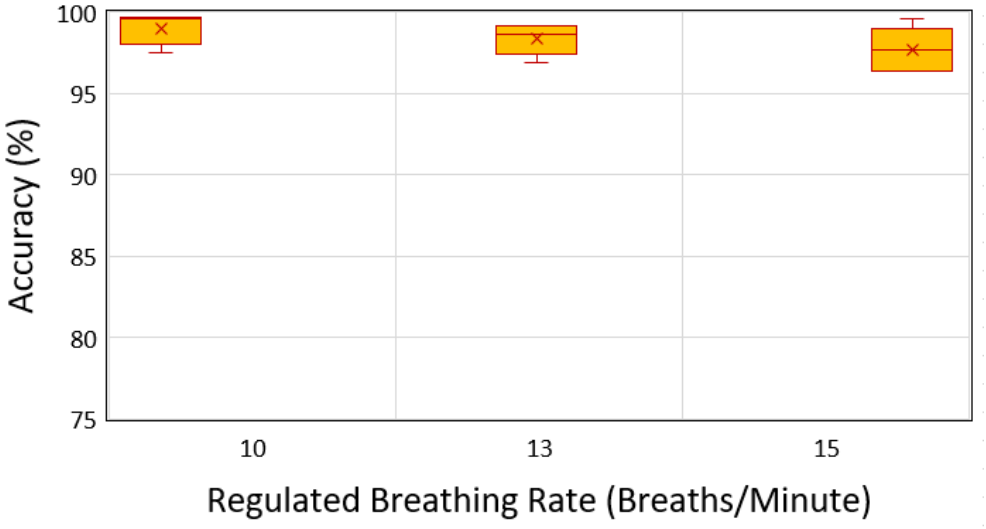


Figure 4.20: Box and whisker plot showcasing the time-averaged accuracy of the radar RR extraction for the three different regulated breathing rates

breathing rates, the participants were equipped with noise-cancelling headphones through which a metronome played, and the setup in Figure 3.8 was used with the radar mounted on the torso with a belt. Participants were instructed to remain seated and stationary and maintain a breathing rate of 10 breaths per minute for 3 minutes. This phase aimed to simulate a resting breathing state. Following this period, the participants were then asked to engage in a breath-hold for a minimum of 30 seconds aimed to mimic a state of apnea, where breathing temporarily ceases. These two phases were repeated twice more, with the breathing rate increasing to 15 and 20 breaths per minute for another 3-minute interval each with interleaved 30-second breath-holding periods. The entire protocol with three regulated breathing and three breath-holding phases was repeated with a deep breath instead of a shallow resting breath aimed to simulate a laboured breathing pattern, as observed during physically demanding or stressful situations.

Extracted waveforms

From the waveforms in Figure 4.21, clear amplitude differences can be observed in periods of shallow breathing, deep breathing, and breath-holding. A statistical thresholding method was devised to differentiate between the aforementioned breathing patterns involving additional data collected from the various participants aside from the previously

Table 4.6: Breakdown of participants in ambulatory and breath-type investigations

Subject ID	Gender	Age	Cardio-respiratory Condition	BMI
1	F	24	Healthy	24.1
2	F	22	Healthy	20.0
3	F	18	Healthy	25.0
4	F	32	Healthy	29.1
5	M	23	Healthy	32.4
6	M	35	Healthy	30.9
7	M	29	Healthy	30.8
8	M	38	Healthy	38.1
9	M	37	Healthy	33.1
10	M	25	Healthy	25.7

described experimental protocol. First, to measure the maximum breath-hold displacement, the amplitudes (min to max) of the peaks detected in the filtered chest displacement over 20-second windows with 1 second of overlap were considered. Around 300 measurements were gathered from a group of 8 participants to establish this statistical parameter. Given that the amplitude values in a breath-hold scenario are always non-negative, they follow a log-normal distribution [120]. After taking the natural logarithm, the mean and standard deviation of the data, are -4.6 and 0.9, respectively. To ensure a higher threshold level, which is preferable to avoid missing breath-hold (i.e., apnea) periods, the empirical rule is applied. According to this rule, 99.7% of the samples lie within three standard deviations of the mean [121]. Employing the three-sigma rule of thumb, the threshold is calculated as -1.89 in the logarithmic scale, which approximately equals 0.15 mm when the exponential function is applied. Hence, any detected peak amplitude below 0.15 mm is considered indicative of a breath-hold period. Similarly, the deep breathing maximum threshold was determined, with 8 participants breathing at 10 breaths per minute, and extracting the total min-to-max amplitudes of the peaks detected in the filtered chest displacement signal over 20-second windows with 1 second of overlap, yielding 360 samples. The three-sigma rule was used to determine the deep breathing maximum threshold. If amplitude values are larger than the shallow breathing threshold but smaller than the deep breathing threshold they were classified as a deep breath. Amplitudes larger than the maximum deep breathing threshold could be attributed to participant motion artifacts. Finally, a similar procedure was followed to determine the threshold for shallow breathing as well, as eight participants were asked to breathe at 18 breaths per minute, which is the average resting breathing rate for an adult [122]. The min-to-max amplitudes of the

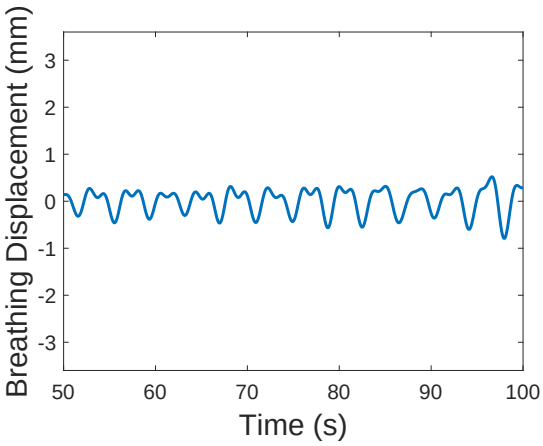
peaks detected in the filtered chest displacement over 20-second windows with 1 second of overlap were considered, extracting around 309 samples. The procedure for determining the threshold was as outlined previously, but to avoid over-estimating the number of shallow breaths, the threshold was chosen as the value two standard deviations away from the mean (i.e., includes 95% of amplitude values), as detecting periods of deep (laboured) breathing was considered more preferable to periods of normal shallow breathing. If amplitude values are larger than the breath-holding threshold but smaller than the shallow breathing threshold they were determined to correspond to a shallow breath. A summary of the extracted statistical parameters is in Table 4.7.

Table 4.7: Thresholding statistical parameters

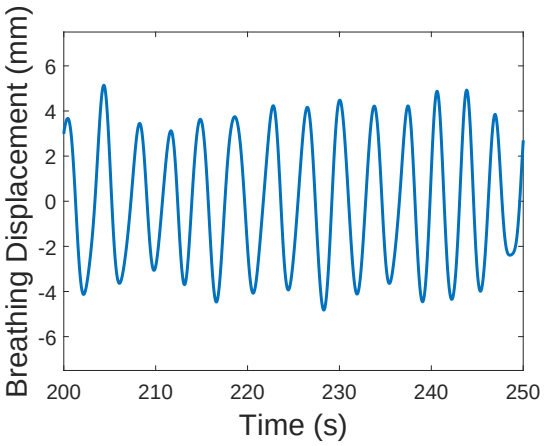
Breathing Type	**Number of Samples**	**Log-normal Mean**	**Log-normal Standard Deviation**	**Log-normal Threshold**	**Threshold (mm)**
Breath-hold	300	-4.601	0.901	(mean + 3 σ) -1.898	0.150
Shallow	309	0.585	0.351	(mean + 2 σ) 1.287	3.622
Deep	360	1.7547	0.201	(mean + 3 σ) 2.1567	8.643

Using the data collected from participants as described in the "Experimental setup" section of this investigation, the threshold values can be applied to define different periods of breath-holds, shallow breathing, and deep breathing. Figure 4.21 showcases sample waveforms of different breathing types. The filtered waveform for each test subject was considered in 20-minute sliding windows with 1 second of overlap, and compared to threshold values in Table 4.7.

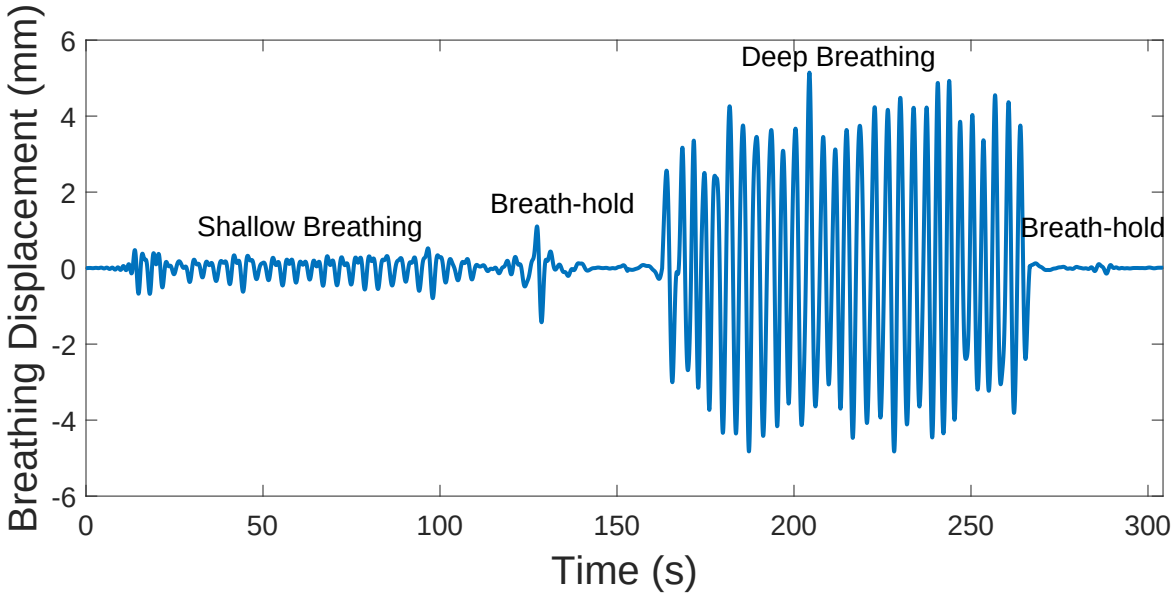
Since the duration of breath-holding and breathing are specifically outlined by the protocol for both shallow and deep breathing, the data can easily be labelled for comparison to the result after the threshold is applied, as shown in the confusion matrix in Figure 4.22. It can be observed that deep breathing and breath-holding have a very high true positive rate, which was the desired outcome as they represent two potential pathological breathing patterns: laboured breathing and apnea, respectively. Shallow breathing has the smallest true positive rate and is sometimes detected as either a deep breath or a breath-hold. This could be attributed to the fact that the amplitude of a shallow breath is highly dependent on the subject and often has a large defined range in the literature between 1–12 mm, unlike a breath-hold or a deep breath which can objectively be defined [14]. Alternatively, this could be attributed to the fact that many participants tend to take a few deep breaths before a breath-hold, even during the shallow-breathing dataset collection. Finally, this



(a) Shallow breathing displacement waveform



(b) Deep breathing displacement waveforms



(c) Stitched shallow breathing, breath-hold, and deep breathing periods to highlight amplitude variation (Subject ID = 1, RR = 15 breaths/minute)

Figure 4.21: Sample respiratory displacement waveforms highlighting various types of breathing

could also be due to an overlap between shallow breathing and other categories in the same sampling window. similarly, some deep breathing periods are detected as breath-holds, and some breath-holds are detected as shallow breaths, which could also be attributed to the overlap of different periods in a given window as well.

Therefore, this section of the investigation shows that the system can differentiate between different breathing patterns through the statistical thresholding method employed. Although this method might not be the most suitable for real-time continuous monitoring, it is an excellent primer to more efficient machine learning methods that could further improve accuracy and reduce latency.

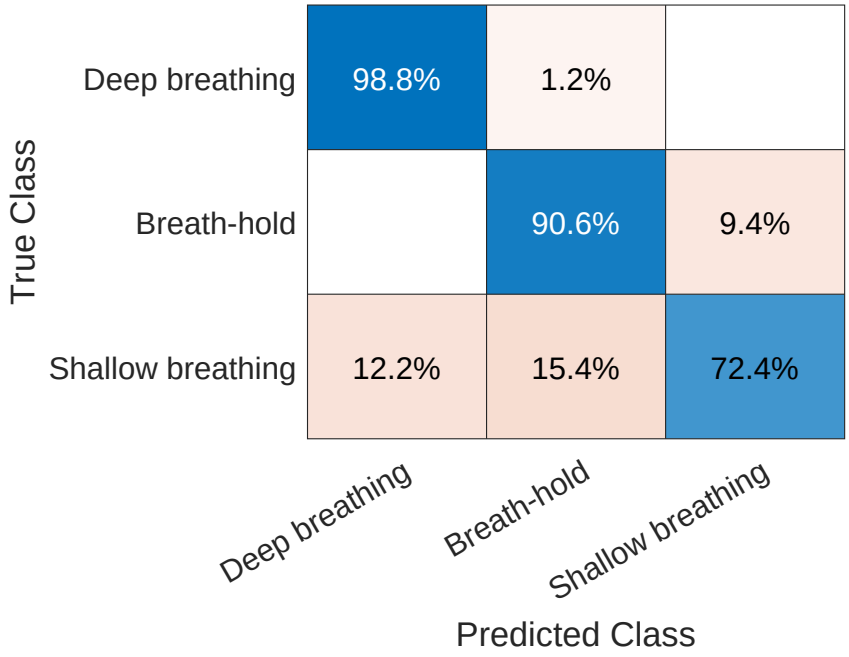


Figure 4.22: Row-normalized confusion matrix of different breathing types to display the true positive rates

4.3.3 Ambulatory respiratory displacement and rate extraction

Experimental Setup

In this study, the ten healthy participants in Table 4.6 were equipped with noise-cancelling headphones through which a metronome was played while wearing both the belt-mounted

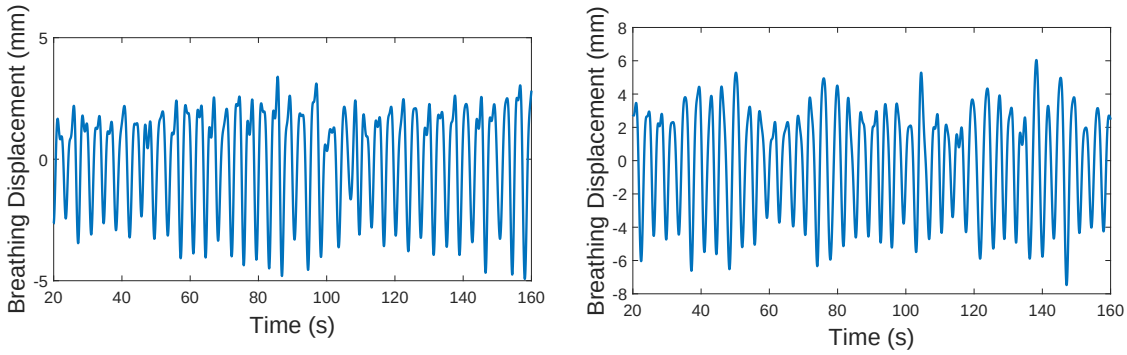
radar system on their chest as well as the Frontier X on their torso as in Figure 3.8. As previously mentioned, the Frontier X has the capability of estimating the RR, however, it was optimized for cardiac performance. As such its' ability to accurately track the metronome-set rate will be compared to that of the radar system. A treadmill was set to a leisurely walking pace of 1.5 MPH. The participants were instructed to breathe at a rate of 15 breaths per minute for a duration of 3.5 minutes. Afterward, the breathing rate was increased to 18 breaths per minute for another 3.5 minutes, followed by a further increase to 20 breaths per minute for another 3.5 minutes to mimic the increase in breathing rate due to exertion during exercise. Once these measurements were completed, the treadmill speed was adjusted to a slow jog of 3.0 MPH, and the breathing protocol was repeated accordingly. This procedure allowed for the collection of data under different treadmill conditions, providing insights into the effects of exercise intensity on the quality of extracted respiratory waveforms and the accuracy of extracted biometrics.

Extracted biometrics

As can be observed in the sample in Figure 4.23, a detailed chest displacement due to breathing can still be extracted during exercise with the near-field system. This is crucial as they can potentially be used for extracting additional biometrics like the tidal volume, inspiratory and expiatory volume, as well as inhalation and expiration time and velocity among others. These detailed respiratory waveforms are observed for all 10 participants. Note the amplitude of these extracted waveforms, particularly in Figure 4.23b, according to threshold values in Table 4.7, these could be categorized as deep breaths, which is likely due to the nature of laboured breath during exercise.

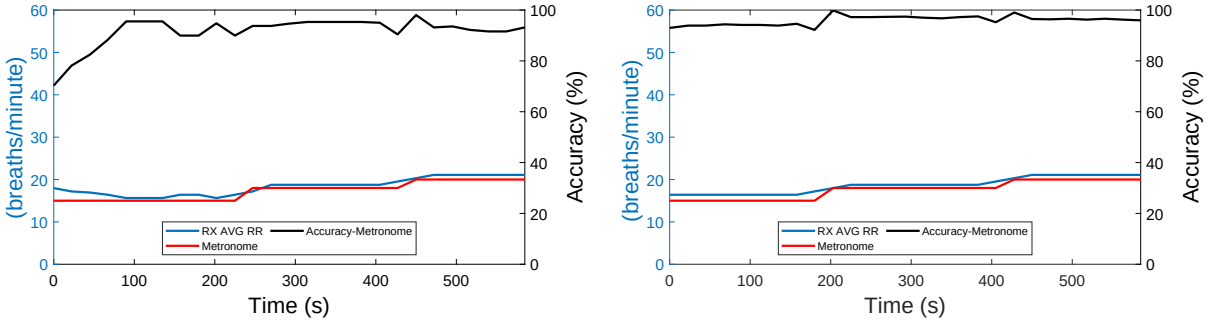
As previously specified, by applying an FFT in 20-second windows with 1-second overlap to the filtered respiratory displacement waveforms, the RR can be extracted. It can be observed that the RR extraction yields high accuracy (as determined using 3.1) throughout the measurement, as shown in the sample in Figure 4.24. Similar accuracy results are observed for all subjects, with an overall averaged accuracy of 92.60% (STD = 7.39) for a treadmill speed of 1.5 MPH and 87.58% (STD = 11.35) for a treadmill speed of 3.0 MPH using the radar. The time-synchronized RR results yielded by the Frontier X show a significantly lower average accuracy rate of 73.44% (STD = 20.15) for a treadmill speed of 1.5 MPH and 46.80% (STD = 26.16) for a treadmill speed of 3.0 MPH. For both the radar and Frontier X, the accuracy drops at the faster exercise speed, likely due to motion artifacts. Overall, the radar shows higher accuracy results with smaller standard deviation values, indicating a smaller spread for the estimated RR values.

As summarized in the histograms in Figure 4.25a for a speed of 1.5 MPH, 89.1% of the



(a) Treadmill speed of 1.5 MPH (b) Treadmill speed of 3.0 MPH

Figure 4.23: Zoomed-in sample extracted continuous respiratory chest displacement for treadmill exercises (Subject ID = 1)

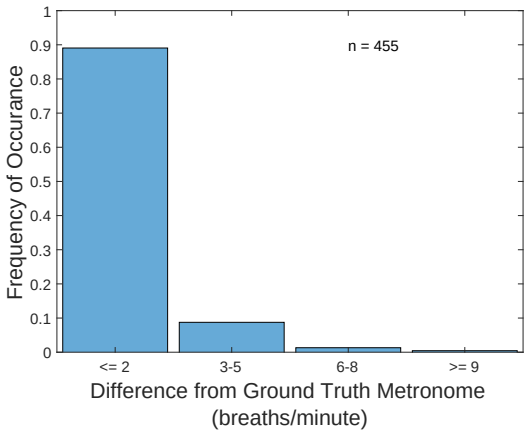


(a) Treadmill speed of 1.5 MPH (b) Treadmill speed of 3.0 MPH

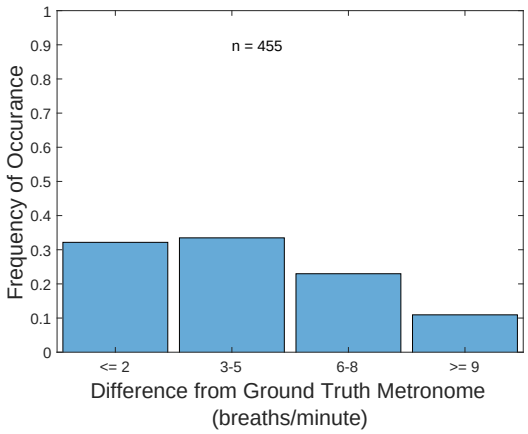
Figure 4.24: Zoomed-in sample extracted continuous RR for treadmill exercises (Subject ID = 1)

continuously acquired RR values are less than 2 breaths per minute away from the ground truth metronome, while in Figure 4.25b, this number decreases to 32.2% for the Frontier X at the same treadmill speed. Likewise, in Figure 4.25c, 74.6% of the continuously acquired RR values are less than 2 breaths per minute away from the ground truth metronome, while in Figure 4.25d, this number decreases to just around 6.4% for the Frontier X, with more than 56.7% of RR samples being over 9 breaths per minute away from the ground truth metronome, indicating that the radar achieves more accurate results.

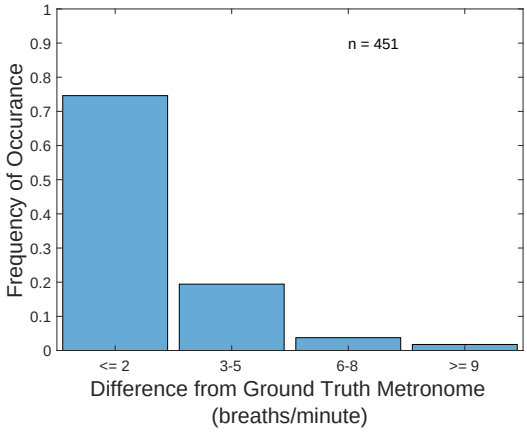
Therefore, this section highlights the ability of the radar to extract accurate respiratory waveforms and rates during mild and intense exercise.



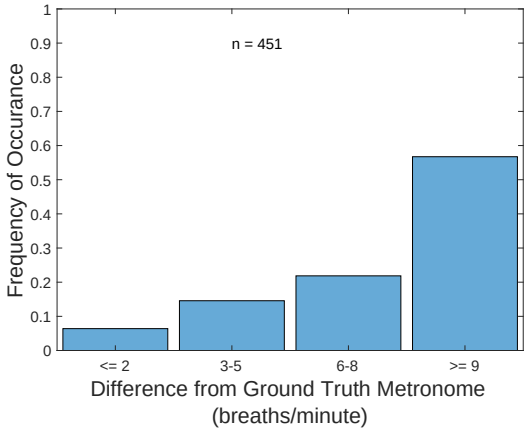
(a) Radar RR at a treadmill speed of 1.5 MPH



(b) Frontier X RR at a treadmill speed of 1.5 MPH



(c) Radar RR at a treadmill speed of 3.0 MPH



(d) Frontier X RR at a treadmill speed of 3.0 MPH

Figure 4.25: Percent of extracted RR from the radar (left) and Frontier X (right) a certain number of breaths per minute away from the ground truth metronome at treadmill speeds of 1.5 MPH and 3.0 MPH

Chapter 5

Conclusion

5.1 Summary

Chapter 1 presents the motivation for the work, and an overview of the thesis. Chapter 2 presents relevant background physiological information regarding the cardiac and respiratory cycle to provide an understanding of the physical phenomena observed in this thesis. Background information regarding conventional cardio-respiratory monitoring techniques is presented as well, highlighting both state-of-the-art methods and their shortcomings, as well as other experimental methods and their limitations. Gold standard cardiac monitoring methods like ECG cause skin irritation, aren't compatible with continuous ambulatory measurements, and are limited to diagnosing conduction disorders. Likewise, respiratory gold standard methods like spirometry require patient participation, are physically taxing making them unsuitable for patients with comorbidities, and do not provide a continuous measurement of RR and respiratory biometrics. Radar methods have been researched as an alternative to these methods due to their ability to monitor both cardiac and respiratory health at the same time, and since they do not need to be in direct contact with the skin. Nevertheless, these methods face limitations due to the presence of multiple targets, RBMs, multi-path and environmental noise, as well as the overlap of cardiac and respiratory harmonics. Near-field radar methods have shown promise in maintaining the contactless nature of radar while overcoming the limitation of both radar and conventional methods. This section also covers the basics of FMCW radar signal.

Chapter 3 covers the radar system and ground truth devices used, as well as the experimental setup. The thesis makes use of a 60 GHz Infineon radar module, a health monitoring belt (Frontier X) for use as a ground truth ECG for the cardiac signal and as a comparison

device for performance accuracy in some of the respiratory investigations. Additionally, we make use of a metronome as the breathing ground truth. To verify acceptable radar antenna performance with skin in the near field, a sweep of the skin distance from the radar antennas is performed, as well as system performance when antennas are radiating in free space. The simulations indicate acceptable behaviour when skin is in the near field.

Chapter 4 summarizes the general digital signal processing for cardio-respiratory waveform and rate extraction in the first section. The second section focuses on cardiac displacement waveform and HR extraction. In this section, the effect of breathing on the cardiac signal is observed in an investigation where the cardiac signal is extracted at regulated breathing rates. Cardiac waveforms are extracted during breath-hold periods to eliminate the effect of breathing on the cardiac waveforms, which enables the extraction of highly detailed curves. For both investigations, the radar cardiac displacement waveforms are mapped to ECG to establish a physiological basis for the signal. Moreover, the curves are used to continuously extract cardiac biometrics accurately including HR and HRV with high accuracy. The final section of this chapter focuses on extracting respiratory waveforms and accurate continuous RRs when a subject is stationary and during various intensities of exercise (i.e., walking or jogging on a treadmill). Additionally, a statistical method is presented to differentiate between different types of breathing such as breath-holds (to simulate apnea), shallow-breathing, and deep breathing to simulate laboured breathing with a high true positive rate.

5.2 On-going and future work

5.2.1 PoE radar system

Some investigations have explored the idea of using multiple radars and/or sensors to improve the performance of radar systems, particularly when a subject is moving [95, 96]. Moreover, after proving the effectiveness of radar systems in near-field applications for cardiac and respiratory monitoring, particularly respiratory monitoring during physical exercise, it might be desirable to use multiple near-field radars in a room to monitor multiple subjects at the same time (i.e., on multiple treadmills in a gym). For these sorts of applications, high data throughput is essential to acquiring a high frame rate which would improve the quality of extracted cardiac and respiratory displacement waveforms and corresponding biometrics. Therefore, the speed and scaling compatibility provided by power over ethernet (PoE) offers several advantages:

- Stable and reliable network connectivity: Ensures consistent and uninterrupted data transmission. This reliability makes it particularly suitable for critical applications such as patient monitoring, where a continuous connection is crucial for timely and accurate data exchange.

- Fast data transfer speeds: Can achieve fast data transfer speeds especially when compared to congested protocols like Wi-Fi. This feature is especially advantageous for bandwidth-intensive tasks like large radar file transfers, where high-speed data transmission is essential to minimize delays and optimize performance. PoE can achieve anywhere between 10/100 Mbps to Gbps transfer speeds.

- Security: Enhances security, particularly in environments with sensitive data such as patient information. By combining power and data transfer over the Ethernet infrastructure, PoE reduces potential vulnerabilities associated with separate power and data connections, thereby providing enhanced security for patient data and other sensitive information.

- Scalability: Since PoE-enabled devices receive power directly from the Ethernet infrastructure, they are not reliant on proximity to power outlets. This eliminates the need for additional electrical infrastructure and allows for more flexible device placement, simplifying installation and offering scalability options for expanding networks without requiring significant modifications to the power infrastructure. They can also be connected directly to a local server

- Cost-effective: This solution combines power and data transfer. Integrating power and data over a single Ethernet cable reduces the complexity and cost associated with separate power supplies and wiring, making PoE a more streamlined and economical option for network deployments.

Work has been done on the design, bring-up, and firmware for a custom PCB to stream the data from the Infineon radar module through a PoE module with 10/100 Mbps transfer speeds, both of which interface to a central Infineon MCU (XMC4400). Details regarding the system diagram and firmware flowchart can be found in Appendix B.

5.2.2 2.5 GHz radar system

Many CW radar systems make use of radar systems operating at 2.5 GHz [91, 92]. Frequencies in the range of 100–2.5 GHz have a penetration depth of about 1.5–0.5 cm through

the human body, whereas at 60 GHz electromagnetic waves have a depth penetration of around 2.0 mm [123, 118]. Therefore, a richer spectrum as well as more detailed cardiac and respiratory waveforms could potentially be extracted using this lower frequency range. Nevertheless, as indicated by A.9, a larger wavelength is not as sensitive to the small vibrations of the chest due to respiration and cardiac activity. Therefore, a recommendation is made to create a system with two non-overlapping frequency bands to avoid any interference: One radar operating at 2.45 GHz to maximize tissue penetration, and the mmWave radar to improve the detection resolution.

Appendix C outlines the custom PCB designed for the proof of concept for this stage. The prototype is designed to interface with a Raspberry Pi microcontroller for data collection and signal processing.

5.2.3 Experimental improvements

Miscellaneous improvements to the system and experimental design are outlined below:

- Additions to the mounting system are needed to ensure the belt distance from the chest is more consistent. These could include some fabric or a foam layer between the chest and radar that is easily compressible and will not dampen the vibration of the chest due to respiration and cardiac movements. It's important that the material be selected carefully as it must not affect the electromagnetic wave propagation.

- Mapping signals, particularly the complex cardiac signal, to more than one physiological gold standard. Similar work was investigated by Will *et al.* where the results from their CW system were mapped against electrical-based systems like ECG and auscultation-based methods like PCG which helps in capturing finer details associated with valvular behaviour[11].

5.3 Publications

Below are the publications and research activities relevant to the work in this thesis:

- S. Abu-Sardanah, A. Gharamohammadi, O. M. Ramahi and G. Shaker, "A Wearable mm-Wave Radar Platform for Cardiorespiratory Monitoring," in IEEE Sensors Letters, vol. 7, no. 6, pp. 1-4, June 2023, Art no. 6003404, doi: 10.1109/LSENS.2023.3277365. [**Published**].

- S. Abu-Sardanah, O. M. Ramahi and G. Shaker, "A Wearable mmWave Radar System for Continuous Cardiopulmonary Monitoring," AP-S/USRI 2023 International Symposium 2023, Portland, Oregon. [**Completed, unpublished**].
  - Received IEEE C. J. Reddy Travel Award
- S. Abu-Sardanah, Y.Wang, A. Gharamohammadi, O. M. Ramahi and G. Shaker, "A Wearable mmWave Radar System for Respiratory Health Monitoring," Journal TBD. [**Under preparation**].
- Study to extract cardio-respiratory data from older adults, both healthy and with cardio-respiratory illnesses, to investigate the system's performance as a potential diagnostic tool. [**Active study and recruitment at the Schlegel-UW Research Institute for Aging**].

References

[1] World Health Organization (WHO), "Cardiovascular diseases (CVDs)," 2020. [Online]. Available: https://www.who.int/news-room/factsheets/detail/cardiovascular-diseases-(cvds)

[2] World Health Organization (WHO) , "Cardiovascular diseases," 2023. [Online]. Available: https://www.who.int/health-topics/cardiovascular-diseases/#tab=tab_1

[3] W. W. Labaki and M. K. Han, "Chronic respiratory diseases: A global view," *The Lancet Respiratory Medicine*, vol. 8, pp. 531–533, Jun. 2020.

[4] G. C. R. D. Collaborators, "Prevalence and attributable health burden of chronic respiratory diseases, 1990–2017: A systematic analysis for the global burden of disease study 2017," *The Lancet Respiratory Medicine*, vol. 8, no. 6, pp. 585–596, 2020.

[5] World Health Organization (WHO), "Asthma," 2021. [Online]. Available: https://www.who.int/news-room/fact-sheets/detail/asthma

[6] Y. Szekely, Y. Lichter, S. Sadon, L. Lupu, P. Taieb, A. Banai *et al.*, "Cardiorespiratory abnormalities in patients recovering from coronavirus disease 2019," *Journal of the American Society of Echocardiography*, vol. 34, pp. 1273–1284, Dec. 2021.

[7] J. L. Anderson, C. D. Adams, E. M. Antman, C. R. Bridges, R. M. Califf, D. E. Casey *et al.*, "ACC/AHA 2007 guidelines for the management of patients with unstable angina/non–ST-elevation myocardial infarction," *Circulation*, vol. 116, no. 7, Aug. 2007.

[8] L. Stingeni, E. Cerulli, A. Spalletti, A. Mazzoli, L. Rigano, L. Bianchi, and K. Hansel, "The role of acrylic acid impurity as a sensitizing component in electrocardiogram electrodes," *Contact Dermatitis*, vol. 73, pp. 44–48, Jul. 2015.

[9] M. R. Miller, J. Hankinson, V. Brusasco, F. Burgos, R. Casaburi, A. Coates, R. Crapo, P. Enright, C. Van Der Grinten, P. Gustafsson *et al.*, "Standardisation of spirometry," *European respiratory journal*, vol. 26, no. 2, pp. 319–338, 2005.

[10] G. L. Ruppel, B. W. Carlin, M. Hart, and D. E. Doherty, "Office spirometry in primary care for the diagnosis and management of copd: national lung health education program update," *Respiratory care*, vol. 63, no. 2, pp. 242–252, 2018.

[11] C. Will, K. Shi, S. Schellenberger, T. Steigleder, F. Michler, J. Fuchs, R. Weigel, C. Ostgathe, and A. Koelpin, "Radar-based heart sound detection," *Scientific Reports*, vol. 8, no. 1, p. 11551, 7 2018.

[12] F. Michler, K. Shi, S. Schellenberger, T. Steigleder, A. Malessa, L. Hameyer, N. Neumann, F. Lurz, C. Ostgathe, R. Weigel, and A. Koelpin, "A clinically evaluated interferometric continuous-wave radar system for the contactless measurement of human vital parameters," *Sensors*, vol. 19, no. 11, p. 2492, May 2019.

[13] M. Mercuri, I. R. Lorato, Y.-H. Liu, F. Wieringa, C. V. Hoof, and T. Torfs, "Vital-sign monitoring and spatial tracking of multiple people using a contactless radar-based sensor," *Nature Electronics*, vol. 2, pp. 252–262, Jun. 2019.

[14] M. Alizadeh, G. Shaker, J. C. M. D. Almeida, P. P. Morita, and S. Safavi-Naeini, "Remote monitoring of human vital signs using mm-Wave FMCW radar," *IEEE Access*, vol. 7, pp. 54 958–54 968, 2019.

[15] T. K. V. Dai, K. Oleksak, T. Kvelashvili, F. Foroughian, C. Bauder, P. Theilmann, A. E. Fathy, and O. Kilic, "Enhancement of remote vital sign monitoring detection accuracy using multiple-input multiple-output 77 GHz FMCW radar," *IEEE Journal of Electromagnetics, RF and Microwaves in Medicine and Biology*, vol. 6, no. 1, pp. 111–122, 2022.

[16] M. Kebe, R. Gadhafi, B. Mohammad, M. Sanduleanu, H. Saleh, and M. Al-Qutayri, "Human vital signs detection methods and potential using radars: a review," *Sensors*, vol. 20, p. 1454, March 2020.

[17] D. E. Mohrman and L. J. Heller, *Cardiovascular Physiology*, 9th ed. New York, NY: McGraw-Hill Education, 2018.

[18] N. Herring, D. J. Paterson, and J. Armstrong, *Cardiac electrophysiology: from cell to bedside*. Elsevier, 2021.

[19] R. E. Klabunde, *Cardiovascular physiology concepts*. Lippincott Williams & Wilkins, 2016.

[20] T. J. Hodgetts, G. Kenward, I. G. Vlachonikolis, S. Payne, and N. Castle, "The identification of risk factors for cardiac arrest and formulation of activation criteria to alert a medical emergency team," *Resuscitation*, vol. 54, pp. 125–131, Aug. 2002.

[21] C. Bruser, C. H. Antink, T. Wartzek, M. Walter, and S. Leonhardt, "Ambient and unobtrusive cardiorespiratory monitoring techniques," *IEEE Reviews in Biomedical Engineering*, vol. 8, pp. 30–43, 2015.

[22] A. Davies and A. Scott, "How to record a 12-lead ECG," in *Starting to Read ECGs*. Springer London, Oct. 2013, pp. 1–17.

[23] K. Lee and J. K. Nadel, "Respiratory system," in *Harrison's Principles of Internal Medicine*, 20th ed., J. L. Jameson, Ed. New York: McGraw-Hill Education, 2018.

[24] R. M. Kacmarek, J. K. Stoller, and A. J. Heuer, *Egan's Fundamentals of Respiratory Care*, 11th ed. St. Louis, MO: Elsevier, 2021.

[25] I. J. Brekke, L. H. Puntervoll, P. B. Pedersen, J. Kellett, and M. Brabrand, "The value of vital sign trends in predicting and monitoring clinical deterioration: A systematic review," *PLOS ONE*, vol. 14, no. 1, Jan. 2019.

[26] R. Mejia, J. Ward, T. Lentine, and D. A. Mahler, "Target dyspnea ratings predict expected oxygen consumption as well as target heart rate values," *American Journal of Respiratory and Critical Care Medicine*, vol. 159, pp. 1485–1489, May 1999.

[27] Z. V. Edmonds, W. R. Mower, L. M. Lovato, and R. Lomeli, "The reliability of vital sign measurements," *Annals of Emergency Medicine*, vol. 39, no. 3, pp. 233–237, Mar. 2002.

[28] O. T. Inan, P. F. Migeotte, K. S. Park, M. Etemadi, K. Tavakolian, R. Casanella *et al.*, "Ballistocardiography and seismocardiography: A review of recent advances," *IEEE Journal of Biomedical and Health Informatics*, vol. 19, no. 4, pp. 1414–1427, 2015.

[29] C. Bruser, K. Stadlthanner, S. de Waele, and S. Leonhardt, "Adaptive beat-to-beat heart rate estimation in ballistocardiograms," *IEEE Transactions on Information Technology in Biomedicine*, vol. 15, no. 5, pp. 778–786, 2011.

[30] O. T. Inan, M. Etemadi, R. M. Wiard, L. Giovangrandi, and G. T. A. Kovacs, "Robust ballistocardiogram acquisition for home monitoring," *Physiological Measurement*, vol. 30, no. 2, pp. 169–185, Jan. 2009.

[31] D. Heise, L. Rosales, M. Skubic, and M. J. Devaney, "Refinement and evaluation of a hydraulic bed sensor," in *2011 Annual International Conference of the IEEE Engineering in Medicine and Biology Society*, 2011, pp. 4356–4360.

[32] M. Brink, C. H. Müller, and C. Schierz, "Contact-free measurement of heart rate, respiration rate, and body movements during sleep," *Behavior Research Methods*, vol. 38, no. 3, pp. 511–521, Aug. 2006.

[33] B. H. Choi, G. S. Chung, J.-S. Lee, D.-U. Jeong, and K. S. Park, "Slow-wave sleep estimation on a load-cell-installed bed: a non-constrained method," *Physiological Measurement*, vol. 30, no. 11, pp. 1163–1170, Oct. 2009.

[34] D. M. Salerno, "Seismocardiography: A new technique for recording cardiac vibrations. concept, method, and initial observations," *Journal of cardiovascular technology*, vol. 9, no. 2, pp. 111–118, 1990.

[35] K. Pandia, O. T. Inan, G. T. Kovacs, and L. Giovangrandi, "Extracting respiratory information from seismocardiogram signals acquired on the chest using a miniature accelerometer," *Physiological measurement*, vol. 33, no. 10, p. 1643, 2012.

[36] P. Bifulco, G. Gargiulo, G. D'Angelo, A. Liccardo, M. Romano, F. Clemente *et al.*, "Monitoring of respiration, seismocardiogram and heart sounds by a PVDF piezo film sensor," vol. 11, Sep. 2014, pp. 786–789.

[37] R. S. Crow, P. Hannan, D. Jacobs, L. Hedquist, and D. M. Salerno, "Relationship between seismocardiogram and echocardiogram for events in the cardiac cycle," *American journal of noninvasive cardiology*, vol. 8, pp. 39–46, 1994.

[38] F. Al-Khalidi, R. Saatchi, D. Burke, H. Elphick, and S. Tan, "Respiration rate monitoring methods: A review," *Pediatric Pulmonology*, vol. 46, no. 6, pp. 523–529, Jan. 2011.

[39] M. Chu, T. Nguyen, V. Pandey, Y. Zhou, H. N. Pham, R. B. Yoseph *et al.*, "Respiration rate and volume measurements using wearable strain sensors," *NPJ Digital Medicine*, vol. 2, no. 1, Feb. 2019.

[40] P. Bingger, M. Zens, and P. Woias, "Highly flexible capacitive strain gauge for continuous long-term blood pressure monitoring," *Biomedical Microdevices*, vol. 14, no. 3, pp. 573–581, Feb. 2012.

[41] Y. Shu, C. Li, Z. Wang, W. Mi, Y. Li, and T. L. Ren, "A pressure sensing system for heart rate monitoring with polymer-based pressure sensors and an anti-interference post processing circuit," *Sensors*, vol. 15, no. 2, pp. 3224–3235, Feb. 2015.

[42] M. J. Tobin, "Respiratory monitoring in the intensive care unit," *American Review of Respiratory Disease*, vol. 138, no. 6, pp. 1625–1642, Jan. 1988.

[43] G. K. Prisk, J. Hammer, and C. J. Newth, "Techniques for measurement of thoracoabdominal asynchrony," *Pediatric Pulmonology*, vol. 34, no. 6, pp. 462–472, Jan. 2002.

[44] E. McAdams, A. Krupaviciute, C. Gehin, E. Grenier, B. Massot, A. Dittmar, P. Rubel, and J. Fayn, "Wearable sensor systems: The challenges," in *2011 Annual International Conference of the IEEE Engineering in Medicine and Biology Society*, 2011, pp. 3648–3651.

[45] O. H. Mayer, R. G. Clayton, Sr., A. F. Jawad, J. M. McDonough, and J. L. Allen, "Respiratory inductance plethysmography in healthy 3-to 5-year-old children," *Chest*, vol. 124, no. 5, pp. 1812–1819, 2003.

[46] N. Strömberg and N. Nelson, "Thoracoabdominal asynchrony in small children with lung disease–methodological aspects and the relationship to lung mechanics," *Clinical Physiology*, vol. 18, no. 5, pp. 447–456, 1998.

[47] C. Y. Guo, K. J. Wang, and T. L. Hsieh, "Piezoelectric sensor for the monitoring of arterial pulse wave: Detection of arrhythmia occurring in PAC/PVC patients," *Sensors*, vol. 21, no. 20, p. 6915, Oct. 2021.

[48] A. Allataifeh and M. A. Ahmad, "Simultaneous piezoelectric noninvasive detection of multiple vital signs," *Scientific Reports*, vol. 10, no. 1, Jan. 2020.

[49] K. Konno and J. Mead, "Measurement of the separate volume changes of rib cage and abdomen during breathing," *Journal of Applied Physiology*, vol. 22, no. 3, pp. 407–422, Mar. 1967.

[50] M. A. Sackner, H. Watson, A. S. Belsito, D. Feinerman, M. Suarez, G. Gonzalez, F. Bizousky, and B. Krieger, "Calibration of respiratory inductive plethysmograph

during natural breathing," *Journal of Applied Physiology*, vol. 66, no. 1, pp. 410–420, Jan. 1989.

[51] H. T. Ngo, C. V. Nguyen, T. M. H. Nguyen, and T. V. Vo, "A portable respiratory monitor using respiratory inductive plethysmography," in *IFMBE Proceedings*. Springer Berlin Heidelberg, 2013, pp. 222–225.

[52] J. Haynes, "Basic spirometry testing and interpretation for the primary care provider," *Canadian Journal of Respiratory Therapy*, vol. 54, no. 4, pp. 92–98, Jan. 2018.

[53] R. Pellegrino, G. Viegi, V. Brusasco, R. O. Crapo, F. Burgos, R. Casaburi, A. Coates, C. Van Der Grinten, P. Gustafsson, J. Hankinson *et al.*, "Interpretative strategies for lung function tests," *European respiratory journal*, vol. 26, no. 5, pp. 948–968, 2005.

[54] A. Davies and S. Alwyn, *ECG Basics*. London: Springer London, 2014, pp. 19–33.

[55] S. Okutucu and A. Oto, *Fundamentals of ECG*. Cham: Springer International Publishing, 2018, pp. 1–18.

[56] F. Castells, P. Laguna, L. Sörnmo, A. Bollmann, and J. M. Roig, "Principal component analysis in ECG signal processing," *EURASIP Journal on Advances in Signal Processing*, vol. 2007, no. 1, Feb. 2007.

[57] E. M. Antman, D. T. Anbe, P. W. Armstrong, E. R. Bates, L. A. Green, M. Hand *et al.*, "ACC/AHA guidelines for the management of patients with ST-elevation myocardial infarction—executive summary," *Circulation*, vol. 110, no. 5, pp. 588–636, Aug. 2004.

[58] C. Slucks, "The electrocardiogram in duchenne progressive muscular dystrophy," *Circulation*, vol. 38, no. 5, pp. 933–940, Jan. 1968.

[59] C. C. Hsu, B. S. Lin, K. Y. He, and B. S. Lin, "Design of a wearable 12-lead noncontact electrocardiogram monitoring system," *Sensors*, vol. 19, p. 1509, Mar. 2019.

[60] Y. M. Chi, T.-P. Jung, and G. Cauwenberghs, "Dry-contact and noncontact biopotential electrodes: Methodological review," *IEEE Reviews in Biomedical Engineering*, vol. 3, pp. 106–119, 2010.

[61] K. Arquilla, A. Webb, and A. Anderson, "Textile electrocardiogram (ECG) electrodes for wearable health monitoring," *Sensors*, vol. 20, no. 4, p. 1013, Feb. 2020.

[62] N. Saghir, A. Aggarwal, N. Soneji, V. Valencia, G. Rodgers, and T. Kurian, "A comparison of manual electrocardiographic interval and waveform analysis in lead 1 of 12-lead ECG and apple watch ECG: A validation study," *Cardiovascular Digital Health Journal*, vol. 1, no. 1, pp. 30–36, Jul. 2020.

[63] N. Isakadze and S. S. Martin, "How useful is the smartwatch ECG?" *Trends in Cardiovascular Medicine*, vol. 30, no. 7, pp. 442–448, Jan. 2020.

[64] M. V. Perez, K. W. Mahaffey, H. Hedlin, J. S. Rumsfeld, A. Garcia, T. Ferris *et al.*, "Large-scale assessment of a smartwatch to identify atrial fibrillation," *The New England journal of medicine*, vol. 381, no. 20, pp. 1909–1917, Jan. 2019.

[65] J. Allen, "Photoplethysmography and its application in clinical physiological measurement," *Physiological Measurement*, vol. 28, no. 3, pp. 1–39, Feb. 2007.

[66] M. Ghamari, "A review on wearable photoplethysmography sensors and their potential future applications in health care," *International Journal of Biosensors & Bioelectronics*, vol. 4, no. 4, 2018.

[67] A. Reisner, P. A. Shaltis, D. McCombie, H. H. Asada, D. S. Warner, and M. A. Warner, "Utility of the photoplethysmogram in circulatory monitoring," *Anesthesiology*, vol. 108, no. 5, pp. 950–958, May 2008.

[68] A. A. Alian and K. H. Shelley, "Photoplethysmography," *Best Practice & Research Clinical Anaesthesiology*, vol. 28, no. 4, pp. 395–406, Jan. 2014.

[69] P. H. Charlton, D. A. Birrenkott, T. Bonnici, M. A. F. Pimentel, A. E. W. Johnson, J. Alastruey, L. Tarassenko, P. J. Watkinson, R. Beale, and D. A. Clifton, "Breathing rate estimation from the electrocardiogram and photoplethysmogram: A review," *IEEE Reviews in Biomedical Engineering*, vol. 11, pp. 2–20, 2018.

[70] H. J. Davies, P. Bachtiger, I. Williams, P. L. Molyneaux, N. S. Peters, and D. P. Mandic, "Wearable in-ear PPG: Detailed respiratory variations enable classification of copd," *IEEE Transactions on Biomedical Engineering*, vol. 69, no. 7, pp. 2390–2400, 2022.

[71] F. Shirbani, N. Hui, I. Tan, M. Butlin, and A. P. Avolio, "Effect of ambient lighting and skin tone on estimation of heart rate and pulse transit time from video plethysmography," in *2020 42nd Annual International Conference of the IEEE Engineering in Medicine & Biology Society (EMBC)*, 2020, pp. 2642–2645.

[72] F. Wouters, H. Gruwez, J. Vranken, D. Vanhaen, B. Daelman, L. Ernon *et al.*, "The potential and limitations of mobile health and insertable cardiac monitors in the detection of atrial fibrillation in cryptogenic stroke patients: Preliminary results from the REMOTE trial," *Frontiers in Cardiovascular Medicine*, vol. 9, Apr. 2022.

[73] R. S. Kasbekar and Y. Mendelson, "Evaluation of key design parameters for mitigating motion artefact in the mobile reflectance PPG signal to improve estimation of arterial oxygenation," *Physiological Measurement*, vol. 39, no. 7, Jul. 2018.

[74] M. Nabih-Ali, E.-S. A. El-Dahshan, and A. S. Yahia, "A review of intelligent systems for heart sound signal analysis," *Journal of Medical Engineering & Technology*, vol. 41, no. 7, pp. 553–563, Oct. 2017.

[75] E. F. Banaszak, R. C. Kory, and G. L. Snider, "Phonopneumography," *American Review of Respiratory Disease*, vol. 107, no. 3, pp. 449–455, 1973.

[76] S. Yuenyong, A. Nishihara, W. Kongprawechnon, and K. Tungpimolrut, "A framework for automatic heart sound analysis without segmentation," *Biomedical engineering online*, vol. 10, pp. 1–23, 2011.

[77] H. Pasterkamp, A. Tal, F. Leahy, R. Fenton, V. Chernick, and C. Serette, "The effect of anticholinergic treatment on postexertional wheezing in asthma studied by phonopneumography and spirometry," *American Review of Respiratory Disease*, vol. 132, no. 1, pp. 16–21, 1985.

[78] S. A. Fattah, N. M. Rahman, A. Maksud, S. I. Foysal, R. I. Chowdhury, S. S. Chowdhury *et al.*, "Stetho-phone: Low-cost digital stethoscope for remote personalized healthcare," in *2017 IEEE Global Humanitarian Technology Conference (GHTC)*, 2017, pp. 1–7.

[79] J. Nedoma, M. Fajkus, R. Martinek, S. Kepak, J. Cubik, S. Zabka, and V. Vasinek, "Comparison of bcg, pcg and ecg signals in application of heart rate monitoring of the human body," in *2017 40th International Conference on Telecommunications and Signal Processing (TSP)*. IEEE, 2017, pp. 420–424.

[80] F. Chakir, A. Jilbab, C. Nacir, and A. Hammouch, "Recognition of cardiac abnormalities from synchronized ecg and pcg signals," *Physical and Engineering Sciences in Medicine*, vol. 43, pp. 673–677, 2020.

[81] B. S. Emmanuel, "A review of signal processing techniques for heart sound analysis in clinical diagnosis," *Journal of medical engineering & technology*, vol. 36, no. 6, pp. 303–307, 2012.

[82] M. Johnston, S. P. Collins, and A. B. Storrow, "The third heart sound for diagnosis of acute heart failure," *Current Heart Failure Reports*, vol. 4, no. 3, pp. 164–169, 2007.

[83] J. Liu, Y. Li, and C. Gu, "Chapter 9 - Radar-based vital signs monitoring," in *Contactless Vital Signs Monitoring*, W. Wang and X. Wang, Eds. Academic Press, 2022, pp. 181–203.

[84] V. P. Tran, A. A. Al-Jumaily, and S. M. S. Islam, "Doppler radar-based non-contact health monitoring for obstructive sleep apnea diagnosis: A comprehensive review," *Big Data and Cognitive Computing*, vol. 3, p. 3, Jan. 2019.

[85] Z. Yang, K. Mitsui, J. Wang, T. Saito, S. Shibata, H. Mori, and G. Ueda, "Non-contact heart-rate measurement method using both transmitted wave extraction and wavelet transform," *Sensors*, vol. 21, p. 2735, Apr. 2021.

[86] A. Prat, S. Blanch, A. Aguasca, J. Romeu, and A. Broquetas, "Collimated beam FMCW radar for vital sign patient monitoring," *IEEE Transactions on Antennas and Propagation*, vol. 67, pp. 5073–5080, Aug. 2019.

[87] D. Obeid, G. Zaharia, S. Sadek, and G. E. Zein, "Microwave Doppler radar for heartbeat detection vs electrocardiogram," *Microwave and Optical Technology Letters*, vol. 54, pp. 2610–2617, Nov. 2012.

[88] S. Petruzzelli, A. Palla, and C. Giuntini, "Limitations of ECG in diagnosing pulmonary embolism," *Chest*, vol. 113, no. 2, p. 559, Feb. 1998.

[89] N. Fourikis, "Systems and applications," in *Advanced Array Systems, Applications and RF Technologies*. Elsevier, 2000, pp. 1–110.

[90] M. Parker, "Pulse Doppler radar," in *Digital Signal Processing 101*. Elsevier, 2010, pp. 201–211.

[91] M. Nosrati, S. Shahsavari, and N. Tavassolian, "Multi-target vital-signs monitoring using a dual-beam hybrid Doppler radar," in *2018 IEEE International Microwave Biomedical Conference (IMBioC)*, 2018, pp. 58–60.

[92] M. Nosrati and N. Tavassolian, "Accuracy enhancement of Doppler radar-based heartbeat rate detection using chest-wall acceleration," in *2018 IEEE International Microwave Biomedical Conference (IMBioC)*, 2018, pp. 139–141.

[93] I. V. Mikhelson, S. Bakhtiari, T. W. Elmer, and A. V. Sahakian, "Remote sensing of patterns of cardiac activity on an ambulatory subject using millimeter-wave interferometry and statistical methods," *Medical & Biological Engineering & Computing*, vol. 51, pp. 135–142, Feb. 2013.

[94] J. Yan, H. Hong, H. Zhao, Y. Li, C. Gu, and X. Zhu, "Through-wall multiple targets vital signs tracking based on vmd algorithm," *Sensors*, vol. 16, p. 1293, Aug. 2016.

[95] C. Gu, G. Wang, Y. Li, T. Inoue, and C. Li, "A hybrid radar-camera sensing system with phase compensation for random body movement cancellation in Doppler vital sign detection," *IEEE Transactions on Microwave Theory and Techniques*, vol. 61, pp. 4678–4688, 12 2013.

[96] J. M. Muñoz-Ferreras, Z. Peng, R. Gómez García, and C. Li, "Random body movement mitigation for FMCW-radar-based vital-sign monitoring," in *2016 IEEE Topical Conference on Biomedical Wireless Technologies, Networks, and Sensing Systems (BioWireleSS)*, 2016, pp. 22–24.

[97] J. M. Muñoz-Ferreras and F. Pérez-Martínez, "Subinteger range-bin alignment method for ISAR imaging of noncooperative targets," *EURASIP Journal on Advances in Signal Processing*, vol. 2010, no. 1, p. 438615, May 2010.

[98] M. Sekine and K. Maeno, "Non-contact heart rate detection using periodic variation in Doppler frequency," in *2011 IEEE Sensors Applications Symposium*, 2011, pp. 318–322.

[99] E. Mogi and T. Ohtsuki, "Heartbeat detection with Doppler sensor using adaptive scale factor selection on learning," in *2015 IEEE 26th Annual International Symposium on Personal, Indoor, and Mobile Radio Communications (PIMRC)*, 2015, pp. 2166–2170.

[100] S. Tomii and T. Ohtsuki, "Heartbeat detection by using Doppler radar with wavelet transform based on scale factor learning," in *2015 IEEE International Conference on Communications (ICC)*, 2015, pp. 483–488.

[101] P.-L. Cheng and C.-L. Yang, "Heart rate detection with hilbert vibration decomposition in random body movements based on FMCW radars," *IEEE Microwave and Wireless Technology Letters*, pp. 1–4, 2023.

[102] H. Lee, B. H. Kim, J. K. Park, and J. G. Yook, "A novel vital-sign sensing algorithm for multiple subjects based on 24-GHz FMCW Doppler radar," *Remote Sensing*, vol. 11, no. 10, p. 1237, May 2019.

[103] D. R. Morgan and M. G. Zierdt, "Novel signal processing techniques for Doppler radar cardiopulmonary sensing," *Signal Processing*, vol. 89, no. 1, pp. 45–66, 2009.

[104] M. Arsalan, A. Santra, and C. Will, "Improved contactless heartbeat estimation in FMCW radar via kalman filter tracking," *IEEE Sensors Letters*, vol. 4, no. 5, pp. 1–4, 2020.

[105] S. Bi, J. Zeng, M. Bekbalanova, D. Matthews, and X. Leo Liu, "Contact-based radar measurement of cardiac motion — a position and polarization study," in *2016 IEEE Topical Conference on Biomedical Wireless Technologies, Networks, and Sensing Systems (BioWireleSS)*, 2016, pp. 29–31.

[106] R. R. Fletcher and S. Kulkarni, "Wearable Doppler radar with integrated antenna for patient vital sign monitoring," in *2010 IEEE Radio and Wireless Symposium (RWS)*, 2010, pp. 276–279.

[107] F. K. Wang, Y. R. Chou, Y. C. Chiu, and T. S. Horng, "Chest-worn health monitor based on a bistatic self-injection-locked radar," *IEEE Transactions on Biomedical Engineering*, vol. 62, no. 12, pp. 2931–2940, 2015.

[108] C. McCormack, B. Kehoe, S. J. Hardcastle, N. McCaffrey, A. McCarren, S. Gaine *et al.*, "Pulmonary hypertension and home-based (PHAHB) exercise intervention: protocol for a feasibility study," *BMJ Open*, vol. 11, no. 5, 2021.

[109] Fourth Frontier, "Frontier X2: Smart heart ECG monitor," 2020. [Online]. Available: https://fourthfrontier.com/products/frontier-x

[110] F. Shaffer and J. P. Ginsberg, "An overview of heart rate variability metrics and norms," *Frontiers in public health*, p. 258, 2017.

[111] "Metronome online - free bpm metronome," 2022. [Online]. Available: https://metronome-online.com/

[112] Infineon Technologies, "BGT60TR13C 60 GHz radar sensor datasheet V2.4.6," 2022. [Online]. Available: https://www.infineon.com/dgdl/Infineon-BGT60TR13CDataSheet-DataSheet-v01_00-EN.pdf?fileId=8ac78c8c7d718a49017d94bac88e5d43

[113] Infineon Technologies , "DEMO BGT60TR13C," 2022. [Online]. Available: https://www.infineon.com/cms/en/product/evaluation-boards/demo-bgt60tr13c/

[114] T. J. Rouphael, *Wireless receiver architectures and design*. Academic Press, Oct. 2014.

[115] T. Egel, "Case study 4: Communication systems," in *The System Designer's Guide to VHDL-AMS*. Elsevier, 2003, pp. 703–718.

[116] A. E. Omer, S. Safavi-Naeini, R. Hughson, and G. Shaker, "Blood glucose level monitoring using an FMCW millimeter-wave radar sensor," *Remote Sensing*, vol. 12, p. 385, January 2020.

[117] ANSYS, Inc., "Ansys EDT HFSS 2022 R2," 2022. [Online]. Available: https://www.ansys.com/products/electronics/ansys-hfss

[118] C. Gabriel, "Compilation of the dielectric properties of body tissues at RF and microwave frequencies," Occupational and Environmental Health Directorate, Radiofrequency Radiation Division, Brooks Air Force Base, Texas, USA, Technical Report N.AL/OE-TR-1996-0037, 1996.

[119] I. Acoustics, Speech, and and Signal Processing Society Digital Signal Processing Committee, *Programs for digital signal processing*. New York: IEEE Press, 1979.

[120] Y. Ji, J. Zhang, J. Meng, and X. Zhang, "A new CFAR ship target detection method in SAR imagery," *Acta Oceanologica Sinica*, vol. 29, pp. 12–16, 2010.

[121] B. Wang, W. Shi, and Z. Miao, "Confidence analysis of standard deviational ellipse and its extension into higher dimensional euclidean space," *PLoS one*, vol. 10, no. 3, 2015.

[122] D. W. Layton, "Metabolically consistent breathing rates for use in dose assessments," *Health physics*, vol. 64, no. 1, pp. 22–36, 1993.

[123] V. Kumar, A. Sharma, A. Kumar, M. Ahmad, and G. Gupta, "Interaction of mobile phone waves with tissues of skeletal muscles and bone of human beings," *IOSR Journal of Pharmacy and Biological Sciences*, vol. 1, 01 2012.

[124] A. Fazleen and T. Wilkinson, "Early COPD: current evidence for diagnosis and management," *Therapeutic Advances in Respiratory Disease*, vol. 14, Jan. 2020.

[125] O. H. Mayer, R. G. Clayton, A. F. Jawad, J. M. McDonough, and J. L. Allen, "Respiratory inductance plethysmography in healthy 3- to 5-year-old children," *Chest*, vol. 124, no. 5, pp. 1812–1819, Jan. 2003.

[126] N. O. Strömberg and N. Nelson, "Thoracoabdominal asynchrony in small children with lung disease - methodological aspects and the relationship to lung mechanics," *Clinical Physiology*, vol. 18, no. 5, pp. 447–456, Jan. 1998.

[127] D. Balasubramaniam and D. Nedumaran, "Efficient computation of phonocardiographic signal analysis in digital signal processor based system," *International journal of computer theory and Engineering*, vol. 2, no. 4, 2010.

[128] M. Jankiraman, *FMCW Radar Design*, 1st ed. Artech House, 2018.

[129] D. K. Barton, *Radar Handbook*. McGraw-Hill Education, 2012.

[130] C. Balanis, *Modern Antenna Handbook*. John Wiley & Sons, Incorporated, 2007.

[131] M. I. Skolnik, *Introduction to Radar Systems*. McGraw-Hill, 1980.

[132] E. Cardillo, C. Li, and A. Caddemi, "Vital sign detection and radar self-motion cancellation through clutter identification," *IEEE Transactions on Microwave Theory and Techniques*, vol. 69, no. 3, pp. 1932–1942, 2021.

[133] M. Alizadeh, "Remote vital signs monitoring using a mm-Wave FMCW radar," Master's thesis, University of Waterloo, 2019. [Online]. Available: http://hdl.handle.net/10012/14392

[134] J. Taylor and A. Terzuoli, "On the concept of near field radar cross section," in *IEEE Antennas and Propagation Society International Symposium 1997. Digest*, vol. 2, 1997, pp. 1172–1175.

[135] B. L. V. Kumar, C. B. Pramod, S. Nagendram, and S. Kalyan, "Design and analysis of circular patch antenna," in *Journal of Physics: Conference Series*, vol. 1804, no. 1. IOP Publishing, 2021.

[136] C. Mukta, M. Rahman, and A. Islam, "Design of a compact circular microstrip patch antenna for wlan applications," *International Journal on AdHoc Networking Systems*, vol. 11, no. 3, pp. 01–11, 2021.

[137] S. Abu-Sardanah, A. Gharamohammadi, O. M. Ramahi, and G. Shaker, "A wearable mm-wave radar platform for cardiorespiratory monitoring," *IEEE Sensors Letters*, vol. 7, no. 6, pp. 1–4, 2023.

APPENDICES

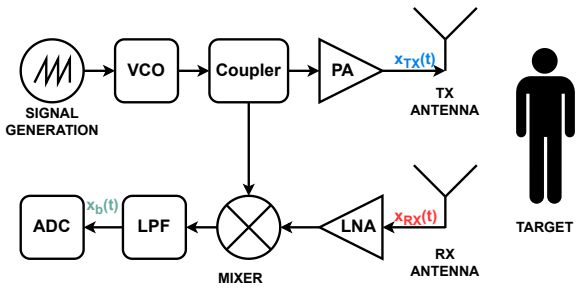
Appendix A

DSP Supporting Materials

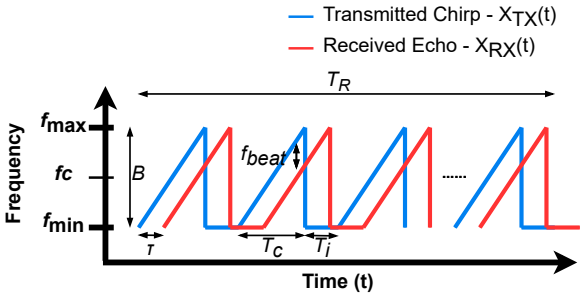
A.1 FMCW radar fundamentals

A.1.1 Radar system overview

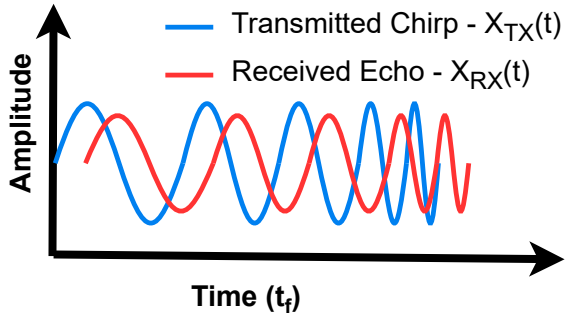
Radars occupy various frequency bands and work by transmitting harmless low-power electromagnetic waves and analyzing their reflections. In particular, FMCW radars are very desirable due to their relatively straightforward architecture, their customizable resolution, and their ability to provide both distance and velocity data. As shown in Figure A.1a, a synthesizer feeds into a VCO to produce a sinusoidal chirp signal where the frequency varies linearly across a frequency bandwidth, B, over a fixed period T_C referred to as the chirp time as in A.1. As highlighted in Figure A.1b, the result is a sawtooth modulation scheme where the slope is defined by the bandwidth and the chirp time as $K = \frac{B}{T_c}$. Note that sampling periods within a single chirp are referred to as the fast time (t_f). The Idle time T_i is to allow the completion of internal system processes and to account for the finite switching time for frequency modulation between chirps. A certain number of chirps is produced within a given frame time (T_R). Note that sampling periods across different chirps in a frame are referred to as the slow time (t_s). The signal is passed through a PA, and transmitted through the TX antenna. As shown in Figure A.1c, the reflection of the transmitted chirp by a stationary object is captured by the RX antenna, and amplified by a LNA before the mixing stage. The received signal is essentially a time-delayed version of the transmitted signal by τ. The difference in frequency between the transmitted and received signals determined at the mixing stage is known as the beat frequency. The beat frequency is sampled by an ADC as it contains desired information about the target.



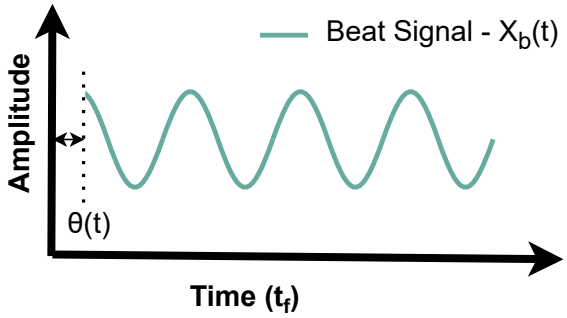
(a) Radar block diagram.



(b) Transmitted and received chirp signals for a stationary target during a single frame.



(c) Single chirp and received echo. Note the time delay and change in amplitude for the received echo.



(d) The resulting beat frequency with a constant frequency and a certain phase shift.

Figure A.1: Radar system and waveform overview.

A.1.2 FMCW radar signal

The instantaneous transmitted frequency varies over time and can be expressed below where f_{min} is the initial chirp frequency of the linear frequency sweep in the range of [f_{min},f_{max}], associated with wavelengths [λ_{max},λ_{min},], B is the bandwidth, and T_C is the chirp duration, and t_f is the fast time:

$$f_t = f_{min} + \frac{B}{T_C} t_f, \quad 0 < t_f < T_c \tag{A.1}$$

The corresponding phase associated with the signal above is represented as:

$$\alpha = 2\pi \int_0^{t_f} f_t dt = 2\pi \left(f_{min} t_f + \frac{B}{2T_C} t_f^2 \right), \quad 0 < t_f < T_c \tag{A.2}$$

As such, a single transmitted chirp signal in a frame as a function of the fast time has the general time domain signal as in A.3, where A_{TX} is the transmitted signal amplitude, K is the chirp slope. The variable ϕ_n is the phase noise of the sawtooth signal generator [128]:

$$\begin{aligned} x_{TX}(t_f) &= A_{TX} \cos \left[2\pi \left(f_{min} + \frac{B}{2T_C} t_f \right) t_f + \phi_n(t_f) \right] \\ &= A_{TX} \cos \left[2\pi \left(f_{min} + \frac{K}{2} t_f \right) t_f + \phi_n(t_f) \right] \\ &= A_{TX} \cos \left[\beta_{TX} \right], \quad 0 < t_f < T_c \end{aligned} \tag{A.3}$$

The chirp signal is transmitted periodically across a frame as mentioned in the previous section, for a duration of T_R, at a period of t_s. Operating under the assumption that thermal noise and other RF imperfections are negligible, the received echo signal can be represented as a delayed version of the transmitted signal as shown in A.4, where $\tau(t_s)$ is the time delay of the chirps within a frame and A_{RX} is the amplitude of the reflected signal:

$$\begin{aligned} x_{RX}(t_f, t_s) &= A_{RX} \cos \left[2\pi \left(f_{min} + \frac{K}{2} (t_f - \tau(t_s)) \right) (t_f - \tau(t_s)) + \phi_n(t_f - \tau(t_s)) \right] \\ &= A_{RX} \cos \left[2\pi f_{min} (t_f - \tau(t_s)) + \pi K (t_f - \tau(t_s))^2 + \phi_n(t_f, t_s) \right] \\ &= A_{RX} \cos \left[\beta_{RX} \right], \quad \tau < t_f < T_c \end{aligned} \tag{A.4}$$

The target, in this case, the human chest exists at a distance R_0 from the radar. It is vibrating due to respiration and heartbeat with a displacement of $\Delta d(t)$. A fraction of the

incident chirp signal is either absorbed or scattered while the remainder is reflected by the target. As a result of the round trip distance $2R_0$ and the propagation of the signal at the speed of light c, the reflected signal has a time delay which can be expressed as:

$$\tau(t_s) = \frac{2(R_0 + \Delta d(t_s))}{c} \tag{A.5}$$

The delayed reflected chirp is mixed with the transmitted chirp resulting in the approximated beat signal. High-frequency components like the ones in A.6 are typically filtered before the beat frequency can be sampled. Moreover, the third phase term in A.7, is mathematically insignificant and is considered negligible in the final expression, as $\tau(t_s)$ is on the order of 1^{-9} s while K is on the order of 1^{13} Hz/s. The final expression described in A.8 is the beat signal at the IF for each radar receiver, denoted by x_{beat}. The system phase noise into a single variable — the total phase noise, ϕ_T.

$$\begin{aligned}
x_{beat}(t_f, t_s) &= x_{TX}(t_f) \cdot x_{RX}(t_f, t_s) \\
&= A_{TX} \cos\left[\beta_{TX}\right] \cdot A_{RX} \cos\left[\beta_{RX}\right] \\
&= A_{TX} A_{RX} \left(\cos\left[\beta_{TX} - \beta_{RX}\right] + \cos\left[\beta_{TX} + \beta_{RX}\right]\right) \qquad \text{(A.6)} \\
&\Rightarrow A_{TX} A_{RX} \cos\left[\beta_{TX} - \beta_{RX}\right] \\
&= A_{TX} A_{RX} \cos\left[2\pi f_{min}\tau(t_s) - 2\pi K\tau(t_s)t_f + \pi K {t_d}^2 + \phi_T(t_f, t_s)\right] \qquad \text{(A.7)} \\
&\approx A_{TX} A_{RX} \cos\left[2\pi f_{min}\tau(t_s) + 2\pi K\tau(t_s)t_f + \phi_T(t_f, t_s)\right] \\
x_{beat}(t_f, t_s) &\approx A_{TX} A_{RX} \cos\left[\theta(t_s) + \omega(t_s)t_f + \phi_T(t_f, t_s)\right], \quad \tau < t_f < T_c \qquad \text{(A.8)}
\end{aligned}$$

Chest vibrations due to respiration and heartbeat are too small in amplitude to be detected as a change in the range bin, instead, they are embedded in the phase change over different frames ($\theta_1(t_s)$), as in A.9, at the target range bin as determined by the radial beat frequency (ω_{beat}) in A.10. In this expression, the vibration displacement is considered negligible compared to the distance of the target in the fast time, and as such the former is dropped from the expression for simplicity. From the expression for θ_1 in A.9, it can be observed that the smaller the wavelength the more sensitive the signal is to smaller vibrations, as is the case for chest vibrations during the heartbeat and respiration, which indicates that the use of mm-Wave radars is ideal for such applications.

$$\theta(t_s) = 2\pi f_{min}\tau(t_s) = 4\pi \frac{R_0 + \Delta d(t_s)}{\lambda_{max}}$$

$$\therefore \theta_0 = 4\pi \frac{R_0}{\lambda_{max}}, \quad \theta_1(t_s) = 4\pi \frac{\Delta d(t_s)}{\lambda_{max}} \tag{A.9}$$

$$\omega_{beat}(t_s) = 2\pi K \tau(t_s) \approx 4\pi \frac{K R_0}{c} = 2\pi f_{beat} \tag{A.10}$$

Therefore, we can represent the expression in A.8 in terms of f_{beat}, phase components θ_0 and θ_1 due to the chest vibrations, and ϕ_T as described in A.11:

$$\begin{aligned} x_{beat}(t_f, t_s) &\approx A_{TX} A_{RX} \cos\left[\theta_0 + \theta_1(t_s) + \omega_{beat} t_f + \phi_T(t_f, t_s)\right] \\ x_{beat}(t_f, t_s) &\approx A_{TX} A_{RX} \cos\left[4\pi \frac{R_0}{\lambda_{max}} + 4\pi \frac{\Delta d(t_s)}{\lambda_{max}} + 2\pi f_{beat} t_f + \phi_T(t_f, t_s)\right], \quad \tau < t_f < T_c \end{aligned} \tag{A.11}$$

From these expressions, we can also deduce metrics relevant to this investigation. To resolve two targets in frequency, the frequency difference must be greater than the reciprocal of the measurement window, which in our case is the duration for a single chirp as in A.12. This indicates that a larger bandwidth yields finer resolution, as described by the relationship in A.13. It is worth noting that bandwidth is typically limited by the hardware used in the FMCW radar system.

$$\Delta f_{beat_{min}} > \frac{1}{T_c} \tag{A.12}$$

$$\begin{aligned} \frac{2K R_{0_{min}}}{c} &> \frac{1}{T_c} \\ R_{0_{min}} &> \frac{c}{2T_c K} \\ R_{0_{min}} &> \frac{c}{2B} \end{aligned} \tag{A.13}$$

Another relevant metric to the set up in this investigation is the maximum range (i.e., the maximum detectable beat frequency). The maximum range is limited by the sampling rate as described in A.14. This is also a limitation set by the radar hardware and can be manipulated by adjusting the number of samples in a single chirp throughout the sampling

window as shown in A.15.

$$\begin{aligned} \Delta f_{beat_{max}} &= \frac{2KR_{0_{max}}}{c} \\ f_S &= \frac{2KR_{0_{max}}}{c} \qquad \text{(A.14)} \\ R_{0_{max}} &= f_S \cdot \frac{c}{2K} \\ R_{0_{max}} &= \frac{\text{Samples per chirp}}{T_c} \cdot \frac{c}{2K} \qquad \text{(A.15)} \end{aligned}$$

The method for capturing the cardiac and respiratory rates and displacement waveforms described in this thesis is displacement-based. As such it is crucial to keep in mind the relationships in A.13 and A.15 when designing the FMCW signal for VS detection.

A.1.3 Radar equation and received signal

The radar equation is a mathematical formula used to describe the performance of a radar system. It relates the transmitted power, the received power, the distance to the target, and various system parameters. The equation is given as shown in A.16 [129, 130]:

$$P_r = P_t G_t G_r \sigma \frac{\lambda^2}{(4\pi)^3 R^4} \frac{1}{L} \qquad \text{(A.16)}$$

where:

- P_r is the received power (in watts)
- P_t is the transmitted power (in watts)
- G_t is the transmitting antenna gain (dimensionless)
- G_r is the receiving antenna gain (dimensionless)
- λ is the wavelength of the radar signal (in meters)
- σ is the radar cross-section (RCS) of the target (in squared meters)
- R is the range to the target (in meters)
- L is the system losses (dimensionless)

Each component of the radar equation plays a distinct role in determining the received power at the radar system [129]. The transmitted power, denoted as P_t, represents the amount of power emitted by the radar system and is a measure of the electrical power converted into radiated power by the transmitting antenna, which is characterized by its gain, denoted as G_t. Similarly, the receiving antenna gain, denoted as G_r, is a measure of how effectively the received signal is converted into electrical power. The antenna gains are crucial components of the radar equation, representing the ability of the transmitting and receiving antennas to convert electrical power into radiated power and collected signal, respectively [130]. The transmitting antenna gain, G_t, measures how effectively the antenna focuses the transmitted power into a beam in the desired direction, while the receiving antenna gain, G_r, measures how effectively the antenna collects the received signal from the desired direction. Both antenna gains depend on the physical characteristics of the antenna, such as its size, shape, and radiation pattern, as well as its operating frequency. The design and optimization of antenna systems is an important aspect of radar engineering that directly impacts the performance of the radar system, such as its range, resolution, and detection capability. The radar cross-section (σ) is a fundamental measure of the target's ability to scatter electromagnetic energy back to the radar[131]. It is influenced by the target's size, shape, and material properties, with larger and more reflective targets exhibiting higher RCS values. The system losses, denoted as L, encompass various sources of energy loss within the radar system, such as cable losses, atmospheric attenuation, and losses in the radar components. Therefore, the received power at the radar system is determined by the interplay of these components, with the RCS of the target providing a critical measure of the target's visibility to the radar system.

The radar equation as presented in A.16 is valid when the target is in the far field region [134]. As will become apparent in upcoming chapters, the FMCW radar system used in this thesis operates at 60 GHz (i.e., $\lambda \approx 5$ mm), with one TX and three RX patch antennas that are 0.98 mm $\times$ 1.95 mm placed 5 mm away from the body. As the dimensions of the antennas are smaller than $\frac{\lambda}{2}$, the antennas are considered electrically small. The far-field and near-field region boundaries are measured in terms of the distance (r) from the radiating source to the wavelength (λ) of the radiation for electrically small antennas as described in A.17 [130]. The summary of the setup indicates that the system operates in the transition region, which is considered to be the farthest point in the near-field region, commonly known as the radiative near field or Fresnel region. The energy in the radiative near field is described as being completely radiant energy (as opposed to reactive in the near-field region), and while the magnetic and electric components of the radiation are more predictable, they do not have quite the same behaviour as they would in the far-field. As such, although the relationship in A.16 is considered valid, the

investigation of system behaviour through full-wave electromagnetic simulation under the described operating parameters is required to understand any loading on the antennas or attenuation to the propagating signal.

$$\begin{aligned} r \ll \lambda &: \text{near} - \text{field region} \\ \lambda \leq r \leq 2\lambda &: \text{transition region} \\ r \gg \lambda &: \text{far} - \text{field region} \end{aligned} \tag{A.17}$$

The radar equation is a crucial tool in the design and analysis of radar systems. It provides insight into the factors that affect the performance of a radar system and can be used to optimize the system parameters for a particular application. An understanding of the maximum range of a target with a certain RCS can be gained by considering the limitations imposed by the specific radar system, including the design and operating parameters of the antenna, the required signal-to-noise ratio at the baseband ($SNR_{BB,\ min}$), as well as the path loss characteristics of the environment.

A.2 Proof of arctangent modulation sensitivity

The sensitivity of arctangent demodulation can be mathematically derived by analyzing the behavior of the arctangent function. Let's consider a simplified scenario where we have a sinusoidal input signal with a small phase variation and examine the response of the arctangent function to this variation.

Assuming the input signal is given by:

$$x(t) = A \cdot \sin(\omega t + \varphi)$$

where A represents the amplitude, ω is the angular frequency, t is time, and φ is the initial phase. Now, let's calculate the derivative of the arctangent function with respect to the phase φ:

$$\frac{d}{d\varphi}[\arctan(x)] = \frac{d}{d\varphi}[\arctan(A \cdot \sin(\omega t + \varphi))]$$

Using the chain rule, we have:

$$\frac{d}{d\varphi}[\arctan(x)] = \frac{1}{1 + x^2} \cdot \frac{d}{d\varphi}[A \cdot \sin(\omega t + \varphi)]$$

and therefore, we can simplify the expression further:

$$\frac{d}{d\varphi}[\arctan(x)] = \frac{1}{1+x^2} \cdot A \cdot \cos(\omega t - \varphi) \tag{A.18}$$

From the above equation, we observe that the derivative of the arctangent function is proportional to the cosine of the phase difference ($\omega t - \varphi$). This indicates that the sensitivity of the arctangent function to changes in phase is proportional to the magnitude of the cosine term. In other words, when the phase variation is small, the cosine term approaches 1, resulting in a higher sensitivity of arctangent demodulation. Conversely, when the phase variation is large, the cosine term approaches 0, leading to reduced sensitivity.

This mathematical analysis demonstrates the sensitivity of arctangent demodulation to small phase changes, which is why it is often employed in radar-based vital sign detection to capture subtle variations in vital signs.

A.3 Commented signal processing algorithm

```
%% Script options
PLOT_FX = 1;

% Use only one at a time. Can use to visualize effect of respiratory
% signal on cardiac signal.
BR_FILT_EN = 0; % 0 = OFF, 1 = ON
HR_FILT_EN = 1; % 0 = OFF, 1 = ON

% Synchronization variables
FX_start = '9:43:09.0000';
radar_start = '09:43:12.995088';

% Time delay for FX
time_shift_fx = -3.9951;

% File locations
directory = '/Users/serene/Desktop/data';
cd(directory)
filename = 'RR_0_HR_FX_AG_Chest_Left_Belt';
```

```
%% Get FX data
if PLOT_FX == 1
    cd(['ecg/' filename]);
    temp = readmatrix([filename '.csv']);
    temp2 = readmatrix('devicedd.csv');

    FX_VS(:,1) = temp2(:,1)/1000,22;
    FX_VS(:,2) = temp2(:,4), 22;
    FX_VS(:,3) = temp2(:,11),22;

    Fs_ecg = 125;  % ECG sampling rate

    temp(:,2) = temp(:,2)/1000;
    ecg = temp;

    [pks,locs,w,p] = findpeaks(ecg(:,2), 'WidthReference','halfheight', ...
                     'MinPeakProminence', 0.05);

    X = [p,w];
    idx = dbscan(X,0.1,9,'Distance','squaredeuclidean');
    k = 1;

    for i = 1:1:size(pks,1)
        % Extract Q
        if idx(i) == 2
            pks_q(k,1) = ecg(locs(i),1);
            pks_q(k,2) = pks(i);
            k = k + 1;
        end
    end

    % Plot the ECG peak clusters
    figure;
    gscatter(X(:,1),X(:,2),idx);
    xlim([0 max(p)]);
    ylim([0 max(w)]);
    xlabel('Promenince (mV)','FontSize', 20);
    ylabel('Width (ms)','FontSize', 20);
```

```
    cd(directory);
end

%% Initialization and variable definitions
% Radar data location
cd('radar');
load([filename '.mat']);

Fs=1000000;% Sampling rate
Fr=20; %Radar frame rate (FPS)
range_res = 0.03; % meter
range_max = 0.96; % meter
lambda = 299792458 / 60750000000; % wavelength = c/f

% Take 1 chirp only
DATA = squeeze(DATA(:,:,10,:));
sample = DATA;

numFrames = size(sample,1);
numRx = size(sample,2);
numSamples = size(sample,3);
data_RX = 3;
time = (0:1:numFrames-1)/Fr;

if PLOT_FX == 1
    window_size = diff(FX_VS(:,1));
else
    window_size = ones(10,1)*40;
end

for n = 1:1:numRx
    %% Determine target range bin
    % Clutter Removal
    sample1 = sample - mean(sample, 1);

    %Use one RX only
    sample1 = squeeze(sample1(:,n,:));
```

```
% Apply FFT on all samples in a frame
NFFT = 2^nextpow2(numSamples);
bins = 0:1:NFFT/2;
P2 = fft(sample1,NFFT,2)/numSamples;
P1 = abs(P2(:,1:NFFT/2+1));
P1(:,2:end-1) = 2*P1(:,2:end-1);

% Determine subject range
bin_max = zeros(numFrames,2);
[bin_max(:,1), bin_max(:,2)] = max(P1,[],2);
[count, bin_value] = groupcounts(bin_max(:,2));
[~,I] = max(count);
target_range_bin(n) = bin_value(I);
fprintf(['Target range: ' num2str((target_range_bin(n)-1)*range_res)...
    ' to ' num2str((target_range_bin(n))*range_res) ' meters for RX'...
    num2str(n) '.\n']);

%% Vibration detection
P1 = P2(:,1:NFFT/2+1);
% Get samples from target bin
vib_bin(n,:) = squeeze(P1(:,target_range_bin(n)));

% Get phase data, upsample, unwrap and downsample
vib_phase(n,:) = angle(vib_bin(n,:));
temp = interp(vib_phase(n,:),2);
vib_phase_unwrapped(n,:) = resample(unwrap(temp),1,2);
vib_phase_unwrapped(n,:) = vib_phase_unwrapped(n,:)

%transform to displacement
displacement(n,:) = (lambda/(4*pi))*vib_phase_unwrapped(n,:)*1000;


%% Filtering
if (BR_FILT_EN == 1) % 0 = OFF, 1 = ON
    displacement_filt(n,:) = filter(FilterBR, 1, displacement(n,:));
elseif (HR_FILT_EN == 1) % 0 = OFF, 1 = ON
    displacement_filt(n,:) = filter(FilterHR2_phaseinterp, 1, ...
```

```
        displacement(n,:));
else
    displacement_filt(n,:) = displacement(n,:);
end

% Rate for entire sample
NFFT = 2^nextpow2(numFrames);
frequency_bins = linspace(0, Fr/2, NFFT/2+1)  * 60;

sig_vs(n,:) = displacement_filt(n,:);

% Rate for entire sample
P2 = abs(fft(sig_vs(n,:), NFFT)/numFrames);
P1 = P2(:,1:NFFT/2+1);
P1(:,2:end-1) = 2*P1(:,2:end-1);
[M,I] = max(10*log10(P1));

% PLot frequency bins
figure;
plot(frequency_bins,10*log10(P1),'r-','LineWidth',2);
hold on
plot(frequency_bins(I),M,'bx')
xlabel('VS Rate (BPM)','FontSize', 20);
ylabel('Magnitude(dB)','FontSize', 20);
xlim([0 100]);


% Determine rate
HR = I;
rate(n) = (HR-1) * (Fr / NFFT) * 60;

% Rate for sliding 20-s window of sample
window_s = 1;
window_e = window_s + window_size(1)*Fr - 1;

for i = 1:size(window_size,1)
    time_VS(i) = time(window_s);
```

```
        sig_hr_seg = displacement_filt(n, window_s:window_e);
        NFFT = 2^nextpow2(length(sig_hr_seg));
        P2 = abs(fft(sig_hr_seg, NFFT)/length(sig_hr_seg));
        P1 = P2(:,1:NFFT/2+1);
        P1(:,2:end-1) = 2*P1(:,2:end-1);
        [~,K(i)] = max(10*log10(P1));

        window_s = window_e + 1;
        if i ~= size(window_size,1)
            window_e = window_e + window_size(i+1)*Fr;
            if window_e < size(time,2);
                time_VS(i+1) = time(window_e);
            else
                window_e = length(sig_vs(n,:));
                time_VS(i+1) = time(end);
                break;
            end
        end
    end
    frequency_bins = linspace(0, Fr/2, NFFT/2+1)  * 60;
    rad_VS(n,:) = frequency_bins(K);

end

% Average all 3 RX channels
displacement_filt(4,:) = mean(displacement_filt(1:3,:),1);
```

Appendix B

PoE 60-GHz FMCW System

B.1 System layout

The custom PoE system is composed of four main components:

- The BGT60T13RC radar module: This radar module was used throughout this thesis, albeit in conjunction with a different MCU (Infenion's MCU7).
- The XMC4400 MCU: This is the central processing unit responsible for the regulation of serial peripheral interface (SPI) communication with the radar for configuration of radar parameters, as well as the transmission control protocol (TCP) communication standard for transmitting raw radar data over LAN.
- The PoE module: The system uses the Ag9712 modules by Silvertel to extract power from a conventional unshielded twisted pair (UTP) Category-5 (CAT-5) Ethernet cable, conforming to the IEEE 802.3af PoE standard.
- Ethernet transceiver: The system uses the KSZ8081RNA which employs the 10BASE-T/100BASE-TX Ethernet physical-layer transceiver for transmission and reception of data over standard UTP CAT-5 cable. In summary, this chip supports data transfer rates of both 10Mbps and 100Mbps.

See Figure B.1, which outlines these different blocks, their power supplies, and the communication protocols between them. Moreover, see the rendered image of the PCB in Figure B.2.

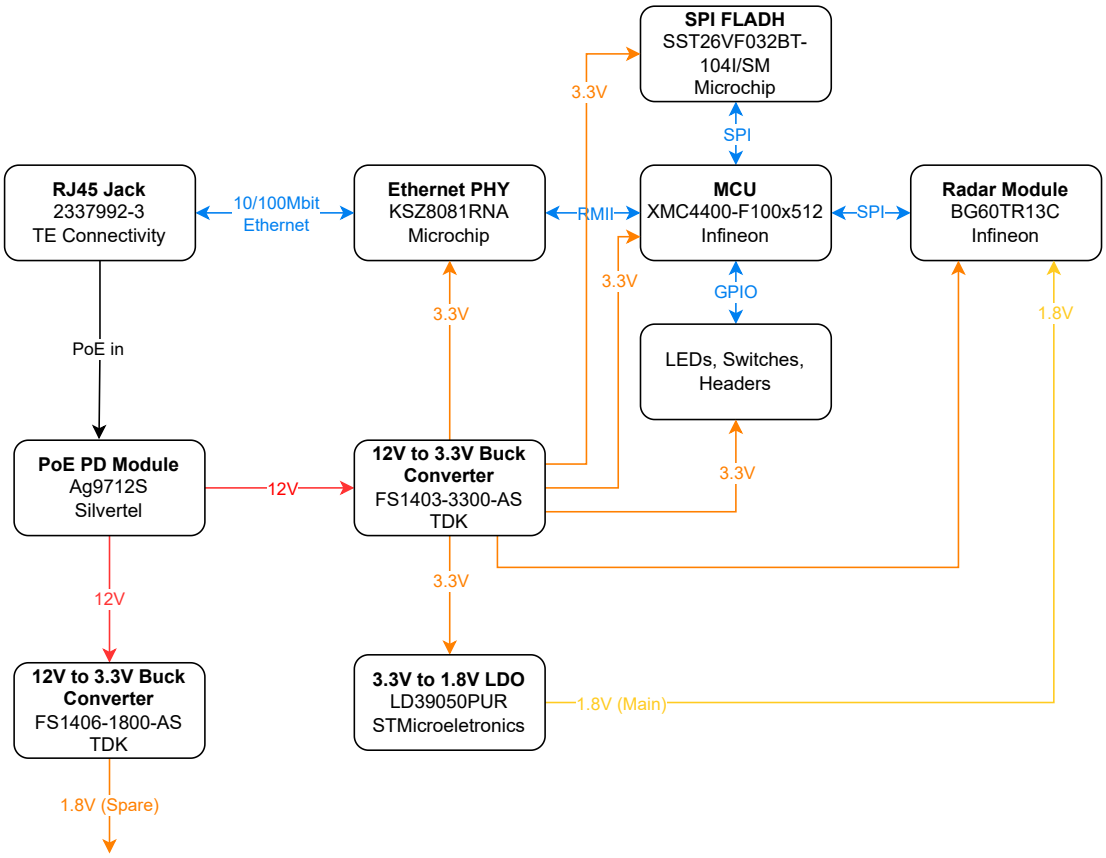
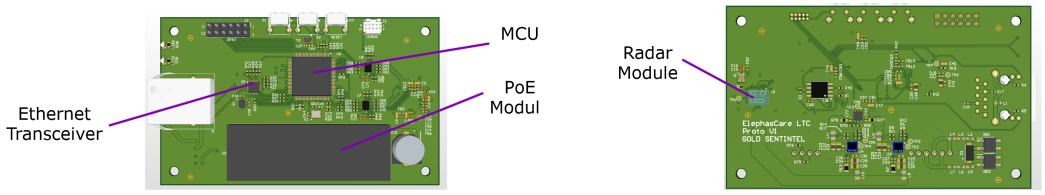


Figure B.1: System layout for high-speed radar system highlighting signals between different chips as well as power up voltages.



(a) Top view.

(b) Bottom view.

Figure B.2: PoE radar custom PCB top and bottom view.

B.2 System firmware flowchart

The bring-up for this system has been completed and the firmware is currently in progress. The general firmware routine begins at device power-up by setting up the SPI protocol between the radar module and MCU. The next step involves setting up the TCP communication protocol between the PoE system,(i.e., the client), specifically the XMC4400 chip, and a local PC (i.e., the server). The client requests the radar set-up parameters from the server. The server sends over the necessary setup parameters to the MCU to facilitate the set-up of the radar chirp signal. Once the radar and peripheral communication protocols are set up, an interrupt is specified to indicate that a radar frame has been received. The main part of the firmware can now be executed, where 12-bit radar samples are acquired from the ADC, and once an entire frame has been sampled, the interrupt is triggered allowing the formatting of the data packet to be sent to the server and checking the validity of the TCP connection. If the connection is valid, the packet is sent and if not, the connection is re-initialized and then the packet is sent. A visual summary of this process can be observed in Fig

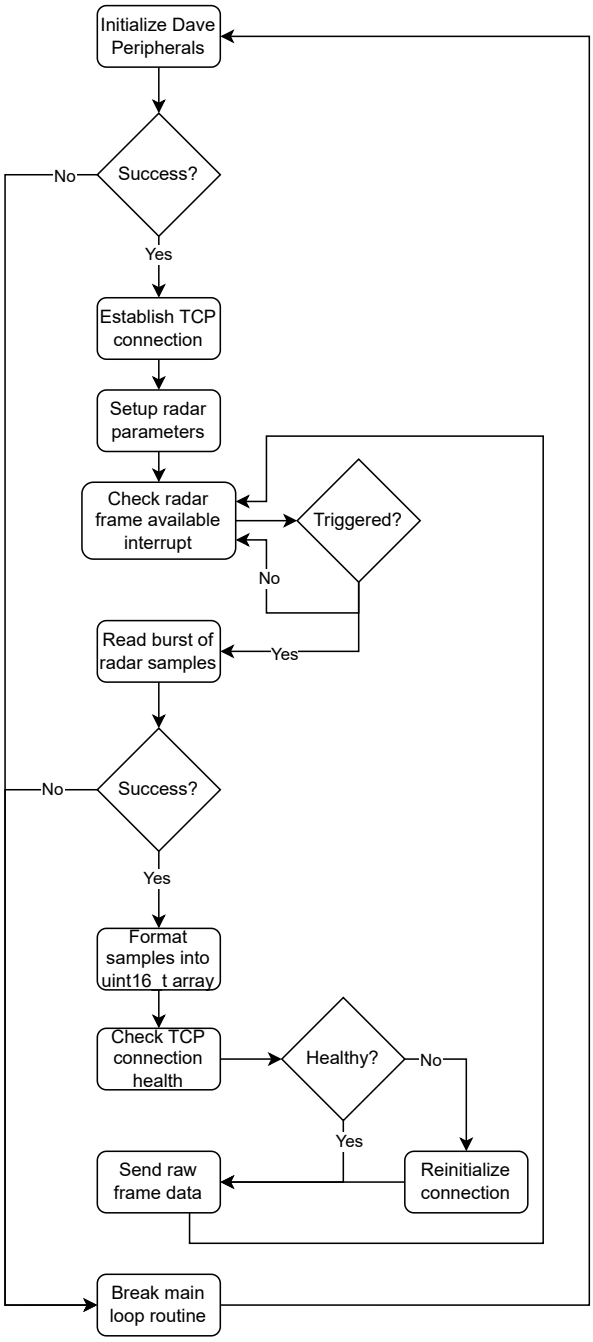


Figure B.3: Firmware flowchart for PoE radar.

Appendix C

2.5 GHz FMCW Radar

C.1 System layout

The system uses a Raspberry Pi to interact with the proposed RF front end PCB. The Raspberry Pi module contains many helpful features to facilitate the straightforward design of the system. The proposed RF front-end system design can be seen in Figure C.1. The design will interface with the Raspberry Pi through the SPI protocol for signal generation and an SPI-compatible ADC for radar IF signal detection. A summary of the components and ICs used for the system is shown in Figure C.2, and some brief information regarding their functionality can be seen in Table C.2. This system is currently under fabrication, therefore, bring-up and firmware activities are underway.

Signal generation: AD9837

The system requires the generation of a triangular voltage signal in the range of 1.25–2.25 V to drive the frequency generation using the VCO. The triangular signal generated by the IC has is conditioned through an op-amp circuit to transform the signal to the desired range. The AD9837 IC by analog devices was chosen mainly due to its low-power consumption as well as its easily customizable features. Moreover, since this signal generator IC can use a supply voltage range of 2.3–5.5 V, it is compatible with both voltages provided by the Raspberry Pi. The IC uses a standard 3-wire SPI interface, which allows it to interface directly with the Raspberry Pi module used. The signal generator uses an external serial clock to write the data, as well as control information flow into the device.

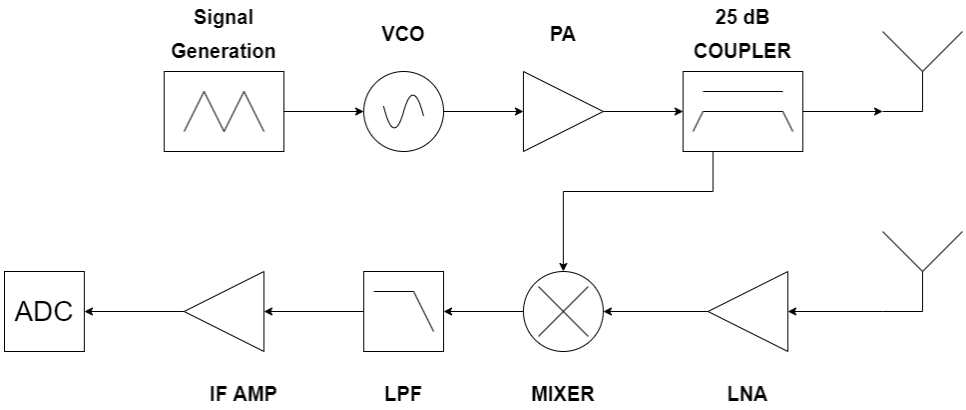
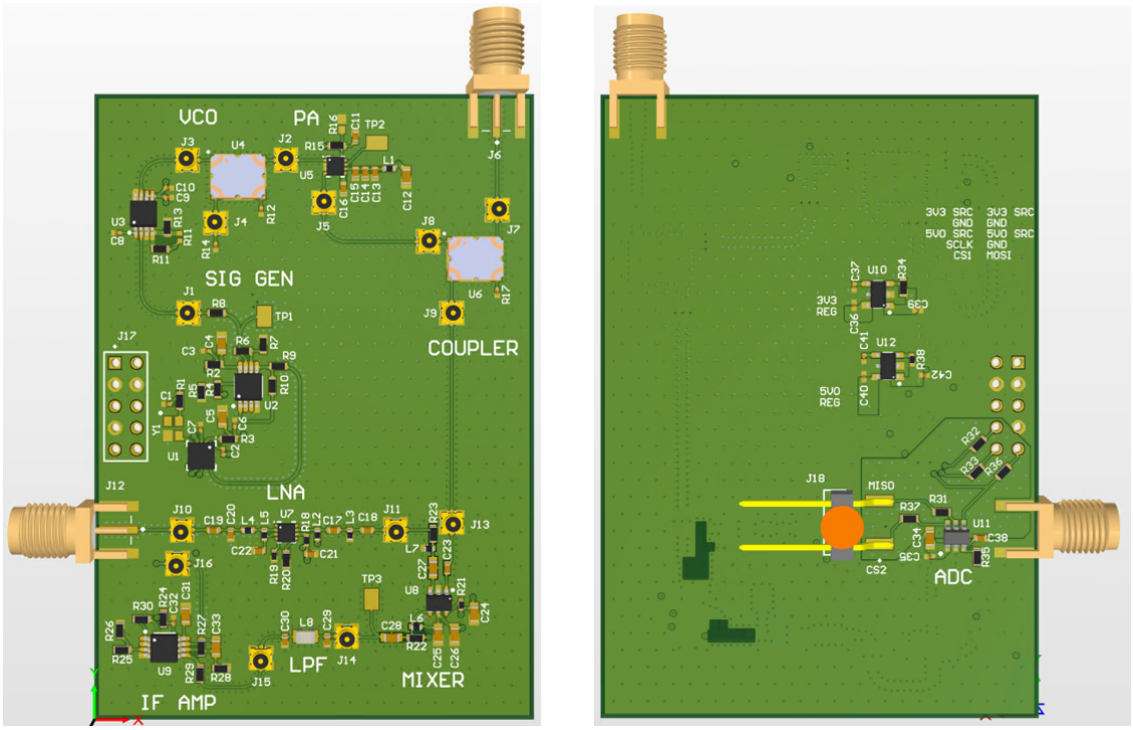


Figure C.1: RF front end system diagram.



(a) Top view.

(b) Bottom view.

Figure C.2: Low-frequency radar custom PCB top and bottom view.

The layout recommended in the datasheet was implemented, including considerations regarding analog and digital signal considerations. Moreover, supply bypassing capacitors were used (0.1 μF in parallel to 10 μF), placed as close as possible to the device for optimal performance.

VCO: MAX2750

This triangular signal in the range of 1.25–2.25 V is fed into the VCO to produce an FMCW signal with a bandwidth of 2.45–2.55 GHz. The rising and falling slope is determined by the generated triangular waveform. The VCO output has an amplifier buffered stage that is matched to 50 Ω internally. This helps with maximizing output power and isolating the VCO from load impedance variations. This IC operates over a supply voltage range of 2.7–5.5 V, which is compatible with voltages provided by the Raspberry Pi. The supply voltage of 3.3 V was chosen for VCO operation, based on the tuning voltage graphs in the data sheet. The IC has internal supply voltage regulation, thus eliminating the need for an external LDO regulator. The IC also provides a digitally controlled shutdown mode for power-supply management. In shutdown, the supply current is reduced to less than 1μA. The output RF power for this IC is −3.0 dBm.

PA: SE2574BL-R

This power amplifier is designed in compliance with IEEE 802.11b/g/n applications, and designed for functionality at 2.5 GHz. The input and output RF ports are internally matched to 50 Ω. The RF ports are also DC-decoupled which eliminates the need for any DC-blocking capacitors or matching components, which is essential in reducing the system board's bill of materials cost and layout size. This PA typically has a 28 dB gain, has excellent linearity, and comes in a small DFN package. It includes a power detector voltage output, that is temperature-stable and VSWR insensitive. Decoupling capacitors were used on the power trace for this component as well.

25-dB coupler: X3C19P2-30S

Based on the output VCO power (−3.0 dBm) and the PA gain (28 dBm; i.e., power is 25 dBm just before the coupler), and the required mixer LO input power (max 0 dBm), a 25–dB 90° coupler was selected. This particular component was selected due to its small

footprint. The performance of the coupler was simulated on ADS using the manufacturer-provided s-parameter file on an FR-4 substrate ($\varepsilon_r = 4.7$) with a thickness of 1.6 mm and a loss tangent ($tan\delta$) of 0.001 to confirm the desired behaviour as shown in Figure C.3.

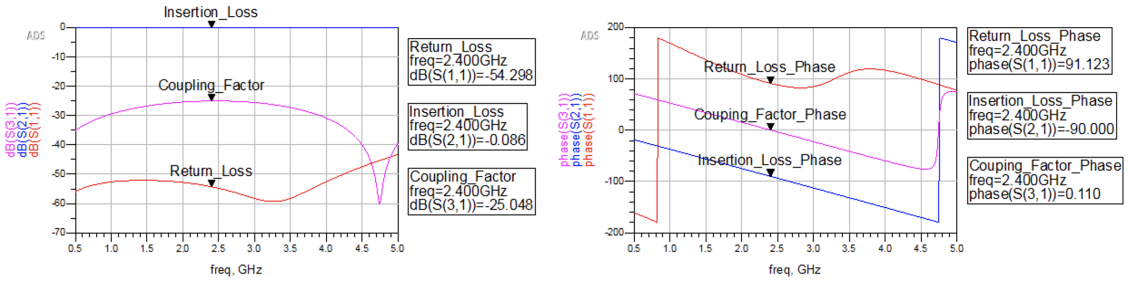


Figure C.3: Magnitude (left) and phase (right) of 25-dB coupler

Antenna

The antenna designed for this near-field application is a circular patch antenna with a circular cutout and a square ground plane cutout. This patch antenna with flexible polyimide substrate was used due to its compact size, low profile, cheap manufacturing costs, straightforward design, and a particularly desirable highly directive radiation pattern that is important for this application[130]. Adding a cutout was proposed by many to encourage wide-band performance in a patch antenna [135]. The addition of a cutout in the ground plane was discussed by Mukta *et. al* [136]. Figure C.4 shows the antenna design, with the parameters for size are shown in Table C.1. The antenna was designed with an input impedance of 50 Ω.

Table C.1: Summary of antenna parameter values.

Parameter	**Value (mm)**
Microstrip line width	0.361
Patch radius	22.2
Patch cutout radius	16.0
Ground plane cutout	44.5

The antenna was simulated using HFSS with a layer of skin or muscle at a distance of 1 cm away and a thickness sweep between 0.5λ–1.0λ to examine behaviour, in particular

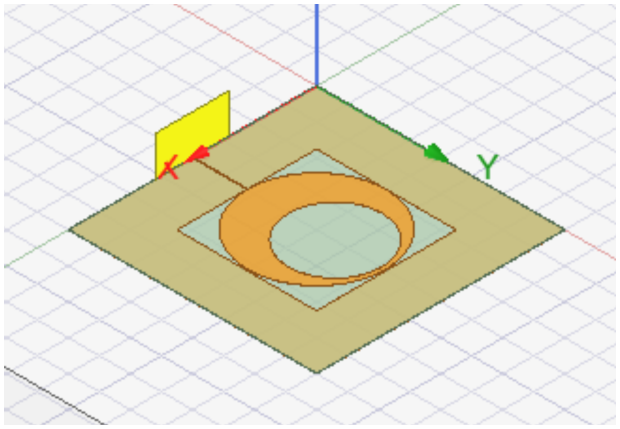


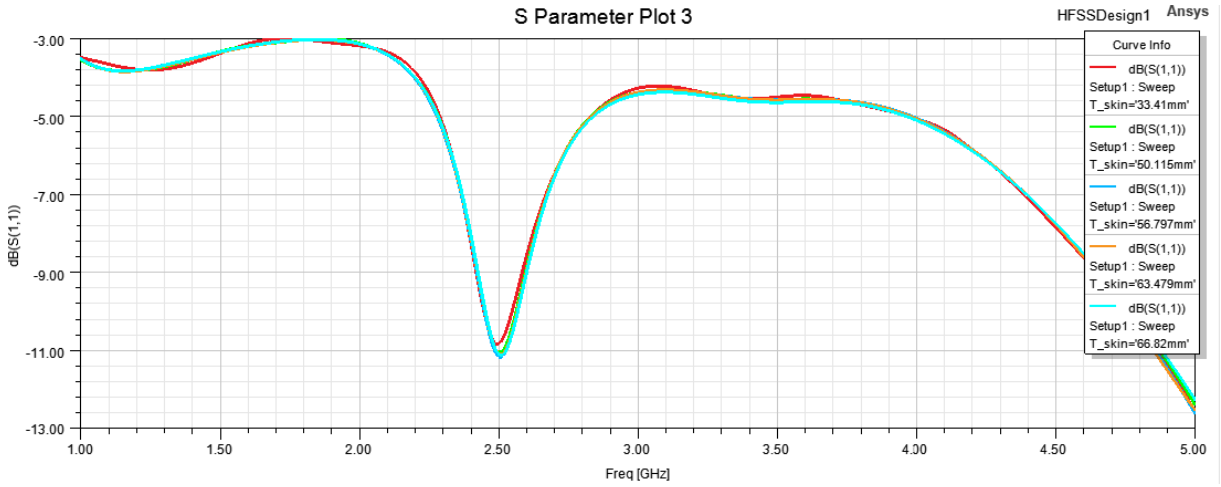
Figure C.4: Patch antenna design.

bandwidth and resonance, under the loading effect of the body. Skin and muscle properties at the frequency of operation were used during the simulaton [118]. The physical structure was simplified to a skin volume as described in Chapter 3 to shorten the simulation time. Results are shown in Figure C.5, note the stability of the behaviour for both simplified structures, at varying thicknesses. It can be seen that a 6–dB bandwidth of 400 MHz is achieved, which is sufficient for this application at close distances. This thickness sweep also indicates that a thickness of 0.5λ is sufficient to approximate the antenna behaviour, as such, it is acceptable to move forward with without the need for a thickness sweep for future simulations.

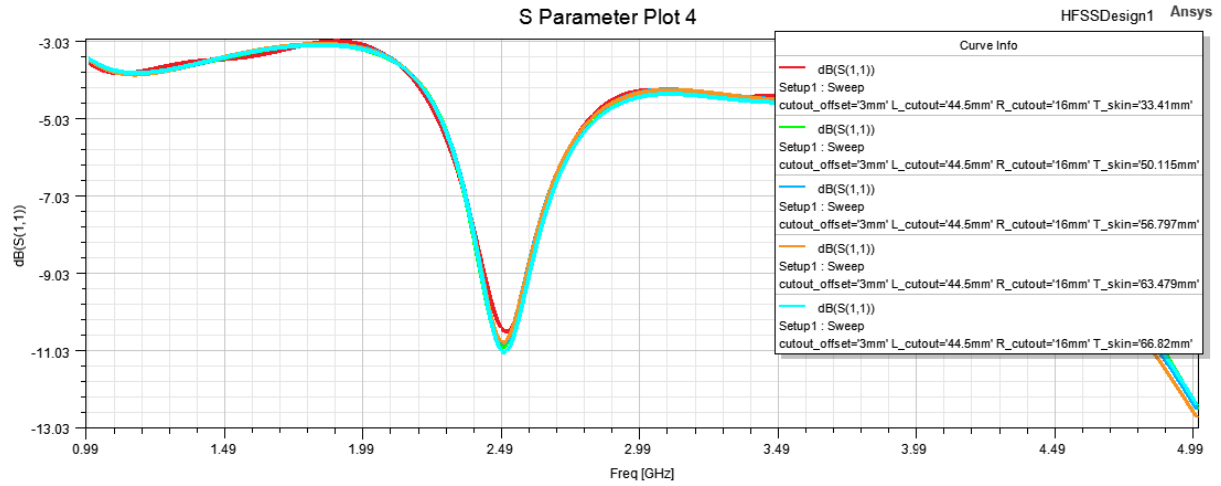
To characterize coupling between receiver and transmitter antennas, a simulation was conducted again with two antennas with a separation distance sweep between 0.5λ–1.5λ for both skin and muscle layers. Results for S_{11} and S_{21} are shown below in Figure C.6 and Figure C.7, respectively. It can be seen that the 6–dB bandwidth, is acceptable, with the antenna displaying good coupling performance.

LNA: SKY67183

This LNA has a wide band (400–6000 MHz) with high gain flatness, very high linearity, and a small package size. The LNA requires input and output matching networks as well as DC-blocking capacitors. The LC component values for operation in the 2300–2700 MHz frequency range we used as a preliminary starting point, as specified in the datasheet, but will be tuned upon fabrication. The LNA requires a supply voltage of 5.0 V, which is provided by the Raspberry Pi.

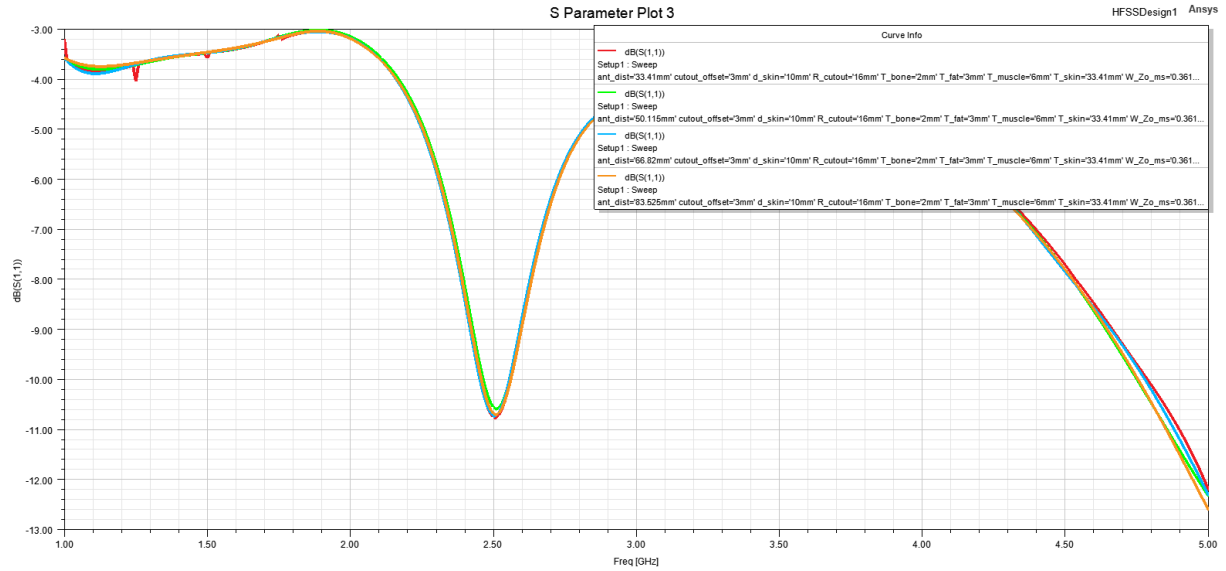


(a) Simulation using muscle layer

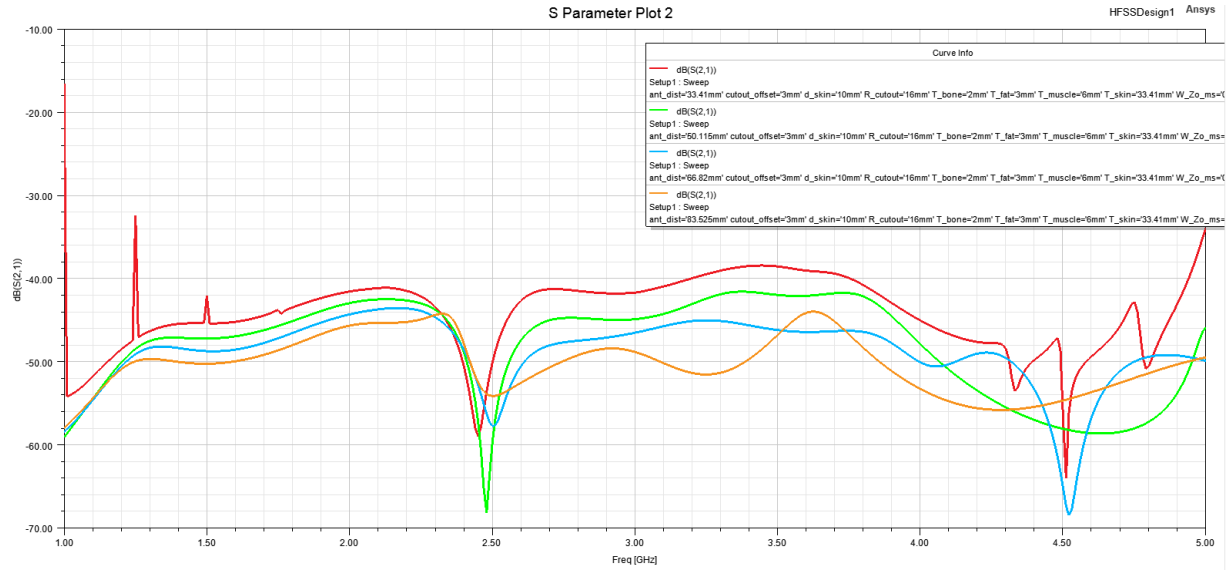


(b) Simulation using skin layer

Figure C.5: Simulation of a single antenna with varying tissue layer thickness

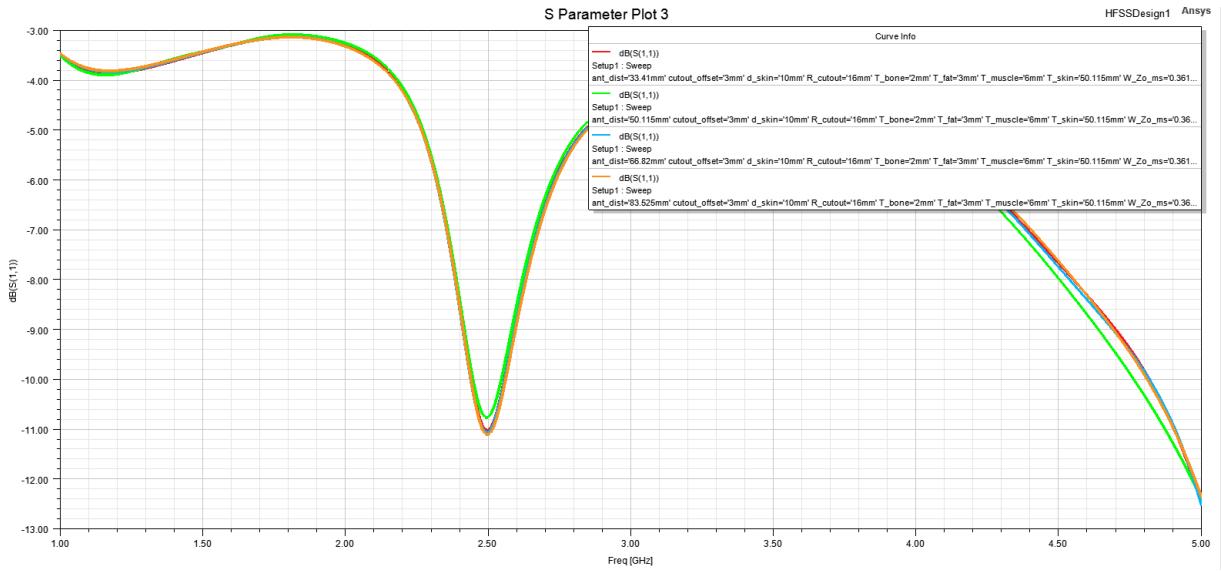


(a) S11 sweep

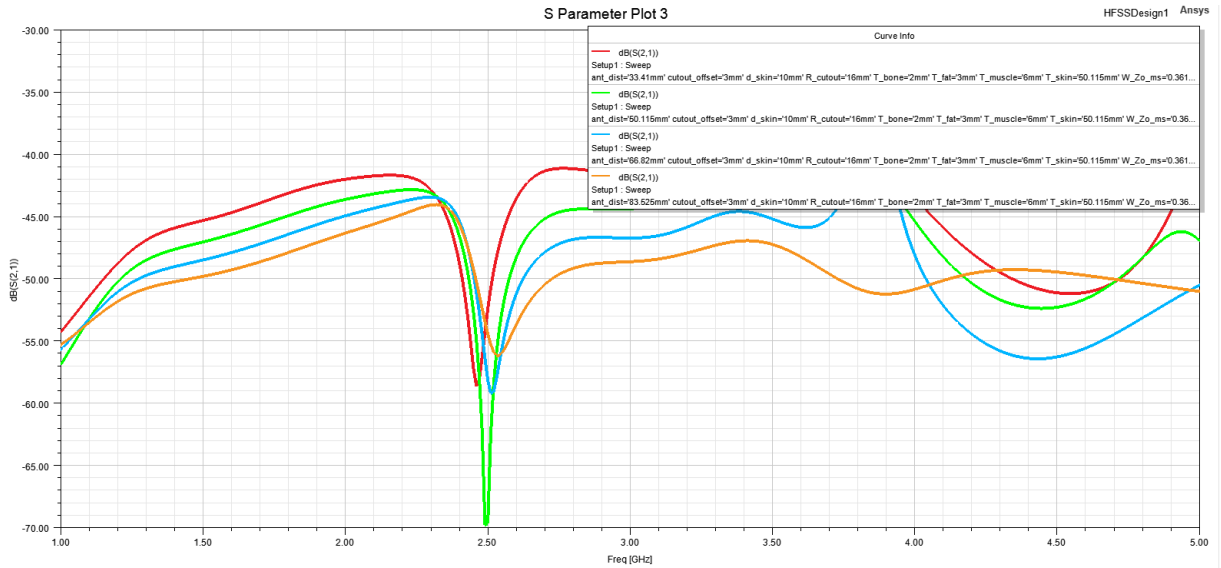


(b) S21 sweep

Figure C.6: Simulation of two antennas on top of skin with varying separation distance



(a) S11 sweep



(b) S21 sweep

Figure C.7: Simulation of two antennas on top of muscle with varying separation distance

Mixer: MAX2681

The low-noise down-converter mixer used has a small package size. The mixer operates with RF input frequencies between 400 MHz and 2500 MHz, and down-converts to IF frequencies between 10MHz and 500MHz. As mentioned in the 25-dB coupler section, the LO power level must be between −10.0 and 0 dBm, which it receives through the 25–dB coupler. The IC utilizes a supply voltage between 2.7–5.5 V, allowing it to be powered directly from the Raspberry Pi. This mixer offers a low sleep supply current of less than 0.1 μA, which is helpful for power management. Matching at the output was initially designed for the IF frequency of 70 MHz. However, this is just a placeholder that was specified in the datasheet, with further fine-tuning required during bring-up.

IF amplifier: MAX4430

This stage of the receiver chain amplifies the IF signal into the range of the SPI-compatible ADC. The schematic and layout are according to the sample design in the MAX4430 datasheet but will require some tuning. The curcuit uses rails of 5.0 V and 0 V (as provided by the Raspberry Pi).

LPF

The LPF comes right after the IF amplification stage. It is a fairly simple third-order filter constructed with discrete LC components. This is designed for a cutoff of 10 sMHz, but the value must be adjusted with some tuning as the device functionality is tested to remove undesired out-of-band effects.

ADC: MAX11105AUT

A successive approximation 12-bit ADC with a 3 MSPS sampling rate was selected. This is sufficient for this application as the vital signals to be detected are in the below 5 Hz and this sampling rate and resolution should be sufficient to capture this data. It enables automatic continuous monitoring of a given channel. This ADC requires peripheral filtering, anti-aliasing, and DC offset stages, as it does not have a negative and a positive reference. The device consumes a small amount of current and requires a supply voltage of 3.3 V which can be supplied by the Raspberry Pi.

Table C.2: Summary of RF front end design.

Component	**IC**	Supply Voltage (V)
Signal generator	AD9837	3.3
VCO	MAX2750	3.3
PA	SE2574BL-R	3.3
Coupler	X3C19P2-30S	N/A
Antenna	PCB Component	N/A
LPF	LC components	N/A
LNA	SKY67183	5.0
Mixer	MAX2681	3.3
IF Amp	MAX4430	5.0 / 0.0
ADC	MAX11105AUT	3.3